A Study of Nuclear Recoils in Liquid Argon Time Projection Chamber for the Direct Detection of WIMP Dark Matter

Huajie Cao

A Dissertation

Presented to the Faculty

of Princeton University

in Candidacy for the Degree

of Doctor of Philosophy

Recommended for Acceptance

by the Department of

Physics

Adviser: Cristiano Galbiati

November 2014

UMI Number: 3665305

UMI
Dissertation Publishing

ProQuest®

Abstract

Robust results of WIMP direct detection experiments depend on firm understandings of nuclear recoils in the detector media. This thesis documents the most comprehensive study to date on nuclear recoils in liquid argon - a strong candidate for the next generation multi-ton scale WIMP detectors. This study investigates both the energy partition from nuclear recoil energy to secondary modes (scintillation and ionization) and the pulse shape characteristics of scintillation from nuclear recoils.

Our collaboration, SCENE, acquired the scintillation and ionization signals of recoiling nuclei in liquid argon as a function of applied electric field by exposing a dual-phase Liquid Argon Time Projection Chamber (LAr-TPC) to a low energy pulsed narrowband neutron beam produced at the Notre Dame Institute for Structure and Nuclear Astrophysics. I present measurements of the scintillation yield and the scintillation pulse shape for nuclear recoils with energies from 10.3 to $57.2\,\mathrm{keV}$ and for applied electric fields from 0 to $1000\,\mathrm{V/cm}$. For the ionization yield, I report measurements from 16.9 to $57.2\,\mathrm{keV}$ and for electric fields from 50 to $500\,\mathrm{V/cm}$. I also report the observation of an anti-correlation between scintillation and ionization from nuclear recoils, which is similar to the anti-correlation between scintillation and ionization from electron recoils. With an assumption that the energy partition in excitons and ion pairs of $^{83m}\mathrm{Kr}$ internal conversion electrons is comparable to that of $^{207}\mathrm{Bi}$ conversion electrons, the numbers of excitons (N_{ex}) and ion pairs (N_{i}) and their ratio ($N_{\mathrm{ex}}/N_{\mathrm{i}}$) produced by nuclear recoils from 16.9 to $57.2\,\mathrm{keV}$ are calculated. Motivated by arguments suggesting direction sensitivity in LAr-TPC signals due to columnar recombination, a comparison of the light and charge yield of recoils parallel and perpendicular to the applied electric field is presented for the first time.

Acknowledgements

I express my deepest thanks to my adviser Prof. Cristiano Galbiati for providing critical support to the SCENE experiment whenever it was most needed, and for giving me the opportunity to work on such a challenging experiment. This experience has greatly enhanced both my scientific knowledge and my ability to independently complete long-term projects. I thank my co-adviser Prof. Peter Meyers for his detailed feedback on this work.

Equally important were the support and guidance I received from Dr. Stephen Pordes, Dr. Henning Back, Dr. Jonghee Yoo, Dr. W. Hugh Lippincott, and Dr. Fritz DeJongh at Fermilab. They provided the material and human resources necessary for the construction and testing of the LAr-TPC, which is central to the experiment. They also supervised and participated directly in its design, prototyping and completion of the TPC at the Proton Assembly Building (PAB) of Fermilab. Our productive interactions at PAB were the highlights of my many month visits of the lab. I hope I have made a lasting impression on them too, beyond my ambulance incident on a Saturday.

I would like to thank Prof. C. Jeff Martoff of Temple University, who not only made big contributions to the SCENE experiment since its beginning, but also devoted many days of his own time to each beam run at the University of Notre Dame. Furthermore, the success of the beam runs would not have been possible without the considerable efforts from his students John Tatarowicz, Susan Walker, Andrew W. Watson and Daniel Olvitt in deploying the apparatus at Notre Dame and sharing the data-taking shifts.

Dr. Hanguo Wang of University of California, Los Angeles (UCLA), in addition to generously providing important pieces of apparatus used in the experiment, gave me and our collaboration crucial comments and suggestions in improving the design of the experiment and the apparatus. I am grateful for having such an expert always within reach.

Next, I would like to acknowledge the rest of the people whose efforts directly contributed to the SCENE experiment in chronological order. The first proposal of the experiment was drafted together by Dr. Pablo Mosteiro and me. We received generous and insightful feedback

Avetisyan, Stephanie Lyons, Kevin Siegl, Sabrina Strauss, along with the students from Temple University previously mentioned, without whom the apparatus would never have been set up for the beam runs and the data-taking shifts would not have been filled.

Besides contributions to data-taking, Thomas Alexander (now at the University of Massachusetts, Amherst) helped me implemented the LabView slow control and worked on data analysis related to Cerenkov radiation. Yixiong Meng also performed the GEANT4 Monte Carlo simulation studies of the TPC and cross-checked my analysis results. I would like to thank Dr. Stephen Pordes, Prof. C. Jeff Martoff, Dr. Giuliana Fiorillo, Prof. Wanpeng Tan, Dr. W. Hugh Lippincott, and Dr. Samuele Sangiorgio for their helpful comments on the analysis results.

I thank W. McClain of chemistry department for preparation of the phenylphosphonic acid subtrate for TPB coating on ITO electrodes. I thank Dr. G. Korga and Dr. A. Razeto for providing the low-noise amplifiers used on the TPC PMT signals. I thank Prof. D. N. McKinsey, Dr. S. Cahn, and K. Charbonneau of Yale University for the preparation of the ^{83m}Kr source. I thank E. Vázquez-Jáuregui of SNOLAB for assistance with MC simulations.

Finally, I also want to thank my fellow scholars of the Princeton DarkSide group: Dr. Masayuki Wada, Jason Brodsky, Emily K. Shields, Shawn Westerdale, Guangyong Koh, Hao Qian, Chris Stanford, Xin Xiang, and Chengliang Zhu for our stimulating discussions. I must not forget to thank the group secretaries Helen Ju (Princeton), Cindy Kennedy and Cathryn Laue (both Fermilab) for their assistance with the experiment's purchases and my travel arrangements.

The work described in this dissertation has been published in the following articles and presented at the following conferences:

arXiv:1406.4825 (submitted to Physical Review D)

Physical Review D 88, 092006 (2013)

UCLA's 11th Symposium on Sources and Detection of Dark Matter and Dark Energy in the Universe, February 2014, Los Angeles, California

13th International Conference on Topics in Astroparticle and Underground Physics, September 2013, Asilomar, California

American Physical Society Meeting, April 2013, Denver, Colorado

To my family.

Contents

List of Tables

List of Figures

Preface

This preface is a short recount of the SCENE experiment - the experiment presented in this work - from my perspective. Its very beginning was in January 2011 at a group discussion initiated by my adviser, Prof. Galbiati on using a low energy pulsed narrowband neutron beam to study nuclear recoils (the merit of the idea will be evident when the results are shown in Ch 8). After that discussion, Dr. Pablo J. Mosteiro, another PhD student then, and I were assigned the project of studying the feasibility of this experiment scheme and defining the constraints to the design of its setup. I feel proud in stating that since the moment when the experiment started from the drawing board I have played a major role in it. I must consider myself very fortunate that, in the age of big science, I could follow the details of an experiment and make direct impact on it from start to finish during my graduate school career.

Our study later turned into a full-fledged experiment proposal [1]. Thanks to the admirable coordination skills of my adviser, interested physicists from Fermilab, Temple Univerisity, Istituto Nazionale di Fisica Nucleare (INFN) - Napoli, the University of California, Los Angeles (UCLA), and the University of Notre Dame joined the effort to turn this idea into reality. The SCENE Collaboration was thus born in the fall of 2011. The acronym SCENE stands for scintillation efficiency of noble elements. The ambition of the group includes studies on liquid xenon besides liquid argon. The collaboration expanded later as more physicists from the University of Massachusetts - Amherst, University College Lon-

don, the University of Chicago, and Lawrence Livermore National Laboratory (LLNL) made contributions to the effort.

Starting a project from scratch is not an easy job. I still remember how unpredictable and technically challenging our proposed experiment appeared to me, when I stepped in the accelerator lab of the University of Notre Dame for the first time. At that moment, I had no experience and very little knowledge of test beam experiments. The unwavering assurance and support of my adviser, my supervisors at Fermilab and other collaborators, made sure that my fear of uncertainty did not ever hold me back. That allowed my curiosity to lead me in the right directions. I was absorbed in looking up new information for solutions to our problems. The joy of accomplishment kept streaming in while we built and refined the setup of the experiment, motivating me further.

Not until much later did I realize that this experiment marked the beginning of a new phase in my scientific pursuits. This phase involved not just quests for ultimate accuracy and precision in making measurements, but one that required judgments and decisions in testing the unknown. Natural to any creative enterprise, many progresses made by our collaborators and I required tough choices between risk (of failed design and delayed experiment, in our case) and reward (improvement on the results). Each decision made during the design phase has a serious impact at the implementation stage. After that, the care and effort put into implementation would lay the foundation for reliable running of the eventual experiment. Such care and effort required prioritizing under time constraints. My survival of this phase has taught me precious lessons on compromise between perfection and practicality. In this sense, doing experimental science trained my ability to managing project risk. This in my opinion is the most valuable part of my graduate school experience.

From December 2011 to November 2013, I visited the accelerator facility of Notre Dame for seven times. Besides the first - a group trip to survey the facility - and the fourth trip for accelerator operator training, every visit marked a beam test campaign. The last four of them were one-week to two-week long (not including the setup period) around-the-clock

data-taking efforts. At the accelerator facility, the schedule of experiments was determined weeks even months in advance, thus the beam time allotted to our experiment left little margin for errors in our preparation, deployment and operations. Teamwork played a huge role in our wins against such challenges. I learned to put faith in the team. I witnessed the impressive efficiency a group of individuals working in solidarity could achieve, despite the shortage of manpower, experience and the long list of tasks. I remembered the numerous instances where the members of the technical staff at Proton Assembly Building of Fermilab went beyond their normal workload to assist the development and testing of our liquid argon detector to meet our schedule. I also remembered the dedication of the graduate students, post-doctorate researchers, faculty members and technical staff on shift at the beam test, and the hard work they put in to help the experiment recover from equipment breakdowns.

I hope this little narrative attempt could remind readers that behind the data, figures, and equations of science treatises and reports often hide the real human stories of scientific discovery and advancement.

Chapter 1

Introduction

"There is more than meets the the eyes" - this adage applies literally to our universe. Recent research [2] concludes with an astounding precision that 85% of the matter in the universe is in a form that neither emits nor absorbs electromagnetic radiation, yet the identity of this "dark matter" remains a mystery. The determination of its identity is one of the biggest scientific challenges of our time.

The collection of evidence of its existence has been growing since 1930s. Classic evidence such as velocity dispersion of galaxies in galaxy clusters and rotation curves of individual galaxies, has gained further support from the breakthrough findings in large-scale structures, cosmic microwave background, strong and weak gravitational lensing, and Big Bang nucleosynthesis over the last two decades (Ref. [3, 4] and References cited therein). It is a crucial fact that the whole collection is based on its gravitational effects on known forms of matter and radiation. These observations thus also highlight to us its lack of electromagnetic and strong nuclear interactions with known matter or with dark matter itself. This fact separates dark matter from baryons and charged leptons.

In addition to interacting gravitationally and possibly also via other ultra-weak processes, large-scale structure of the universe poses another requirement that dark matter should be "cold", *i.e.*, non-relativistic at the onset of galaxy formation [5]. Although Standard

Model neutrinos fit the first requirement, they would smooth out fluctuations below a scale of $\sim 40\,\mathrm{Mpc}$ (similar arguments apply to other "hot" and "warm", *i.e.*, fast moving dark matter candidates). Cosmological simulations based on Lambda Cold Dark Matter (ΛCDM) model resembled observations remarkably closely across the entire simulated scales [6]. For the ΛCDM model to give predictions that match observations from different epochs of the universe, one must also assume that dark matter is stable on cosmological time scales and it has the right relic density from the Big Bang. Those properties further suggest dark matter to be particles beyond the Standard Model. Hence, the understanding of dark matter particle will bring along with it the understanding of new physics. In other words, cracking this puzzle of dark matter's identity will have far-reaching implications on both astrophysics and particle physics.

Despite the multitude of existing observations that provide constrains on the properties of non-baryonic dark matter, ingenious theoretical particle physicists found no shortage of possible candidates that could constitute dark matter. Many of them not only would fit the constraints deduced from astronomical observations, but would also solve long standing problems in the Standard Model of particle physics. Some of the most prominent candidates include weakly interacting mass particles (WIMPs), axions and sterile neutrinos. WIMPs might solve the gauge hierarchy problem by revealing new physics at the weak interaction scale; axions are motivated by a solution to the strong CP problem; sterile neutrino could explain the observed neutrino masses. The motivations for those particles and related particle physics problems are interesting and important topics in modern day physics. Because they are established subjects in the dark matter research field and do not contribute directly to the discussions or affect the conclusions of this thesis, I will not elaborate on them in this thesis. Excellent reviews [3, 5, 7, 8] and PhD dissertations in my field [9–12] covered several times the evidence, the understood properties, and the list of most well-motivated candidates of dark matter. I refer the interested readers to those good resources and the references cited therein for a complete review of the foundational topics.

Since the beginning of my graduate school career, I have been making contributions to the DarkSide program, an experimental research that aims at testing the hypothesis of WIMPs as a dark matter candidate. The progress of the experiment is supported by 32 institutions from 7 countries. The goal of this program will be achieved by observing collisions between WIMPs and ordinary nuclei, or by demonstrating the absence of such collisions. DarkSide champions liquid argon as its chosen target nuclei and the liquid argon time projection chamber (LAr-TPC) technology for its WIMP detectors. My study on the recoiling nuclei of argon in LAr-TPC is primarily motivated by its application in the DarkSide program.

My thesis is arranged in the following structure. In Chapter 2 and 3, I review the expected properties of WIMPs and the current experimental efforts in its detection. In Chapter 4, I describe the DarkSide program and explain the importance of my thesis experiment to this program and to other related research efforts. In Chapter 5, I compare the techiques and results of related experiments. In Chapter 6, I describe the experiment scheme and apparatus. In Chapter 7 and 8, I present the details of the analysis, including calibration, event selection, and results.

Chapter 2

WIMP Dark Matter

Weakly interacting massive particles (WIMPs) represent a general class of dark matter candidates that may be the thermal relics of the Big Bang. In this chapter, I cover the general properties of WIMPs and various methods for their detections.

2.1   Properties of WIMPs

In standard cosmology, *i.e.*, in the framework of the ΛCDM model, WIMPs are in thermal and chemical equilibrium with the hot "soup" of Standard Model particles after inflation. Two factors control the abundance of WIMP after that: one is the cooling of the universe and the other is its expansion. When the universe cools to temperatures below the WIMP mass, m_X, the co-moving density, *i.e.*, the density ignoring the expansion of space, of WIMPs decreases exponentially with its temperature according to the Boltzmann factor $e^{-m_X/T}$ as a result of WIMP self-annihilation. As the universe expands, the corresponding drop in the WIMP density suppresses the rate of self-annihilation. When the self-annihilation rate becomes smaller than the Hubble expansion rate, WIMPs freeze out, or chemically decouple from the thermal equilibrium. Although the WIMP density continues to decrease with the expansion of the universe, its co-moving density approached a constant. If we assume this constant co-moving density is equal to the observed value for dark matter, the WIMP self-
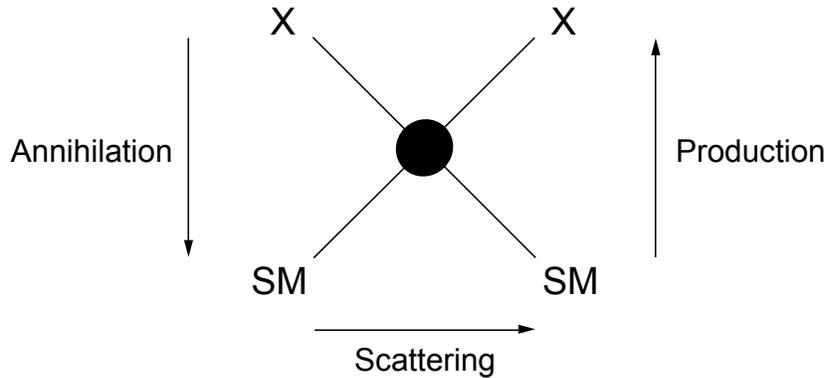
Figure 2.1: Possible non-gravitational interactions of WIMP (X) with Standard Model particle (SM).

annihilation cross-section needed to account for it is at the weak scale. A sketch of the calculation is given in [11].

The WIMP mass cannot be directly derived from the relic density, but on dimensional grounds [3], the weak coupling assumption leads to plausible WIMP masses in the range of $\sim 30\,\text{GeV}$ - $1\,\text{TeV}$, which coincides with the weak scale. The coincidence that weak scale particles interacting through the weak force form the right relic density is sometimes referred to as the "WIMP miracle". This is the motivation of considering WIMPs as excellent dark matter candidates.

New stable particles at the weak scale are predicted by some theoretical extensions to the Standard Model of particle physics, such as the models of supersymmetry or extra spatial dimensions. Those theoretical frameworks were invented to address the gauge hierarchy problem for which new physics and new particles are required at the weak scale. The discovery of WIMP could become powerful validation for some of those frameworks as the successor to the Standard Model. This is a major reason for WIMPs being perhaps the most widely studied class of dark matter candidates to date.

One more reason for WIMPs' prominence is the number of possibilities to test their existence with current and near future experiments. Since WIMPs must annihilate to other particles to yield the observed relic density, in conventional particle physics framework they

can produce three types of observable signatures under the right circumstances. As shown in Fig. 2.1, the processes WIMP can take part in include: (X stands for WIMP and SM stands for a Standard Model particle)

- **Annilation**: X + X → SM + SM. In regions of space where the WIMP density is sufficiently large, the radiation produced by their pair-annihilation may be detectable on or near the Earth.

- **Production**: SM + SM → X + X + {SM}, where {SM} denotes one or more SM. WIMPs may be produced at particle colliders. Since WIMP by its definition interacts only weakly and gravitationally and has cosmological scale lifetime, they will pass through detectors without a trace, but their existence can be inferred by the missing momentum of the collision products, similar to the neutrino/antineutrino produced in beta decay. For the same reason, although WIMPs may be produced through SM + SM → X + X, such events are undetectable.

- **Scattering**: X + SM → X + SM. If WIMPs can scatter off Standard Model particles through weak interaction, the deposited energy and momentum may be signatures of their existence.

These three types of signatures of WIMP are accessible with current technology and they are keenly sought after in a large number of current and proposed experiments.

2.2   Methods of detection

The field of dark matter research has coined the terms "indirect detection", "particle colliders" and "direct detection" to classify the type of experiments targeting each of the three signatures of WIMPs. Over the past thirty years, each category of WIMP searches has grown into a mature field of study consisting of a considerable number of experiments [13, 14]. Here I provide an overview for each class:

- **Indirect detection**: These experiments seek the WIMP pair-annihilation products in the forms of photons (gamma rays, X-rays, and radio), neutrinos and cosmic rays (including positrons, electrons, antiprotons, and antideuterons). The instruments detecting those signals presently include space- and ground-based gamma-ray telescopes and cosmic-ray detectors, large underground, under-ice, and underwater neutrino telescopes. Apart from neutrinos, the indirect detections probe the characteristic annihilation cross section of WIMP thermal relics. Search for neutrinos, on the other hand, constrains the scattering cross sections. If WIMPs scatter on nuclei and slow down when passing through the Sun or the Earth, there may exist a substantial density of captured WIMPs in the center of the Sun and the Earth. Neutrinos from WIMP annihilation at those locations can escape and be detected, but not the other types of products (see Section 3.4 of Ref. [3]).

- **Particle colliders**: The particle colliders provide a controlled laboratory environment to study the production of WIMPs from the Standard Model particles. Proton-proton collisions at the Large Hadron Collider (LHC) probes a broad range of WIMP masses for the case of substantial couplings between WIMPs and nuclear matter; the decommissioned Large Electron-Positron Collider (LEP) excluded dark matter with electroweak-size couplings to electrons with a mass below about $90\,\text{GeV}$. The search results at particle colliders can constrain many WIMP properties and WIMP theories. However, colliders are unable to distinguish missing momentum signals produced by a particle with lifetime $\sim 100\,\text{ns}$ from one with lifetime $\gtrsim 10^{17}\,\text{s}$ required for dark matter.

- **Direct detection**: These experiments target the signals produced by WIMPs scattering off nuclei in detectors. This method provides the most straightforward and potentially the least ambiguous signals for WIMPs. The Earth along with the solar system is believed to be traveling though the dark matter halo of the Milky Way Galaxy while orbiting the galactic center. The gravitational binding energy of our galaxy determines the velocity distribution of WIMPs, which in turn defines the energy scale

of WIMP scatterings. With a weak scale WIMP mass, the kinetic energy transferred to nuclei through elastic scattering is $\lesssim 100\,\text{keV}$ [13]. Detecting those $\lesssim 100\,\text{keV}$ nuclear recoils requires sensitive detectors and good discrimination against background. Electron scatterings unfortunately have too low energy to be detected by current technology.

The rate and energy spectrum of those events depend on the details of the WIMP-nucleus scattering cross sections and the velocity distribution and local density of WIMPs. Since the local density of the halo at the vicinity of the Earth is known to within a factor of two, the weak scale cross section limits the event rate to an order of a few events per kg or per ton per year (see Section 2 of Ref. [13]). This makes WIMP direct detection similar in nature to other rare event experiments, such as solar neutrino observatories and search for neutrinoless double-beta decay. The stringent requirements on background suppression force these detectors to be hosted in deep underground laboratories, where the flux of neutrons produced by cosmic ray showers is at a minimum.

Despite decades of R&D efforts and orders of magnitude improvement on the search sensitivities of these experiments, a positive signal for WIMPs is yet to be established through any of the methods. However, many researchers are optimistic that at the current rate of progress, the discovery may take place by the end of this decade [4, 8]. In the 2013 US high-energy physics community study, the leading researchers in the dark matter field reaffirmed these detection methods as three of the "four pillars" of the dark matter search program [4]. The fourth pillar "astrophysical probes" is unsurprisingly the extension of the astronomical observations that initially provided the evidence of dark matter and many of its known properties. Those probes will focus on searching for the impacts of non-gravitational interactions of dark matter on astrophysical phenomena. The experts reiterated the importance of each of the "four pillars" and their complementarity to one another [4].

In this chapter I have covered the basic properties of WIMPs and the detection methods. My goal is to show the readers how DarkSide, a program of direct dark matter searches that inspired the SCENE experiment, fits in the broad scientific program of dark matter research.

Chapter 3

Direct detection of WIMPs

The direct detection experiments test the hypothesis that WIMP-nucleus interactions can produce nuclear recoil signals in detectors. These signals include a recoil energy spectrum, its annual modulation, and a sidereal daily cycle of the recoil directions. In this chapter, I first summarize the characteristics of these expected signals and then survey the leading direct detection technologies. Finally, I summarize the current status of WIMP direct detection. The most up-to-date reviews written by the leading researchers in this field can be found in [13, 15].

3.1   Signals of direct detection

3.1.1   Nuclear recoil energy spectrum

In a WIMP detector, the differential rate for WIMP elastic scattering off nuclei can be expressed as:

$$\frac{dR}{dE_R} = N_N \frac{\rho_0}{m_W} \int_{v_{\min}}^{v_{\max}} d\boldsymbol{v} \, f(\boldsymbol{v}) \, v \, \frac{d\sigma}{dE_R} \,, \tag{3.1}$$

where N_N is the number of the target nuclei, m_W is the WIMP mass, ρ_0 the local WIMP density in the galactic halo, $\boldsymbol{v}$ and $f(\boldsymbol{v})$ are the WIMP velocity and velocity distribution

13

function in the Earth frame and $d\sigma/dE_R$ is the WIMP-nucleus differential cross section. Given the measured local dark matter density, ρ_0 and a model of the WIMP velocity distribution, $f(\boldsymbol{v})$, the measured nuclear recoil energy spectrum determines the WIMP-nucleus cross sections for a certain WIMP mass, m_W.

WIMPs with speeds larger than $v_{esc}(r) = \sqrt{2|\phi(r)|}$, where $|\phi(r)|$ is the gravitational potential, are not gravitationally bound to the galaxy. The v_{esc} constraint, $i.e.$, the "cold" nature of WIMPs keep the kinematic calculations in the non-relativistic limit. Therefore, the energy transferred to the recoiling nucleus is:

$$E_R = \frac{p^2}{2m_N} = \frac{\mu^2 v^2}{m_N}(1 - \cos\theta), \tag{3.2}$$

where p is the momentum transfer, θ is the scattering angle in the WIMP-nucleus center-of-mass frame, m_N is the nuclear mass and μ is the WIMP-nucleus reduced mass:

$$\mu = \frac{m_N \cdot m_W}{m_N + m_W}. \tag{3.3}$$

Therefore, the minimum velocity is

$$v_{\min} = \sqrt{\frac{m_N E_R}{2\mu^2}}, \tag{3.4}$$

and $v_{\max}$ is the galactic escape velocity in the Earth reference frame.

With standard assumptions about the WIMP halo and WIMP-nucleus interaction, the energy spectrum of nuclear recoils from WIMP scattering is a featureless, rising exponential as the energy decreases. The general shape of the energy spectrum does not depend on the underlying particle physics, as low-energy scatterings will be close to isotropic in the center of mass frame. However, the interaction cross section is highly dependent on particle physics models and it can vary by orders of magnitude. In the non-relativistic limit, the WIMP-nucleon couplings are commonly divided into the "spin-dependent" terms, when the

sign of the scattering amplitude depends on the relative orientation of particle spins, and the "spin-independent" terms when spin orientations do not affect the amplitude (see details in [15] and References cited therein). For spin-dependent interactions, the WIMP effectively couples to the net nuclear spin, due to cancellation between opposite spin pairs. For spin-independent couplings, the total nuclear cross section depends on the number of protons and neutrons and the relative strength of proton and neutron couplings to WIMPs. Recoil energy spectra of multiple target nuclei may constrain the spin-dependent and -independent WIMP-nucleon couplings.

On the astrophysics front, the recoil spectrum was shown to be largely independent of many features of the galactic halo distribution [16], so astrophysical uncertainties are expected to play only a small role. It however also implies that, after the WIMP discovery phase, energy spectra from direct detection experiments will provide little information to aid the studies of the galactic halo models.

Experimentally distinguishing the nuclear recoils due to scattering of WIMPs from various radioactive background signals is a major challenge for direct detection experiments (see more detail in Sec. 3.2). A significant number of events and agreement from multiple detectors at different geographical locations might therefore be needed before a definitive discovery can be declared.

3.1.2 Annual modulation of the energy spectrum

It was recognized quite early that the nuclear recoil energy spectrum is not static over time. Even assuming an absence of large unknown fluctuations in local WIMP density due to small scale structures of the dark matter halo, the Earths motion around the Sun can produce an annual/seasonal modulation of the energy spectrum [17].

When the Earth's orbital vector is aligned with the Suns orbital vector - as happens in summer - the Earth's speed with respect to the Galactic rest frame is largest. This boosts the WIMP speed distribution in the Earth's frame towards higher speeds and hence leads to

15
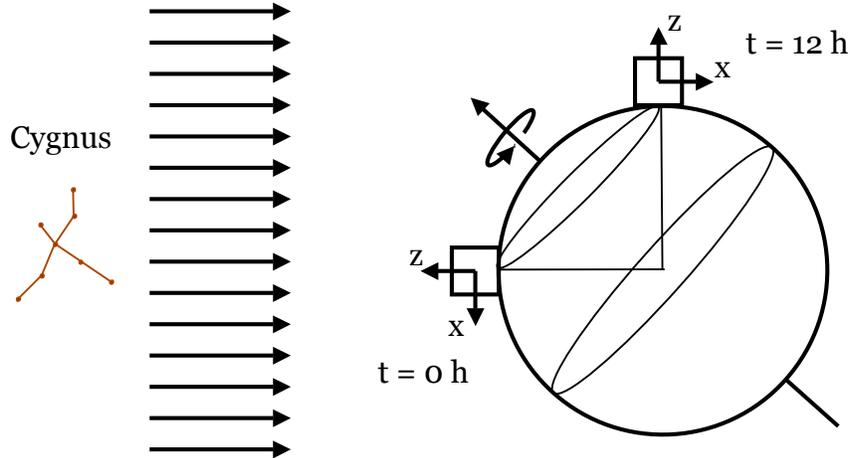
Figure 3.1: (Fig. 2 in Ref. [18]) The daily rotation of the Earth introduces a modulation in recoil angle, as measured in the laboratory frame.

a larger number of high energy recoils and a deficit of low energy recoils. Unfortunately, the amplitude of the annual modulation is on the order of a few percent, because the Earth's orbital speed is small compared to the Sun's speed with respect to the Galactic rest frame.

As mentioned earlier, distinguishing WIMPs scattering off of nuclei from background is a major challenge, and it also applies to the spectrum's annual modulation. The long standing controversies surrounding the WIMP discovery claim of the DAMA/LIBRA experiment have demonstrated that the backgrounds themselves are likely to have seasonal modulation, via cycles in the cosmogenic production of radioactive elements. Nevertheless, annual modulation is an important feature of the WIMP signal.

3.1.3   Sidereal daily cycle of recoil directions

The main velocity component of an earthbound laboratory with respect to the galactic center of mass is due to the revolution of the solar system about the galactic center. This rotational velocity is nearly equal to the virial velocity of an isothermal dark matter WIMP halo [19]. In this situation, the kinematics of WIMP-nucleus scattering will result in recoil nuclei from WIMP scattering which are predominantly directed into the hemisphere antiparallel to the rotational velocity. However, the rotational velocity has a fixed direction in celestial

coordinates of right ascension and declination, which points towards the constellation Cygnus (see Fig. 8.14). In the laboratory frame, the Earth's rotation makes this direction rotate around the polar axis with a period of one sidereal day. The strength of the correlation varies for different WIMP halo models and different detector characteristics and has been extensively studied theoretically [20].

These studies show that in practically any WIMP model, even modest direction sensitivity for a limited number of detected events gives a powerful discriminant for identifying a signal with the galactic halo, as opposed to any isotropic or fixed-location source in the laboratory. Direction-sensitivity is therefore a highly desirable characteristic for a direct detection experiment, and has been actively sought after in many signal modalities for many years (see Ref. [18] and references cited therein).

3.2   Direct detection technologies

The last two decades witnessed an explosion of interest in dark matter searches, most notably in the direct detection experiments of WIMPs in deep underground laboratories. The research has been centered around two main themes: larger detectors and lower background. Fig. 3.2 and Fig. 3.3 show the growth of the field in terms of the number of active researchers, and detection sensitivities in terms of spin-independent WIMP-nucleon cross section probed under the simplest assumptions.

Due to the extremely low cross sections expected of WIMP-nucleus interaction and consequently the small event rate, WIMP detectors must have high detection efficiency of low energy nuclear recoils and strong discrimination power against background events.

The leading detector technologies with such capabilities include noble liquid, cryogenic solid state, and superheated liquid detectors. Noble liquids, liquid argon and xenon, allow simultaneous detection of scintillation and ionization from an ionizing particle interaction. The 3D position of the interaction can be determined to good precision in a time projection
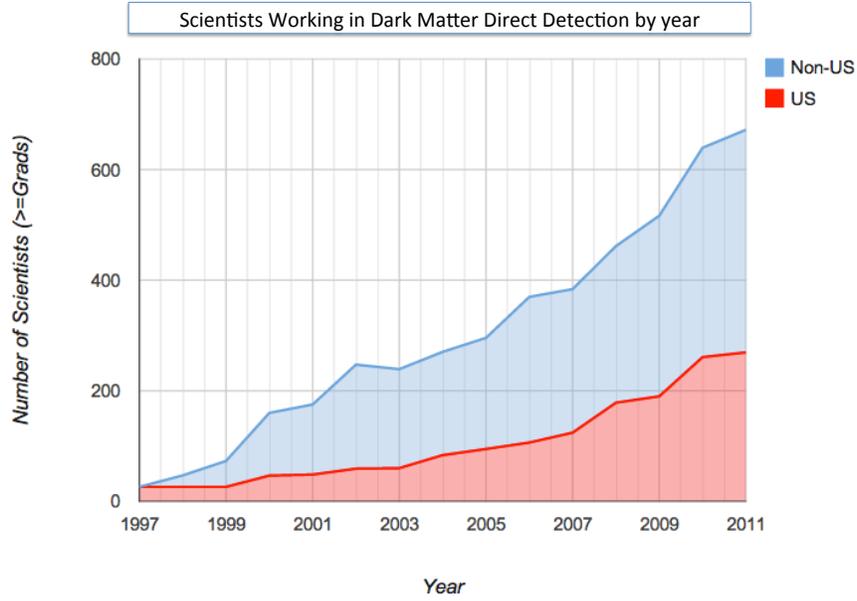
Figure 3.2: (Fig. 4 of Ref. [13]) Dark matter direct detection experiment demographics. The majority of the experiments search for WIMPs.
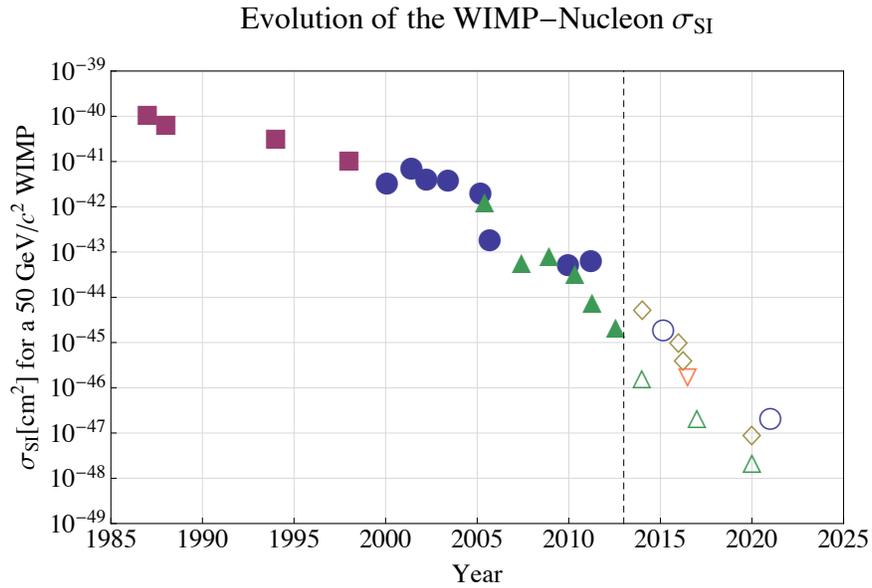
Figure 3.3: (Fig. 1 of Ref. [13]) History and projected evolution with time of spin-independent WIMP-nucleon cross section limits for a 50 GeV WIMP. The shapes correspond to technologies: blue circles - cryogenic solid state, purple squares - crystal detectors, brown diamonds - liquid argon, green triangles - liquid xenon, and orange inverted triangle - threshold detectors.

chamber. The ratio of energy dissipation in scintillation and ionization allows discrimination against electron recoil background (see background from β/γ radiation later in this sec-

tion). Scintillation pulse shape discrimination is an additional feature in liquid argon. The leading cryogenic solid-state bolometric detectors also use the ratio of energy measured in two different readout channels to provide the electron-recoil to nuclear-recoil discrimination. These two signal readout techniques are phonons (heat) and ionization for germanium and silicon, and phonons and scintillation light for calcium tungstate. The superheated liquid detectors are threshold devices, as a minimum energy deposition is required to induce a phase-transition, where an energy deposition destroys the metastable state, leading to the formation of bubbles. The bubble formation can be recorded both acoustically and optically. The operating temperatures and pressure can be adjusted to ensure only nuclear recoils (large stopping power) form bubbles, making them insensitive to electron recoils. The threshold detectors hold the best limits on spin-dependent WIMP-proton cross sections because of the use of target compounds containing ^{19}F - an unpaired proton makes its nuclear spin 1/2.

I mention scintillation crystal detectors for its historical importance. Since 1995, the DAMA/LIBRA experiment has been searching for the annual modulation of the WIMP scattering rate with 250 kg of sodium iodide crystals activated with thallium NaI(Tl). The experiment has observed an annual variation, with a phase consistent with expectation, in the single-scatter event rate at low energies with a statistical significance of more than 9σ. This observation is in strong tension with the results of many experiments using noble liquid, cryogenic solid state, and superheated liquid detectors, and another scintillation crystal detector using CsI (KIMS). Independent NaI(Tl) experiments are currently in progress to test the signal by ruling out the possibility due to seasonal varying background.

Detectors sensitive to the nuclear recoil directions, sometimes referred to as directional detectors, are the holy grail of WIMP direct detection. Most attempts at directional detection thus far have focused on low-pressure gas time projection chambers. Typically, $1\,\mathrm{m}^3$ of detector volume contains only $\sim$100 g target mass. The existing constraints on WIMP-nucleon cross sections require the future directional detectors to be several orders more

massive. More research into the anisotropy of nuclear recoil signals will therefore be needed to develop discovery-capable directional detectors.

Greater details for each of the detector types are covered in [13, 15] and references cited therein.

The sources of background generally fall within the following five categories:

- β/γ radiation

- surface α-particle radiation

- radiogenic neutrons: neutrons from radioactive decays

- cosmogenics: cosmic-ray muons and induced neutrons

- neutrinos (a concern only for future mega-scale detectors)

The β/γ radiations usually originate from the background sources intrinsic to the chosen detector target materials, radioactive impurities in the apparatus and shielding components, and environmental radioactivity including airborne radon and its daughters. Typical current and near future detectors can discriminate electron recoils induced by β/γ radiations from nuclear recoils to a sufficiently high level to prevent leakage due to the tail of the distribution in discrimination parameter space. However, more stringent requirements in background reduction through material screening must be met to achieve the target sensitivities for multi-ton scale detectors.

^{210}Pb, a product of the ^{222}Rn decay chain with a half-life of 22 years, can deposit on the surfaces of the detectors' sensitive volumes, and its ^{210}Po daughter can generate a steady rate of α decays throughout the detectors' lifetime. The α particles can easily be identified by their large energy deposition (a few MeV), but the recoil nuclei, with kinetic energies of $\sim 100\,\text{keV}$, may mimic WIMP-induced nuclear recoils. Excellent position reconstruction capabilities and fiducial volume cuts can greatly reduce the level of contamination from this source. Reduced radon exposure and surface treatment before detector assembly are other ways to effectively solve this problem.

Fast neutrons can produce nuclear recoil signals identical to WIMP-scattering (this fact is exploited later for our nuclear recoil studies). (α, n) and fission reactions produce so-called radiogenic neutrons, with energies below 10 MeV; cosmic ray muons, which can still penetrate deep underground laboratories, generate neutrons with energies up to dozens of GeV. Both radiogenic and cosmogenic neutrons pose serious concerns for WIMP detectors. Stringent material selection, increased laboratory depth and reduced radon exposure are necessary precautions. With improving position resolution in large detectors, multiple scattered neutrons are less likely be a background. Even single-scatter neutrons may be eventually efficiently rejected by active neutron vetoes enclosing the WIMP detectors.

Neutrinos are considered the ultimate background for direct detection experiments with no recoil direction sensitivity. High fluxes of low energy solar pp-neutrinos contribute to the electron recoil background through neutrino-electron scattering. Higher energy neutrinos, such as the ^{8}B solar neutrinos, the atmospheric neutrinos, and the diffuse supernovae neutrinos, can produce neutrino-induced nuclear recoils from coherent neutrino-nucleus scattering, indistinguishable from WIMP-induced signals. Direction sensitive detectors may overcome the neutrino limit as neutrino sources are unlikely to produce signals with the same period as the WIMP halo.

3.3   Latest developments

Fig. 3.4 presents the limits of spin-dependent WIMP-nucleon interaction cross section as a function of WIMP mass derived from the direct detection experiments up to 2013, under standard assumptions of the halo model and WIMP-nucleon interactions (details of the assumptions are explained in Ref. [11, 22, 23]). Fig. 3.5 shows the limits and allowed regions for spin-independent cross section. The most notable features of the spin-independent plot are the tension between the allowed regions of WIMP-nucleon interaction derived from DAMA, CoGeNT, CRESST, and CDMS-Si experiments and the upper limits set by the other ex-
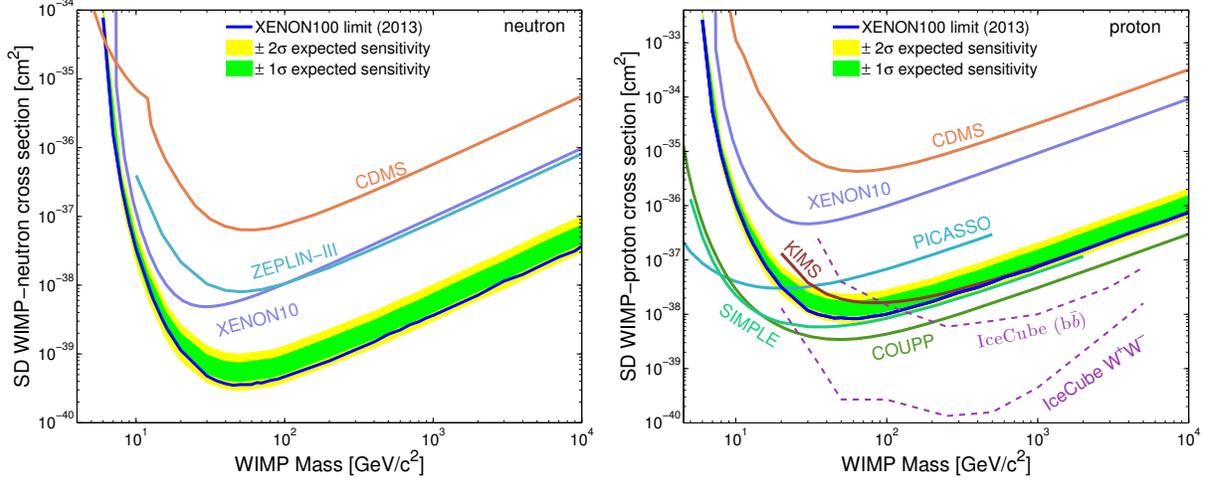
Figure 3.4: (Fig. 9 of Ref. [13]) Spin-dependent WIMP-neutron (left) and WIMP-proton (right) cross section limits versus WIMP mass for direct detection experiments, compared with the model-dependent Ice Cube results (model-dependent) as of summer 2013.
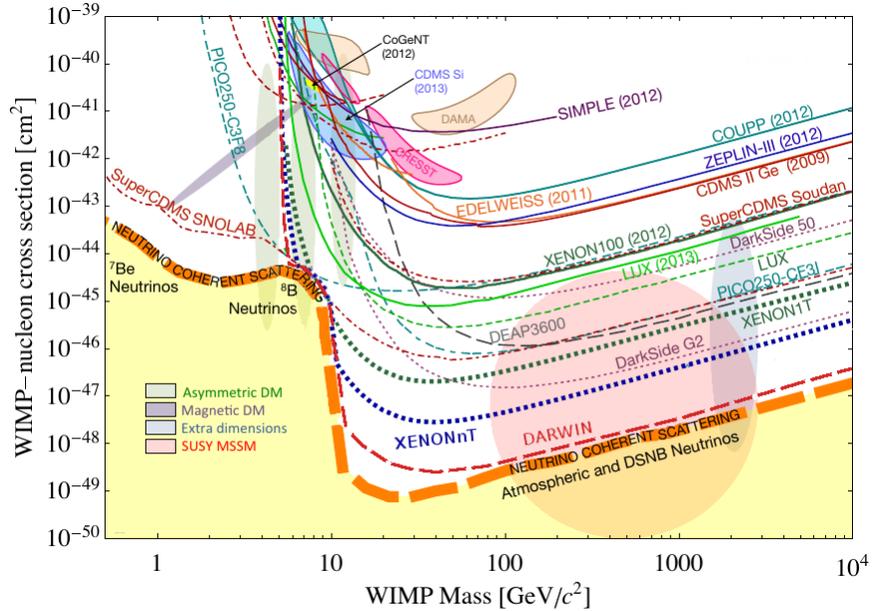
Figure 3.5: (Fig. 3 of Ref. [21], adapted from Fig. 26 of Ref. [13]) WIMP-nucleon spin-independent cross section limits (solid curves), hints for WIMP signals (shaded closed contours) and projections (dot and dot-dashed curves) for US-led direct detection experiments that are expected to operate over the next decade.

periments. In addition, the allowed regions are also not in agreement. Alternative models of WIMP-nucleon interaction, such as isospin violating dark matter where proton and neutron couplings to WIMP are different, were proposed to reconcile these observations. The
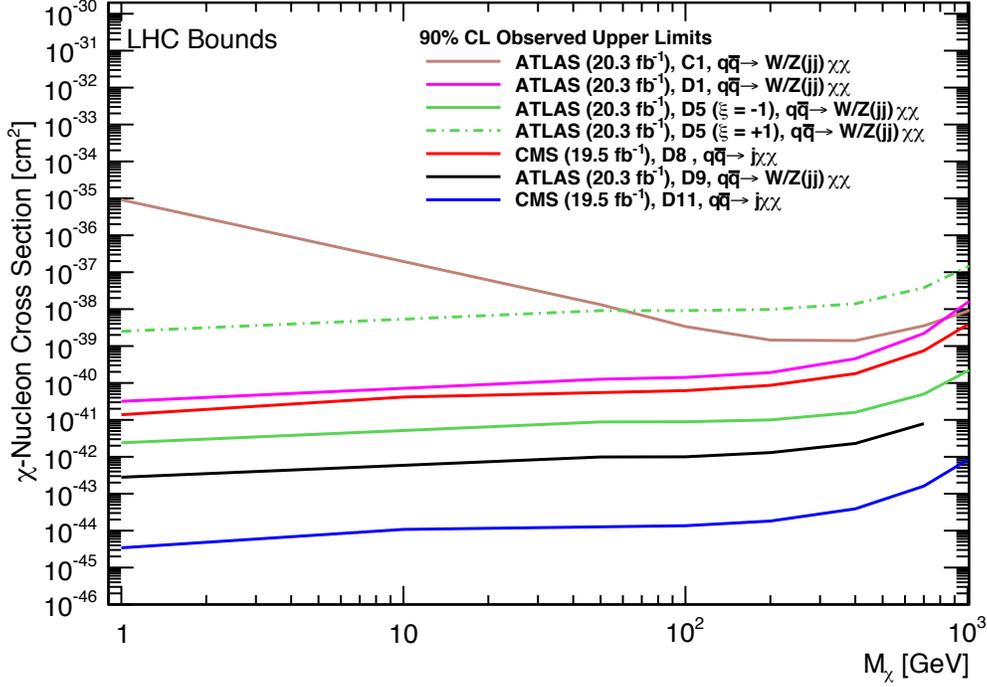
Figure 3.6: (Fig. 20 of Ref. [24]) The current bounds on upper limit for dark matter-nucleon cross section for different dark matter operators from collider searches with different final state.

observed excess nuclear recoil events in CoGeNT, CRESST, and CDMS-Si detectors fueled an interest in low mass WIMPs, altough these signals are not statistically different from the expected background.

The collider searches at the LHC have not found any evidence of dark matter production. In the ATLAS and CMS experiments, analyses using jets, photons and W/Z bosons have been performed with more final states yet to be analyzed [24]. Fig. 3.6 presents the current status of WIMP-nucleon cross section upper limit from mono-jet and mono-W/Z searches for different dark matter operators.

The collider search has also placed tight constraints on the low mass WIMPs that are products of Higgs boson decay. Measurements of Higgs boson properties and dedicated searches of missing transverse momentum performed by the ATLAS and CMS collabora-
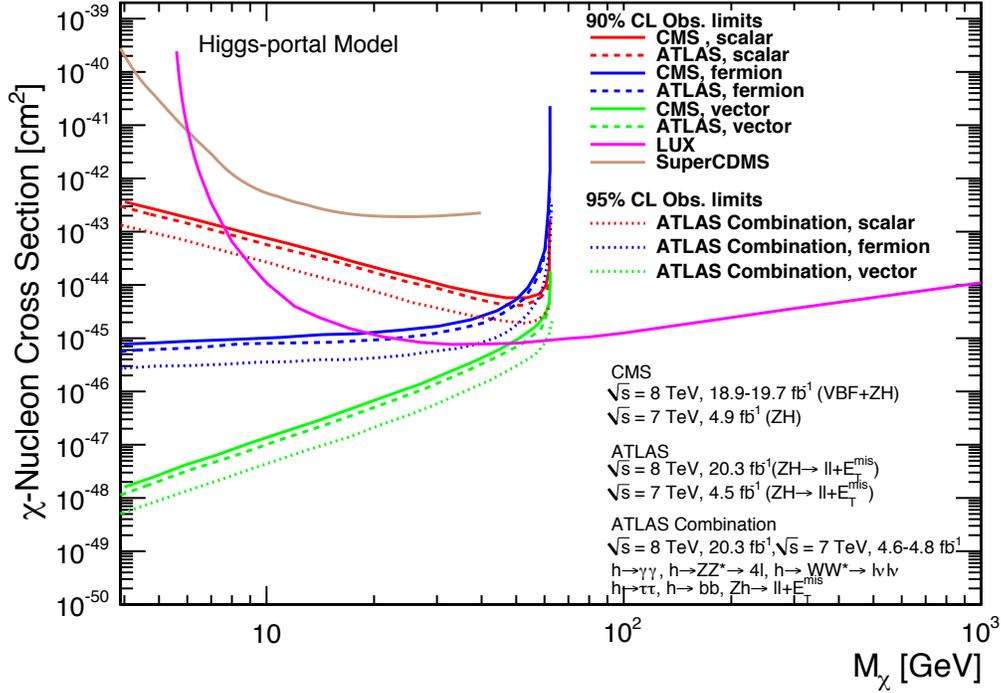
Figure 3.7: (Fig. 18 of Ref. [24]) Observed 90% CL upper limit for WIMP-nucleon cross section with scalar, vector and Majorana DM particle from $Z(\to \ell\ell)H$ final state.

tions lead to constraints on the $H \to invisible$ branching ratio and therefore couplings to WIMPs [24]. Fig. 3.7 shows the upper limits for scalar, vector, Majorana fermion WIMP candidates reported by the two collaborations.

The latest results of the direct detection, considered in the context of the limits provided by the LHC, points to a continued need for probing lower cross sections and therefore for the R&D and the deployment of larger direct detection detectors. In the next chapter, I describe the DarkSide program and outline its attractive design features as a promising contender of the ultimate mega scale WIMP detectors.

Chapter 4

The DarkSide program

In this chapter, I introduce the liquid argon time projection chamber (LAr-TPC) technology and briefly report the current status of the DarkSide[1] program.

4.1 LAr-TPC

Similar to LXe, LAr scintillates in the vacuum ultraviolet (VUV) range and produces free charge carriers in response to radiation [25]. Studies of β/γ radiations, α-particles and relativistic heavy ions have shown that the charge and light signals in both LAr and LXe are highly complementary and anticorrelated. When detected simultaneously and with high efficiency, the two signals enable a precise measurement of the particles properties from its deposited energy to its interaction position, time and type.

A typical dual-phase LAr or LXe TPC, as shown in Fig. 6.3, detects the scintillation photons (S1) with the photomultiplier tube (PMT) array. For LAr, the low wavelength (peaked at ~ 128 nm) of the S1 photons demands the use of wavelength shifter with commercially available PMTs (for detailed discussions on the choice of wavelength shifter, see Chapter 3.1.1 of Ref. [12]). The applied uniform electric field causes the free electrons to drift verti-

---

[1]The program name DarkSide was derived from the acronym DArCSciDE (depleted argon chamber for scintillation and drifted electrons).
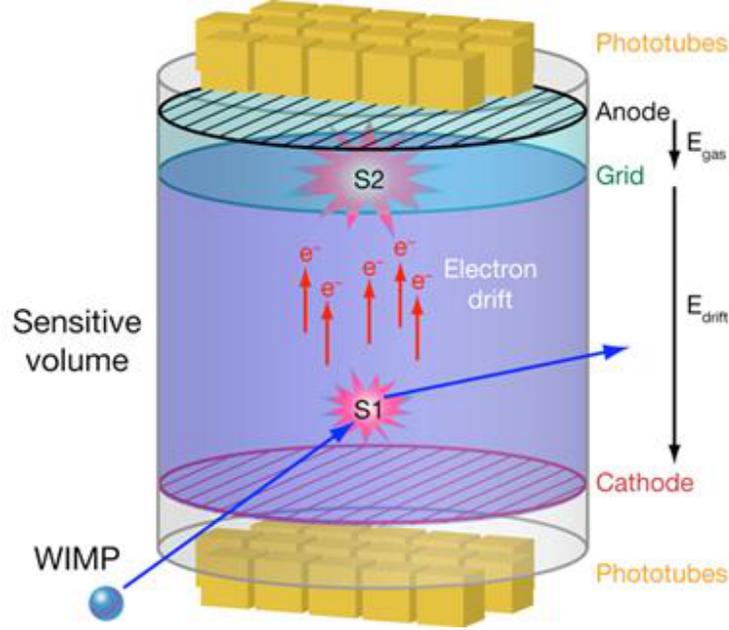
Figure 4.1: (Fig. 14 of Ref. [13]) Schematic of a dual-phase LAr or LXe TPC.

cally towards the anode, and the electric field between the anode and the grid extracts the electrons from the surface of the liquid. The extracted electrons produce electroluminescent light (S2) in the Ar gas, which is again captured by the PMT array. S2 is proportional to the number of drifted electrons. The free Ar ions drifts towards the cathode, but at a speed roughly one thousand times slower than the free electrons.

The choice of LAr as WIMP targets is motivated by the good separation of nuclear recoil events, as expected of WIMP interactions, from electron recoil events in LAr. For every event, scintillation pulse shape provides a strong first level discrimination and the scintillation-to-ionization ratio supplies a moderate additional discrimination. The high photon yield ($\sim$40000 photons/MeV for $1\,$MeV electrons at null electric field), the optical transparency to its own light, and the ease to drift free electrons are the crucial properties of LAr that enable the good discrimination.
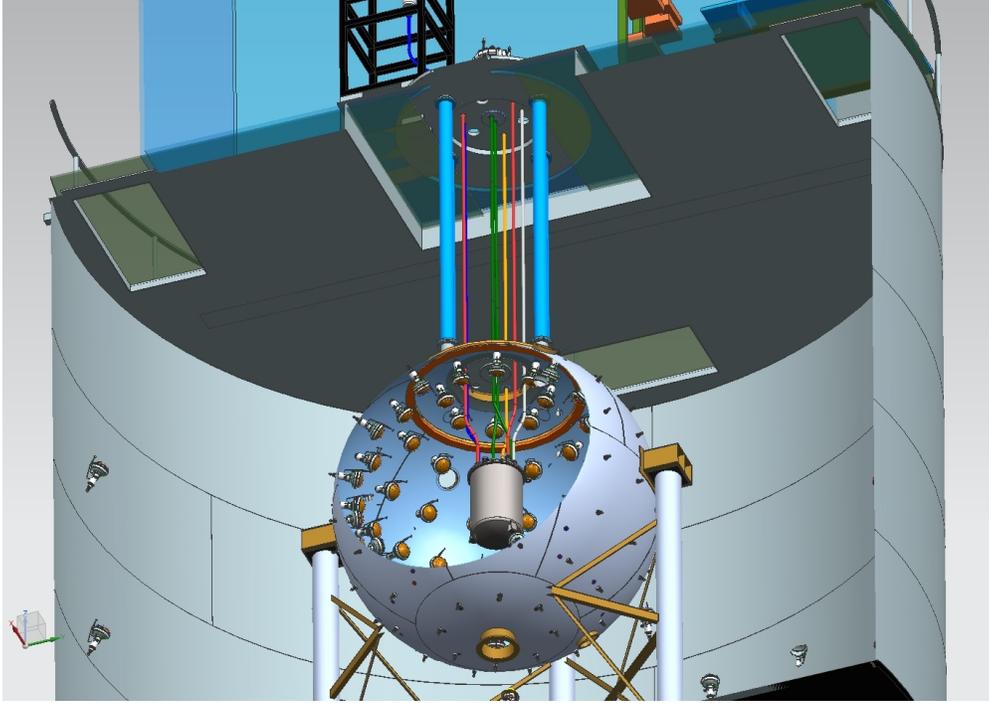
Figure 4.2: The nested detector system of DarkSide-50. The outermost dark grey cylinder is the water-Cerenkov veto, the sphere is the liquid scintillator neutron and γ-ray veto, and the dark grey cylinder at the center of the sphere is the LAr-TPC.

4.2 The status of DarkSide-50 experiment

The DarkSide-50 collaboration is operating a two-phase TPC with a 50 kg LAr target in the underground facility of Laboratori Nazionali del Gran Sasso (LNGS). The TPC, as shown in Fig. 4.2, is enclosed first by a 4 m-diameter spherical organic liquid scintillator detector, designed to veto neutrons and gamma rays, and next by a 11 m-diameter by 10 m-high cylindrical water Cherenkov detector, for vetoing the residual cosmic ray flux and passively shielding the external neutrons. The entire underground facility is shielded by 3600 meter water equivalent of rock, where the muon flux is suppressed by six orders of magnitude with respect to sea level. DarkSide-50 not only will demonstrate the background suppression efficiency of LAr-TPC, but will have the potential to provide a significant physics reach of $10^{-45}\,\text{cm}^2$ in the WIMP cross section at $100\,\text{GeV/c}^2$ mass in 0.1 ton $\times$ year exposure.

The DarkSide-50 experiment has dedicated a notable effort to reduce the expect backgrounds to a level of $\lesssim 0.5$ counts over three years after all cuts [11]. The sources of background in DarkSide-50 include radioactive contaminants in the detector components, surface α-decays, cosmic-ray muons - the common background types discussed in Sec. 3.2 - and ^{39}Ar, a β-decay with long half life ($\tau_{1/2} = 269$ years and Q-value $= 565$ keV), intrinsic to liquid argon.

The entire DarkSide-50 TPC achieved remarkable radiopurity. PMTs are usually the largest source of radiogenic neutrons in a noble liquid detector. The use of low-background PMTs (3" Hamamatsu R11065) for the TPC mitigated this background to a minimum level. The building materials used in the other components of the TPC were selected for their low radioactivity. Samples of each material passed a stringent screening of their ^{238}U and ^{232}Th activities. Futhermore, the TPC assembly was performed entirely in a clean room with radon suppressed air, thus minimizing the level of ^{210}Po α activity due to ^{210}Pb plating on the surfaces of the sensitive volume.

Passive neutron shielding scheme, common to existing WIMP direct detection experiments, was replaced with an active veto in the DarkSide-50 design, as the passive shield is ineffective in reducing the neutron background emerging internally from the detector components, or in attenuating external high energy cosmogenic neutrons. The liquid scintillator in the neutron veto is a 1:1 mixture of TriMethylBorate (TMB) and a solution of PPO (2,5-Diphenyloxazole) - a wavelength shifter - in PseudoCumene (PC). A significant portion of faster neutrons can be tagged by exploiting scintillation from elastic scattering of neutrons on protons. In addition to this scintillation, once the neutron thermalizes in the liquid scintillator (in ~ 100 ns), it is efficiently captured by ^{10}B in TMB, a result of the large thermal neutron capture cross section of ^{10}B and its natural abundance of 20%. Neutron capture on

boron triggers one of the two following reactions:

$$^{10}\mathrm{B} + n \xrightarrow{6.4\%} {}^{7}\mathrm{Li}\,(1015\,\mathrm{keV}) + \alpha\,(1775\,\mathrm{keV}) \tag{4.1}$$

$$\xrightarrow{93.6\%} {}^{7}\mathrm{Li}^{*}\,(839\,\mathrm{keV}) + \alpha\,(1471\,\mathrm{keV}),\ {}^{7}\mathrm{Li}^{*} \to {}^{7}\mathrm{Li} + \gamma\,(478\,\mathrm{keV}) \tag{4.2}$$
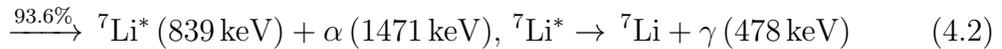
The α-particles have a short range in the liquid. After quenching, it can produce scintillation equivalent to $60\,\mathrm{keV}_{ee}$ (electron-equivalent energy). At a light yield of 0.5 photoelectrons per keV_{ee} ($\mathrm{PE/keV}_{ee}$) currently measured in the scintillator detector, the neutron capture events can be detected with around at least $30\,\mathrm{PE}$. For the branch with γ-ray production, If the γ-ray interacts in the liquid before escaping, the observed signal can be even greater. The scintillator cocktail thus allows an efficient neutron detection.

$^{39}\mathrm{Ar}$ is mainly formed in the atmosphere by cosmic neutron activation on $^{40}\mathrm{Ar}$ - the third most common gas in the Earth's atmosphere, at $\sim 1\%$ by volume. $^{39}\mathrm{Ar}$ is present with relatively high concentrations (8.0×10^{-16} with respect to $^{40}\mathrm{Ar}$ [26]) and produces a β-decay activity of about $1\,\mathrm{Bq/kg}$ in commercial liquid argon, the distillation product of liquid air. Although the PSD capability of LAr only has an inefficiency of 10^{-8} in rejecting electron recoil events, the level of $^{39}\mathrm{Ar}$ activity in atmospheric argon limits the size of argon-based WIMP detectors and restricts the sensitivity at low energies [27]. To reduce the $^{39}\mathrm{Ar}$ background, the DarkSide collaboration extracted underground argon (UAr) from a CO_2 well in Colorado [28]. This source of UAr contains less than 0.65% of the $^{39}\mathrm{Ar}$ activity in atmospheric argon.

The first year of DarkSide-50 data-taking started in October 2013. Major efforts have been devoted to fully characterize the three nested detectors. At this initial stage, the TPC has been filled with atmospheric argon. The run with underground argon is going to start in 2015.

Chapter 5

Past studies of nuclear recoils

As I have reviewed in Chapter 3, the expected WIMP signals in the direct detection experiments are in the form of nuclear recoils - nuclei scattered by WIMP. In order to infer the WIMP mass and interaction cross section (or its upper limits in the case of null result), which are the principal measurement objectives for all WIMP direct detection experiments, each experiment must perform a careful calibration of its detector's response to nuclear recoils.

Calibrations of nuclear recoils offer two important pieces of information for WIMP direct detection experiments: (1) the energy scale of nuclear recoils, and (2) the discrimination power against the backgrounds of the detectors. Those calibration data are the inputs for calculating the accepted fraction of nuclear recoils as a function of energy in the WIMP detectors. The uncertainties in these measurements for nuclear recoils can directly translate to the uncertainties in the interpretation of WIMP direct detection results, therefore precise calibration results are important for resolving the tensions currently exist among the WIMP direct detection experiments, especially in the low WIMP mass region.

In the cases of liquid noble gas detectors, the observable signals of nuclear recoils that require calibration, are in the modes of scintillation and ionization, as mentioned in Sec. 3.2 and 4.1. The calibration results of those modes in liquid argon are the main accomplishments of this thesis work. These results are applicable to LAr-TPCs that measure the two modes

simultaneously, or to LAr scintillation only or ionization only detectors, that detect the signals in just one of the two channels. In this chapter, I survey the experimental methods of nuclear recoil studies and review the results obtained for noble liquid detectors which are pertinent to the DarkSide program.

5.1   Methods of study

The key to a successful nuclear recoil study is the ability to select single nuclear recoil events with good knowledge of their kinetic energies. A few experimental techniques exist in the literature for studying nuclear recoils with kinetic energies of $\lesssim 100\,\mathrm{keV}$ in a particle detector, but each technique has its limitations.

5.1.1   Calibration with neutron beam

The canonical method uses a mono-energetic neutron beam to create nuclear recoils in a calibration detector. A typical calibration detector is a few centimeters in each dimension and features a design with as little material as possible along the path of neutrons to reduce the chance that neutrons scatter another time before or after their interaction in the active volume of the detector. The nuclear recoil energy is determined by tagging the elastically scattered neutrons with fast neutron detectors positioned at known angles. Ref. [29, 30] (the SCENE experiment described in this thesis) and Ref. [31, 32] presented the results of this method for nuclear recoil studies in LAr, Ref. [33–35] in liquid xenon (LXe), Ref. [36, 37] in high-purity Ge, Ref. [38–41] in Si crystal, Ref. [37, 42–47] in NaI(Tl) crystal, Ref. [48] in CaF$_2$ crystal, Ref. [49] in stilbene crystal, and Ref. [50] for protons and ^{12}C in KamLAND liquid scintillator.

Beam associated γ-ray background is a major challenge in studying nuclear recoils with this method. For WIMP detectors with nanosecond scale time resolution, time of flight (TOF) can effectively separate neutrons from γ-rays. A second challenge is in lowering the

nuclear recoil energies to the threshold ($\sim$ a few keV) of the calibration detector. Reducing the angle of the neutron-tagging detector can reduce the tagged nuclear recoil energy, but it would increase the fractional uncertainty of the recoil angle and therefore increase the uncertainty in the recoil energy. To retain a good angular precision, a low energy neutron beam of a few 100 keV or lower should be used. Such a neutron source can be obtained with the reaction $^7\text{Li}(p, n_0)^7\text{Be}$ [51]. This source triggered by a pulsed proton accelerator was exploited in Ref. [36, 39–41, 44, 48, 49] and this work.

D-D neutron generator (deuterium onto a deuterated target) was another popular choice among those studies. It produces relatively high energy neutron at $\sim$2.4 MeV (like other monochromatic sources, the neutron energy depends on the emission angle). Besides large uncertainties for small recoil energies, the large neutron energy of the D-D generator will also result in inelastic scatterings of most targets. Despite of these disadvantages and a lack of neutron bunching, not requiring the use of a proton accelerator makes the setup of the experiment more convenient. Our collaborator Prof. Martoff from Temple University is currently developing a D-D generator with the capability of detecting the ^3He nucleus emitted in the opposite direction of the neutron. This will allow TOF measurement from the neutron source to the calibration detector. This TOF has been shown to be an effective event selection tool for studies with pulsed neutron beams, so it may greatly improve the signal-to-noise for the measurements using D-D generators.

A variation on this method does not require the use of neutron tagging detectors. The full nuclear recoil spectrum is recorded and the calibration is determined using the correspondence between the end point of the nuclear recoil energy spectrum and the end point of the detector's response spectrum. Both end points are given by the elastic backscatter of the incident neutrons. This technique does not require the detector to bear good timing resolution for TOF selection, but a background subtraction is necessary for determining the end point. Measuring or modeling the background sometimes is a difficult task and subject

to many uncertainties. Ref. [52] gives an excellent example of the results obtained with this technique, for ionization yield measurements in LAr.

5.1.2   Alternative methods with neutron sources

In recent years, the particle physics simulation libraries have become increasingly accurate for modeling low energy neutron interactions in matter [53, 54]. The full simulation of neutron source exposures to the large underground WIMP detectors, either with a monoenergetic neutron source, such as the D-D generator and ^{88}Y/Be [55], or with a broad spectrum neutron source, such as ^{252}Cf and ^{241}AmBe, can be used to compare with actual spectra from data. Due to the large sizes of those detectors compared to the neutron mean free path, both the data and the Monte Carlo simulations include single- and multiple-interaction events within the spectra. Fitting the experimentally obtained spectra to the simulated spectra allows the extraction of crucial energy scale calibration factors such as scintillation, ionization or phonon yields of the WIMP detectors. Good position reconstruction capability of the current generation WIMP detectors make it even possible to exclude multiple interaction events from the data [56]. The drawback of this method is the lack of features in the spectra of neutron energy deposition, as the neutron interactions are dominated by elastic scattering. The uncertainties in many inputs of the simulation, for instant the neutron-nucleus differential cross sections and the WIMP detector trigger efficiencies at near threshold energies, limits the precision of those energy scale calibrations.

Recently, some preliminary results from the LUX collaboration suggested that, with a collimated mono-energetic source of neutrons, one can use the reconstructed positions of twice-scattered neutron events to determine the nuclear recoil energy of the first neutron scatter in a large LXe-TPC [57]. This seems a promising method to calibrate ionization signals in large LXe or LAr-TPCs, but the scintillation signals of the two scatters cannot be resolved. It is also worth noting that this scheme can be applied successfully only if there is a short path for neutrons to enter the sensitive volume. The spread in the direction and

kinetic energy of the incoming neutrons and the uncertainties in the position reconstruction eventually limit the precision of the results.

In addition to elastic scattering, neutrons can have inelastic interaction with WIMP targets. A good example is the Ge nuclei[37, 58, 59]. The first excited states of several Ge isotopes have high inelastic scattering cross-section. The products of such a collision are: (1) a nuclear recoil with a kinetic energy inferior to that associated with elastic scattering, (2) a scattered neutron with a reduced energy and thus an increased time-of-flight to the neutron tagging detector, and (3) a γ-ray emission that may deposit some of its energy in the detector. As most of the γ-ray escape detection, these experiments rely on neutron TOF to discriminate these events from elastic scatters or deexcitation of other levels. Also worth noting in Ge, a calibration of $254\,\mathrm{eV}$ ^{73}Ge recoil is also possible with a beam of thermal neutrons through ^{72}Ge(n, γ)^{73}Ge reaction [60].

5.1.3   Exotic method

For bubble chambers with CF_3I as target, neutron sources are ineffective tools for calibrating iodine recoils, as the iodine recoils contribute only a small fraction to the total neutron-nucleated bubble rate. The COUPP collaboration developed a technique with the elastic scattering of $12\,\mathrm{GeV}/c$ negative pions for measuring the threshold and efficiency for bubble nucleation from iodine recoils [61]. This technique is suitable for bubble chambers, as they are insensitive to γ-ray photons.

5.2   Previous measurements in noble liquids

5.2.1   Liquid argon

Before the SCENE experiment, the scintillation yield of nuclear recoils in LAr was measured only under zero applied electric field. A summary of all previous measurements was shown in Fig. 5.1. In Ref. [31, 32], the measurements of scintillation yield were performed with 2.8
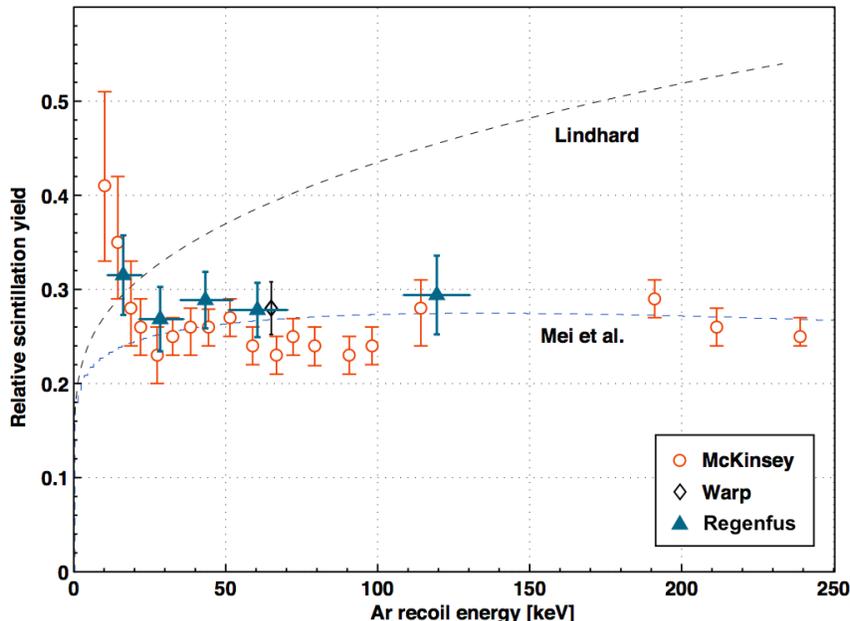
Figure 5.1: (Fig. 8 in Ref. [32]) Values for scintillation efficiency of nuclear recoils in LAr relative to scintillation efficiency of electron recoils at the 122 keV line of ^{57}Co. There is no applied electric field.

and 2.45 MeV neutrons from D-D neutron generators, so at energies below ∼25 keV, *i.e.*, at scattering angles smaller than ∼35°, the uncertainty of the angle is a significant source of error. In addition, the LAr chambers used in both experiments had relatively large diameters, as a result, a large fraction of neutrons scatter multiple times in these LAr detectors. Due to the smallness of momentum transfer in each neutron-nucleus interaction, the TOF technique is ineffective in distinguishing single-scatter from multiple-scatter events. Reducing the size of the detector is the only general tactic for lowering the multiple-scattering background in the calibration results. It is worth noting the suspicious rise of the scintillation yield with the decrease of recoil energy in the previous measurements. A drop in the trigger efficiency with the decrease of energy could result in a cut-off of events at low energies. If the trigger efficiency was over-estimated at low energies, the cut-off could shift the peak of the nuclear recoil spectrum to a higher position and bias the measured scintillation yield.

For ionization yield, there was no dedicated measurement available for nuclear recoils in the energy range relevant to WIMP search before SCENE. A group mainly from University
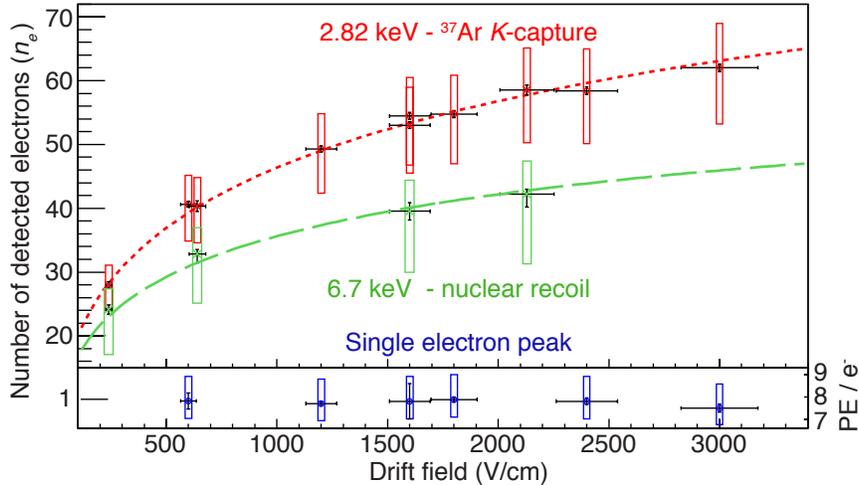
Figure 5.2: (Fig. 4 in Ref. [52]) Number of observed electrons from 2.82 keV electronic recoils and 6.7 keV nuclear recoils are shown at different drift fields in the upper frame. Statistical uncertainties are indicated with error bars, systematic uncertainties with error boxes. The dotted curve shows the best fit modified Thomas-Imel model (see original text) fit to 2.82 keV electronic recoil data. The dashed curve shows the best fit modified Thomas-Imel model fit to 6.7 keV nuclear recoil data. The single electron peaks used with 2.82 keV data to infer the single electron calibration for endpoint data are shown in the lower frame.

of California, Berkeley and Lawrence Livermore National Laboratory (LLNL) recently (and concurrently with SCENE) measured it at 6.7 keV nuclear recoils (see Fig. 5.2) using the end point of the recoil spectrum in a TPC [52].

The objectives of the SCENE experiment were hence set on filling the void in the measurements of both the scintillation and ionization yield of nuclear recoils in liquid argon and in the characterizations of the effects of applied electric field on the scintillation and ionization yields and on the pulse shape discrimination.

5.2.2 Liquid xenon

Only LXe and LAr among liquid rare gases produce both charge carriers and scintillation photons in response to radiation [25]. Other physical properties of LXe, such as the ability to drift radiation induced electrons and holes due to the existence of a conduction band, are also similar to LAr. Thus unsurprisingly for a variety of particles, the scintillation and
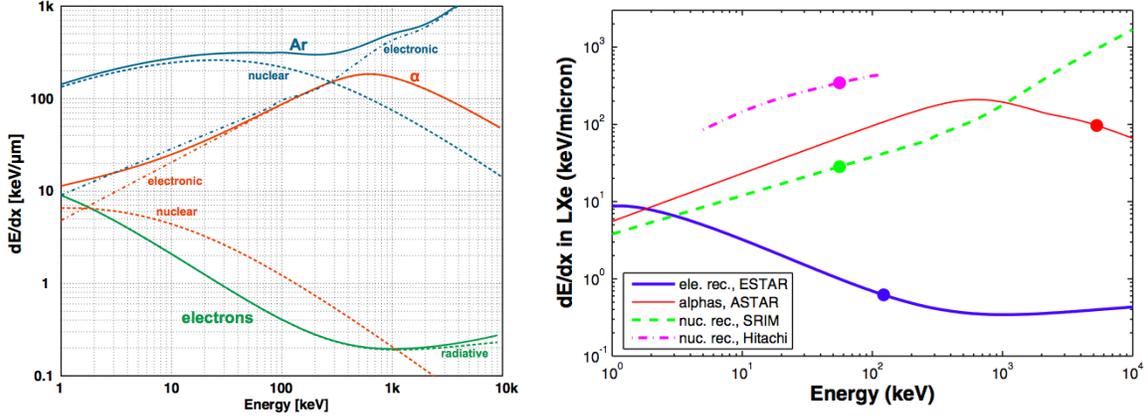
Figure 5.3: Left: (Fig. 4 in Ref. [32]) Predicted total stopping power (solid lines) and contributions (dashed lines) for Ar ion, electron and α-particle in LAr. Right: (Fig. 5 in Ref. [62]) Predicted electronic stopping power for Xe ion, electron and α-particle in LXe.
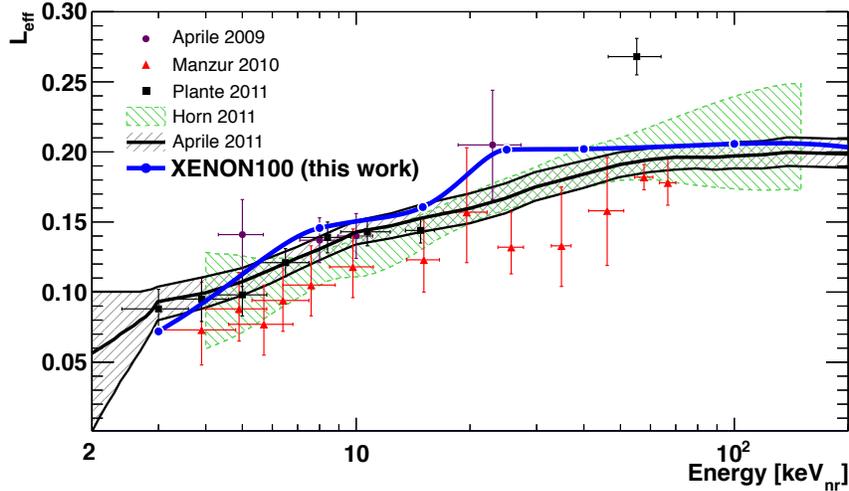
Figure 5.4: (Fig. 5 in Ref. [56]) Scintillation efficiency of nuclear recoils in LXe relative to scintillation of electron recoils at the 122 keV line of ^{57}Co. Aprile 2009, Manzur 2010, Plante 2011 were obtained from calibration detectors at zero drift field, the others were calculated from comparing Monte Carlo simulations with data taken with drift field. Earlier measurements can be found in [34].

ionization yields share the same qualitative dependence on linear energy transfer, drift field and deposited energy [25, 63]. Given the similarity in the dependence of the stopping power of Ar and Xe ions in LAr and LXe respectively (see Fig. 5.3), we expect an analogous dependence of scintillation and ionization yields on nuclear recoil energy.
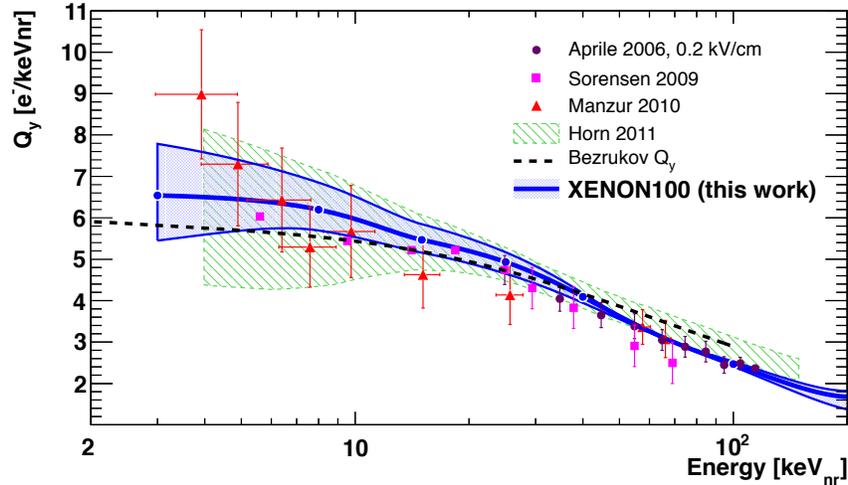
Figure 5.5: (Fig. 3 in Ref. [56]) Ionization yield of nuclear recoils in LXe. Data taken under a range of different drift fields.

The most recent nuclear recoil measurements in a calibration detector[33–35] and in XENON100 and ZEPLIN-III detectors are shown in Fig. 5.4 and 5.5. The measurements taken with small calibration detectors were obtained at zero drift field. For the scintillation efficiency with drift field, there is one precise measurement at $56.5\,\mathrm{keV}$ [64] and a set of measurements at lower energy with poor precision [35]. It has lead to a common assumption used by the XENON collaboration that the presence of drift field has a small effect on the scintillation efficiency. If this assumption is false, it could modify the WIMP cross section limits set by LUX and XENON experiments in the low WIMP mass region. Precise measurements of the scintillation efficiency with and without drift fields is therefore a crucial task for the interpretation of current and future LXe-TPC results.

Fig. 5.5 shows the ionization yield of nuclear recoils in LXe. The increase of ionization yield with the decrease in recoil energy is generally considered an effect of reduction in the recombination of electron-ion pairs produced by recoiling nuclei. This effect also explains the corresponding decrease in the scintillation yield. The ionization yields were acquired under a few different drift field values, but the existing data show no clear trend for a dependence on the drift field. It is necessary to point out that apart from the Manzur 2010 measurements, the energy scales of the ionization yield measurements were not determined

directly with kinematics, but were inferred from the scintillation signals. Hence, a direct and precise calibration will help validate the conclusion on field independence. This along with the determination of the field effect on scintillation are the goals of the LXe studies for the future phase of the SCENE experiment.

Chapter 6

SCENE LAr experiment geometry and apparatus

The SCENE collaboration[1] used a monoenergetic neutron beam to characterize scintillation (S1) and ionization (S2) signals produced by nuclear recoils between 10.3 and 57.2 keV in a LAr-TPC with and without an applied electric field. The results obtained with this study are relevant for the calibration and interpretation of data of LAr-TPC dark matter detectors [65–67]. They also lay the groundwork for a method that could be applied for the characterization of LXe-TPC [68–70] and other dark matter detectors. I describe in this chapter the experimental setup and the apparatus used in this experiment.

6.1   Geometry

The experiment was performed at the University of Notre Dame Institute for Structure and Nuclear Astrophysics in two runs in June and in October, 2013. Protons from the Tandem accelerator [71] struck a $0.20\,\mathrm{mg/cm^2}$ thick LiF target deposited on a 1-mm-thick aluminum backing generating a neutron beam through the reaction $^7\mathrm{Li(p,n)}^7\mathrm{Be}$. For the October 2013 run, a 0.1-mm-thick tantalum layer was interposed between the LiF target and aluminum

---

[1]See the description in Preface

backing to fully stop the protons before they reach the aluminum. This reduced the intensity of γ-ray background. The proton beam was bunched and chopped to provide pulses 1 ns wide, separated by 101.5 ns, with an average of 6.3×10^4 protons per pulse. The accelerator pulse selector was set to allow one of every two proton pulses to strike the LiF target, giving one neutron beam pulse every 203.0 ns. During the S2 studies, the pulse selector setting was modified to allow one of every four, five, or eight pulses. The settings for proton beam energy and scattering angle used in the two runs and the corresponding nuclear recoil energies explored are summarized in Table 6.1.

The TPC was located 73.1 cm from the LiF target in June and 82.4 cm in October. The average number of neutrons passing through the TPC per pulse was $\approx 3 \times 10^{-4}$. Scattered neutrons were detected in three EJ301 12.7$\times$12.7 cm cylindrical liquid scintillator neutron

	Proton Energy [MeV]	Neutron Energy [MeV]	Scattering Angle [°]	Nuclear Recoil Energy [keV]
	2.376	0.604	49.9	10.3 (10.8)
	2.930	1.168	42.2	14.8 (15.2)
Jun 2013	2.930	1.168	49.9	20.5 (20.8)
	2.930	1.168	59.9	28.7 (29.0)
	4.100	2.327	49.9	40.1 (41.5)*
	2.930	1.168	82.2	49.7 (49.9)
	2.316	0.510	69.7	16.9 (16.5)
Oct 2013	3.607	1.773	45.0	25.4 (26.1)*
	2.930	1.119	69.7	36.1 (36.3)*
	3.607	1.773	69.7	57.2 (57.6)*

Table 6.1: Proton energy, neutron energy, and scattering angle settings for the two runs. Note that the neutron production angle was 25.4° in June and 35.6° in October. To determine the nuclear recoil energy we performed a MC simulation of neutron scattering in our apparatus taking full account of all materials and the geometry of the detectors. The first value in the last column is the mean energy obtained by fitting the MC energy distribution with a Gaussian plus linear background. For interest, we also show a second value in parenthesis, the recoil energy calculated directly from the scattering angle using the center of the TPC and the center of the neutron detector. Datasets marked with an asterisk (*) were taken with the TPC trigger requiring the coincidence of the two TPC PMT's, see the text for details.
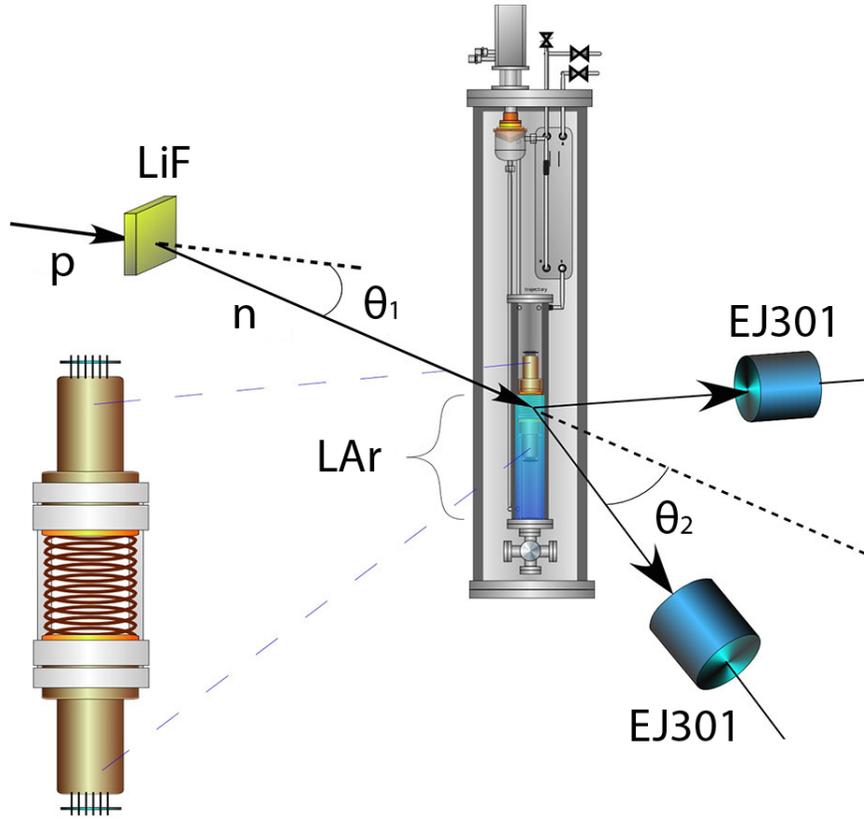
Figure 6.1: A schematic of the experiment setup (not to scale). θ_1 is the neutron production angle and θ_2 is the scattering angle. The inset shows a zoomed-in view of the TPC including the PMTs, field shaping rings and PTFE support structure. It does not include the inner reflector.

detectors [73]. These detectors were placed on a two-angle goniometer-style stand at a distance of 71 cm from the LAr target and at selected angles with respect to the beam direction. The angles determined both the energy of the nuclear recoils and the direction of the initial momentum of the recoils. Fig. 6.1 shows a schematic of the geometry along with a zoomed-in view of the TPC, Fig. 6.3b shows a photo of the full setup, and Table 6.1 lists the configurations of beam energy and detector location and the corresponding mean nuclear recoil energy in the TPC. The liquid scintillators provided timing information and pulse shape discrimination, both of which suppressed background from γ-ray interactions. Cylinders of polyethylene (22×22 cm) shielded the neutron detectors from direct view of the LiF target for all but the 49.7 keV data.
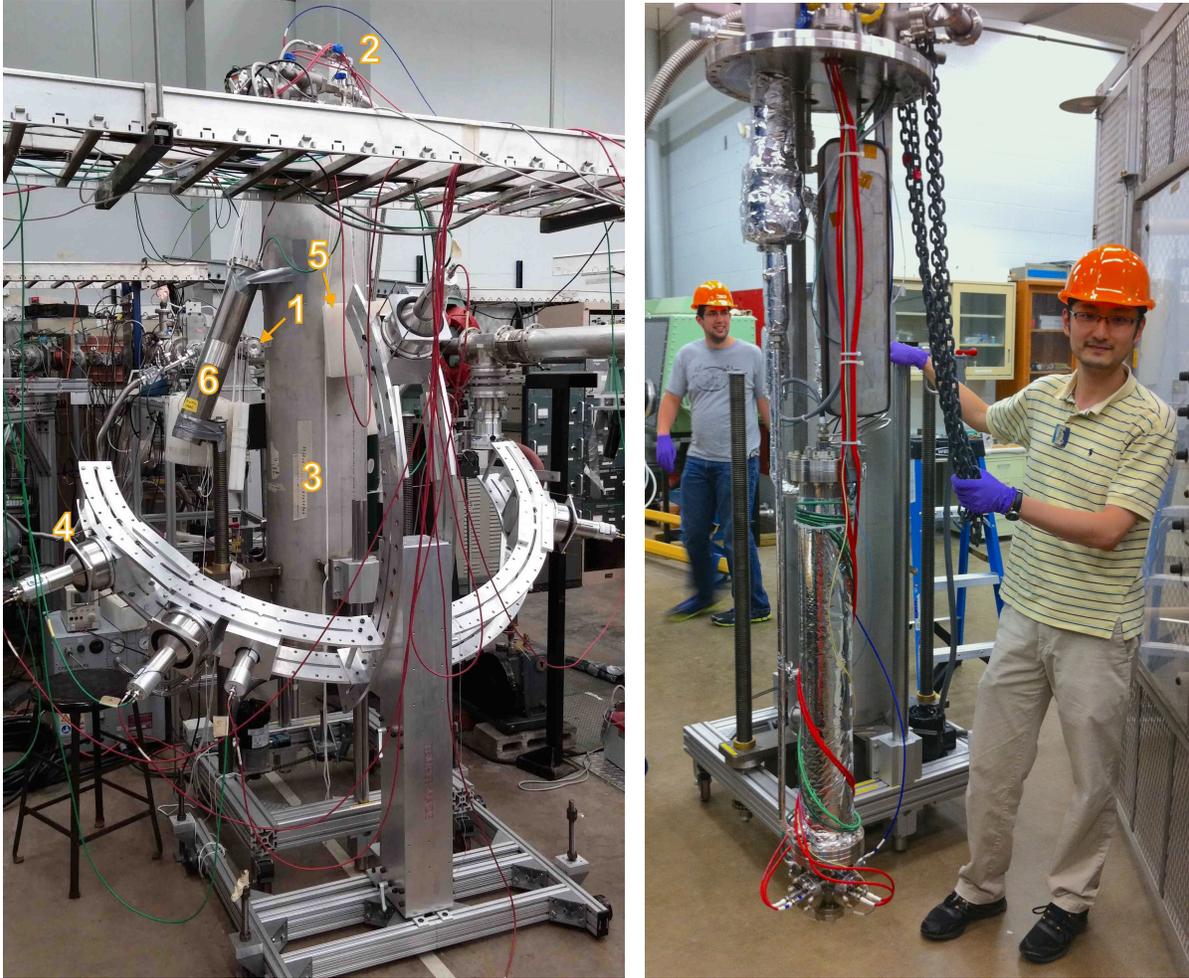
Figure 6.2: **Left:** Photo of the experimental setup at the Notre Dame accelerator lab. 1 - LiF target, 2 - LAr-TPC cryostat, 3 - LAr-TPC position, 4 - EJ301 neutron detector on the goniometer-style stand, 5 - Polyethylene cylinder for blocking direct neutrons from LiF target, 6 - NaI(Tl) detector from SABER experiment [72] for a preliminary nuclear recoil study.

Right: Photo of the LAr-TPC inner chamber. The high voltage feedthroughs for the PMTs and TPC electrodes are located at the bottom of the chamber, ensuring that most of the high voltage connections were submerged in LAr and the risk of electrical breakdown was minimized. The author is on the right and Thomas Alexander (University of Massachusetts, Amherst) is on the left.

6.2 TPC design

The design of the TPC closely followed that used in DarkSide-10 [67]. The active volume was contained within a 68.6 mm diameter, 76.2 mm tall, right circular polytetrafluoroethylene (PTFE) cylinder lined with 3M Vikuiti enhanced specular reflector [74] and capped by
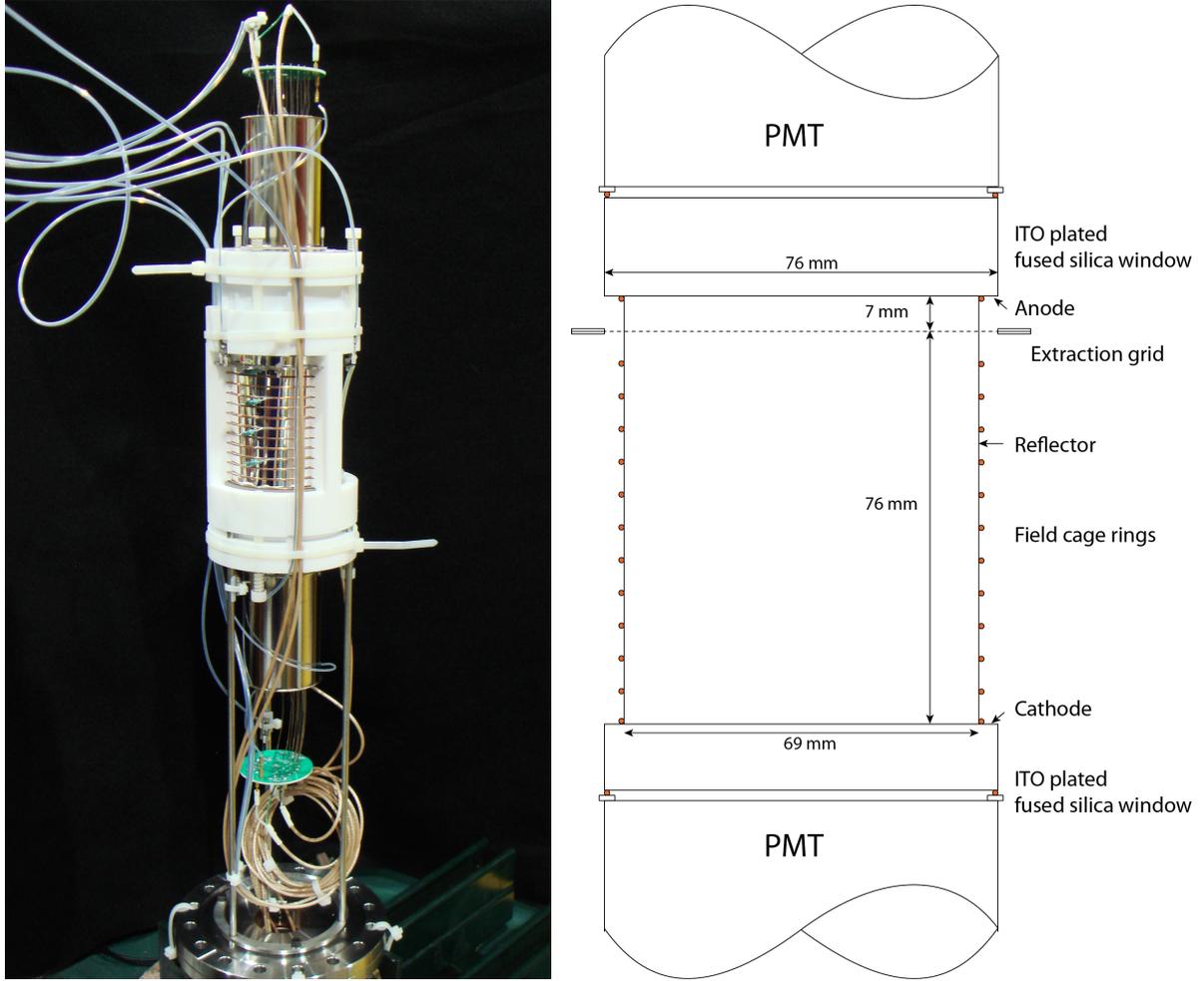
Figure 6.3: **Left:** Photo of the LAr-TPC before insertion into the inner chamber. **Right:** TPC sectional drawing.

fused silica windows (see Fig. 6.3). The LAr was viewed through the windows by two 3" Hamamatsu R11065 PhotoMultiplier Tubes (PMTs) [75]. The windows were coated with the transparent conductive material indium tin oxide (ITO), allowing for the application of electric field, and copper field rings embedded in the PTFE cylinder maintained field uniformity (see Fig. 6.4). All internal surfaces of the detector were evaporation-coated with the wavelength shifter TetraPhenylButadiene (TPB) which converted the LAr scintillation light from the Vacuum UV range (128 nm) into the blue range (∼420 nm). A discussion of the details on the evaporation-coating technique is included in Appendix G.
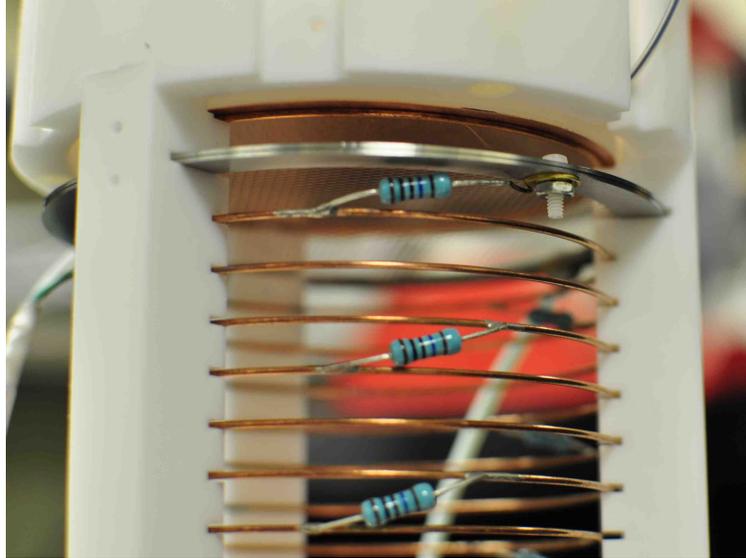
Figure 6.4: Close-up photo of the TPC, showing the stainless steel mesh, field cage, and PTFE support. The Vikuiti reflector is not installed and the anode window is replaced by a copper disk in this shot for clear view.
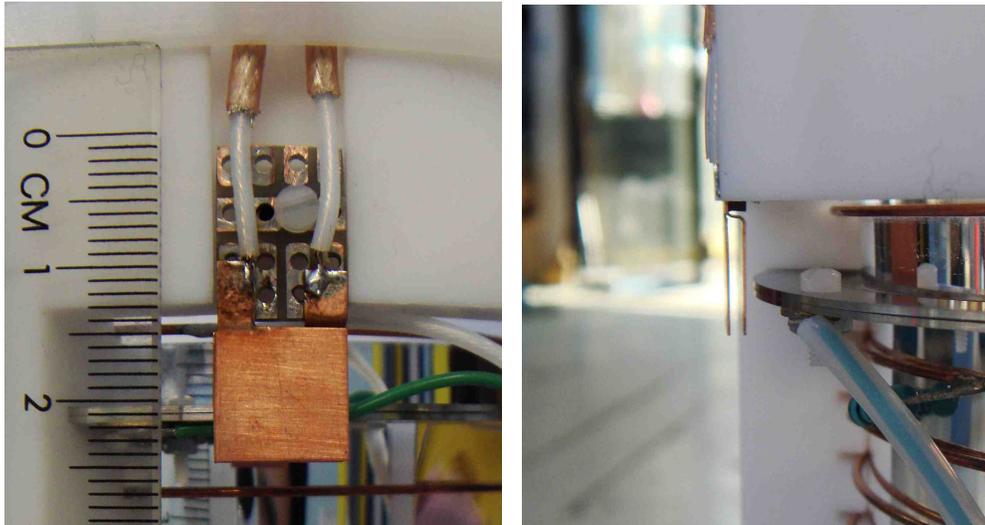
Figure 6.5: Photos of the parallel-plate capacitive level sensor.

A hexagonal stainless steel mesh was fixed at the top of the active LAr volume and connected to the electrical ground (see Fig. 6.4). The strips in the mesh were $50\,\mu$m wide, and the distance between the parallel sides in each hexagon was $2\,$mm. We maintained the LAr level at $2\,$mm below the mesh in June and $1\,$mm above the mesh in October by keeping a constant inventory of Ar in the closed gas system at stable temperature and pressure. We
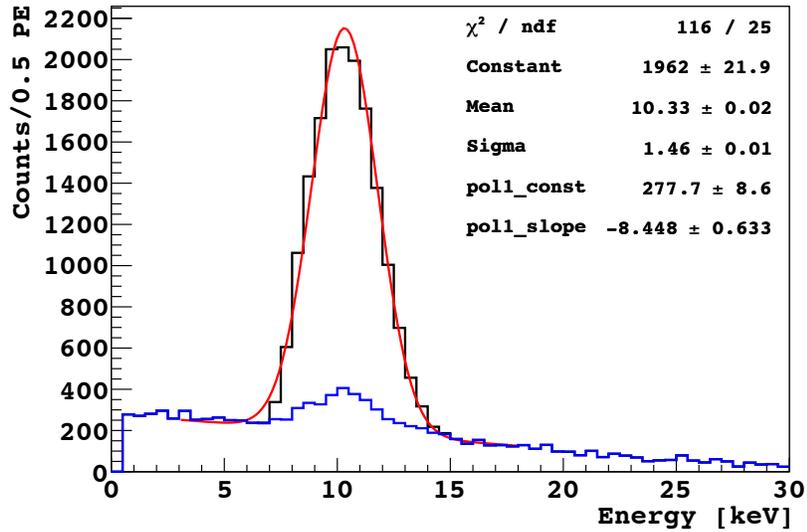
Figure 6.6: GEANT4-based simulation of the energy deposition in the LAr-TPC at the 10.3 keV setting. **Black:** all scatters that produced a coincidence between the TPC and the neutron detector and survived the timing cuts discussed in the text. **Blue:** from neutrons scattered more than once in any part of the entire TPC apparatus before reaching the neutron detector. **Red:** Gaussian plus first order polynomial fit to the black histogram.

monitored the liquid level with 3 pairs of 10 mm×10 mm parallel-plate capacitive level sensors, with radially symmetric positions along the circumference of the mesh (see Fig. 6.5). Ar gas filled the remaining volume below the anode (the ITO coating on the top window). The gap between the mesh and the anode was 7 mm in height. The electric potential difference between the cathode and the mesh set the drift field, and that between the anode and the mesh set the electron extraction field in the liquid above the mesh and in the electroluminescence region. The cathode and anode potentials were controlled independently. This allowed us to collected data with and without the ionization signals by switching on and off the voltage applied to the anode.

The diameter and height chosen for the liquid argon target allowed the acquisition of adequate statistics with an acceptable level of contamination from multiple scattering. Fig. 6.6 shows energy deposition distributions from a GEANT4 [53] simulation of 10.3 keV recoils[2];

---

[2]The GEANT4 simulation studies were performed by Yixiong Meng of University of California, Los Angeles.
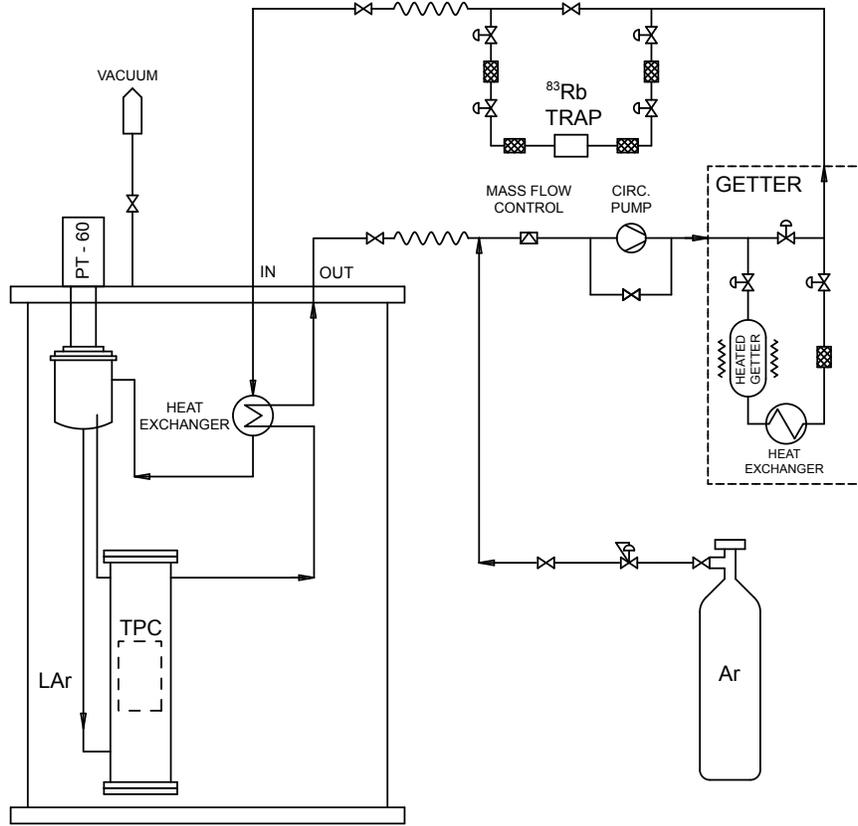
Figure 6.7: Ar gas system used for continuous purification of the LAr and injection of ^{83m}Kr source. The TPC chamber and the outer vacuum jacket are single-walled.

the multiple scattering contributes less than 32% of the total event rate between 5 and 16 keV, and the position of the single scattering peak is not affected by the background. We estimated the mean recoil energy for each configuration by fitting the MC energy distribution with a Gaussian plus linear background.

The argon handling system is shown in Fig. 6.7. The LAr detector was cooled by a Cryomech PT-60 [76] connected through a heater block to a condenser (see Fig. 6.8). Commercial argon gas (6 9's grade [77]) was recirculated through a SAES MonoTorr PS4-MT3-R1 getter [78] to remove impurities (mainly oxygen, nitrogen and water) from both the input gas and the LAr-TPC.
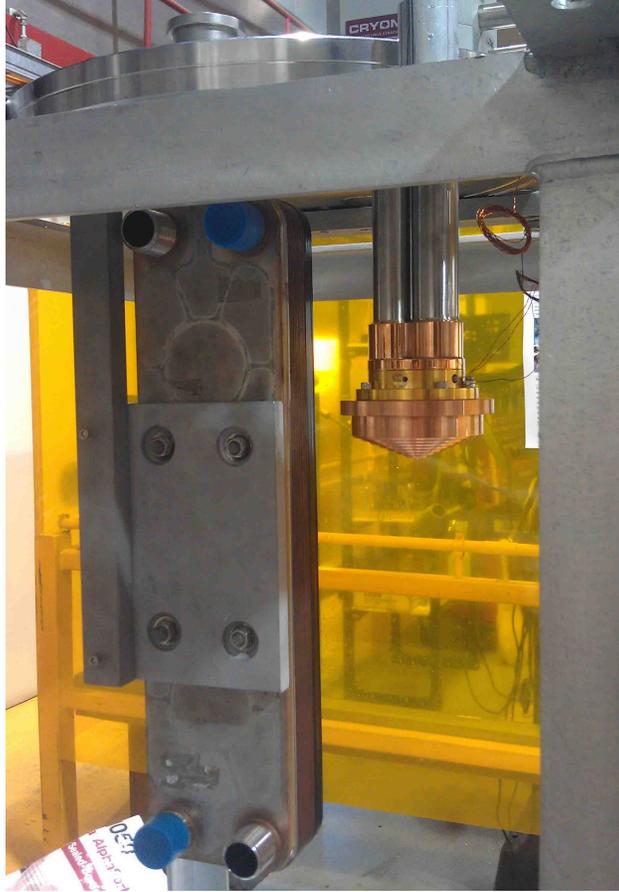
Figure 6.8: Photo of the cold-head on the right (before the attachment of the condensing canister) and input-output gas heat exchanger on the left.

6.3 EJ301 liquid scintillator neutron detectors

We chose the commercially available EJ301 liquid scintillator [73] as our neutron detection targets. EJ301 is identical to the NE-213 liquid scintillator, whose responses to radiation have been extensively documented in the references cited in Ref. [73]. Proton recoils, which is the main form of energy deposition of neutrons in this liquid scintillator, produces $\sim$ 1-2 scintillation photons per keV of kinetic energy in the range of $100\,\text{keV}$ to $1\,\text{MeV}$, assuring sufficient detection efficiency of proton recoils hence scattered neutrons in our experiment. The fast response of this signal is suitable for our time of flight (TOF) measurements at nanosecond level. Although only supplemental to TOF discrimination in our application,

the EJ301 liquid scintillator exhibits excellent pulse shape discrimination between γ-rays and fast neutrons.

6.4   Trigger and data acquisition

The experiment trigger required a coincidence of the TPC trigger with one of the neutron detectors. The TPC trigger was set as either the OR or the AND of the two TPC PMT's discriminator signals. In addition to the coincidence events, we recorded events triggered by the TPC alone, consisting largely of ^{83m}Kr events, at a prescaled rate of 12 Hz (5 Hz in October). The full schematic diagram of the trigger is shown in Fig. 6.9.

The discriminator thresholds of the TPC PMTs were set to $\sim$0.2 photoelectrons (PE). As shown in Fig. 6.10, the TPC trigger efficiency was determined to be above 90% for pulses above 1 PE with the OR trigger (above 10 PE with the AND trigger) using positron annihilation radiation from a ^{22}Na source placed between the TPC and a neutron detector, following the method described in Ref. [34]. Use of the AND trigger was limited to the recoil energies above 25 keV (marked with * in Table 6.1). See Section:8.2 for further details on the impact of trigger efficiency on S1 spectra.

The data acquisition system was based on 250 MSPS waveform digitizers [79], which recorded waveforms from the TPC, the neutron detectors and the accelerator RF signal. At the times when the TPC was operated without S2 production (i.e. with zero anode voltage), the digitizer records were 16 μs long including 5 μs before the hardware trigger (used to establish the baseline). At the times when the TPC was operated with S2 production, the length of the digitizer records was set to the maximum drift time plus 45 μs. The data were recorded using the in-house daqman data acquisition and analysis software [11, 80]. The analysis modules applied to the data stream included ConvertData (converts binary digitizer data to arrays and applying SER calibration), SumChannels (combines the waveforms of the two TPC PMT channels into a single waveform), BaselineFinder (separates the base-

Figure 6.9: Trigger scheme of the experiment. **Blue arrows:** analog signals. **Black arrows:** NIM logic signals.
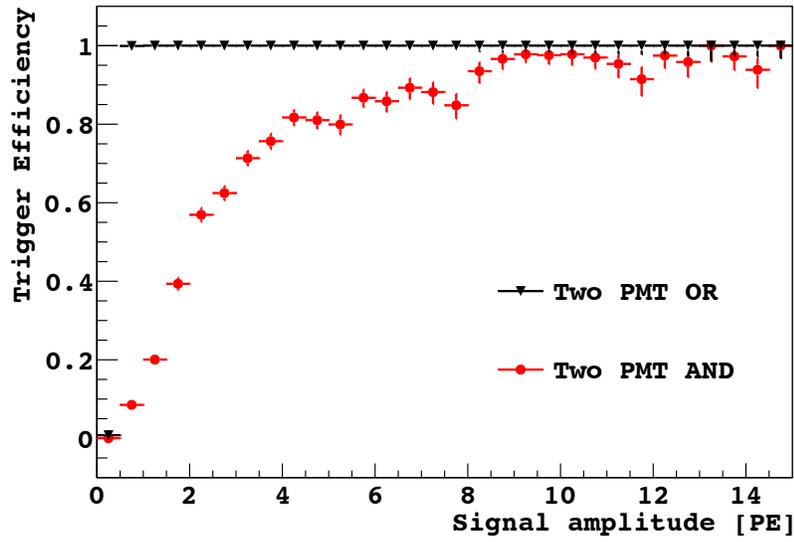
Figure 6.10: Efficiency for the two TPC trigger conditions described in the text. **Black:** OR of the two TPC PMT's. **Red:** AND of the two TPC PMT's. See text for description of the measurement of the efficiency.

line regions in each waveform from the regions containing photoelectron signals), EvalRois (evaluates relevant statistics for a chosen time window) and PulseFinder (identifies the start and end time for S1 and S2 signals) that were also utilized in the DarkSide-10 experiment. They are described in details in Ref [11]. A TimeOfFlight module was added specifically to compute the arrival time of the signals in the TPC and in the EJ301 detectors with respect to the periodic accelerator RF signal. See its description and usage in Sec. 8.1.

Chapter 7

TPC monitoring and calibration

The overall stability of the light yield was of critical importance to our measurements. Several systems, including the wavelength shifter, the reflector, the photosensors, and the electronics, determined the light yield and its variations. The stability of the temperature and pressure in the LAr-TPC must also be monitored constantly to prevent significant variations in the liquid level, which could affect the electron-extraction field and electron-multiplication field in the region above the mesh, and subsequently change the magnitude of S2 signals. I describe the methods we adopted for monitoring and calibrating each of those parameters listed in this chapter.

7.1 Temperature, pressure, and liquid level monitoring

The temperature of the LAr chamber was controlled through the electric power applied to the heater block that is attached to the PT-60 cryocooler cold-head. Along with the resistance temperature detector (RTD) on the cold-head and a Lake Shore Model 336 cryogenic temperature controller [81], they formed a closed-loop temperature control operating in proportional-integral-derivative (PID) mode. Two additional PT1000 RTDs were installed in the LAr chamber, one right above the bottom Conflat-600 flange monitoring the liquid temperature, and the other at the base of the top PMT monitoring the gas temperature.
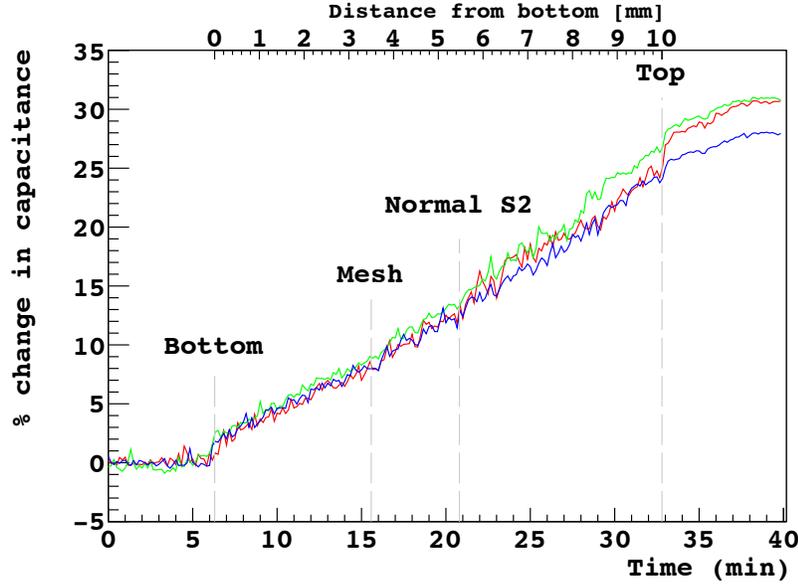
Figure 7.1: Calibration of the capacitive level sensors. Ar gas is being condensed at a constant rate of 2 slpm. The initial capacitance of the level sensors (Ar gas in the gap) are 1.57 (red), 1.69 (green) and 2.08 (blue) pF in this test. The discontinuities at 6.3 minutes and 32.8 minutes indicate the bottom and the top of the level sensors. The top axis is a liquid level calibration derived from those two calibration points. "Mesh" is the expected location of the mesh; "Normal S2" indicates the transition in S2 rise time.

The gas pressure inside the LAr chamber was checked with a MKS 750B pressure transducer [82] mounted downstream of the CAEN getter in the gas recirculation loop.

The liquid level was monitored with the capacitance read-out of the three parallel-plate capacitive level sensors shown in Fig. 6.5. Liquid Ar and gas Ar have different dielectric constant (1.5 versus 1), so an increase of the liquid level in the gap between the parallel plates corresponds to an increase in the capacitance of the level sensor. We used the Smartec Universal Transducer Interface (UTI) [83] to measure the capacitance of the parallel plates, which was about 1-2 pF. UTI is capable of subtracting the parasitic capacitance, which was much greater than a few pF, from the coaxial cable used for making the connections.

The result of a careful calibration of the the capacitance level sensors is shown in Fig. 7.1. We filled the LAr chamber by condensing a flow of Ar gas at a constant flow rate of 2 standard liter per minute (slpm) while recording the measurements of the capacitance (each point in Fig. 7.1 is a 10 s average) and monitoring the S2 ionization signals registered by

53

the PMTs. The pressure and temperature of the chamber were stable at such slow flow rate. The capacitance measurements showed clear discontinuities at 6.3 minutes and 32.8 minutes, indicating the times when the LAr liquid level hit the bottom of the level sensors and when it rose above the top of the sensors. This gives us two calibration points of the level sensors. As the flow rate was constant, we could approximate the increase in the liquid level as a constant rate of $0.38\,\mathrm{mm/min}$. This implied LAr would reach the level of the mesh at the time marked "Mesh" in Fig 7.1. We also expected a drastic change in the magnitude of the electric field near the liquid-gas phase boundary when the liquid level crossed over the mesh. This change would be reflected in a sharp decrease in the S2 pulse rise time. We observed this transition at the time marked with "Normal S2". The discrepancy between "Mesh" and "Normal S2" gave us a measure of the systematic uncertainty in our liquid level measurement. During the October run, we filled the TPC to the "Normal S2" level by monitoring the S2 pulse rise time. We took the average of the two calibration methods and reported the liquid level as $1\,\mathrm{mm}$ above the mesh, with an error of $\pm\,1\,\mathrm{mm}$.

During the initial LAr filling at the beginning of each TPC commissioning, two additional PT1000 RTDs located at intermediate heights below the TPC helped to indicate the progress of the fill. The readings on those RTDs, the temperature readings on the Lake Shore controller, the pressure transducer measurement and the mass flow controller reading were fed into a USB-1208LS Multifunction USB Data Acquisition Device by Measurement Computing Corporation [84]. Those digitized measurements and the capacitance readings from the UTI were recorded on a slow control computer with a National Instrument LabVIEW [85] program[1]

7.2 Single photoelectron calibration

The single PE response (SER) of each PMT, determined using pulses in the tails of scintillation events, was continuously monitored and showed a slow decline of about 15% (26%) in

---

[1]The program was the product of a joint effort by Thomas Alexander and the author.
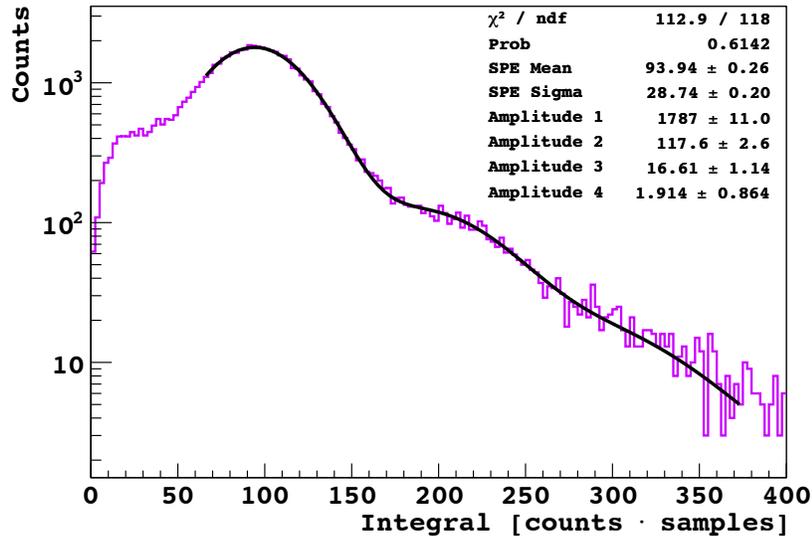
Figure 7.2: The charge response spectrum of the top PMT over Run 611. The spectrum is fit with a sum of four Gaussian functions with related means and sigmas (see text). The normalization factors of the Gaussian functions are free parameters. We used the mean of the first Gaussian function as the SPE mean calibration and the sigma of the first Gaussian function as the sigma calibration of the SPE distribution.

the top PMT and 10% (26%) in the bottom PMT over the course of the 6 (13) day run in June (October).

We define the regions of the recorded waveforms containing an excursion from the baseline above a threshold of $\sim$4 times the rms of baseline noise as the signal regions. We select signal regions that are shorter than 150 ns (including a 40 ns pre-signal baseline and a 40 ns post-signal baseline) on each PMT, and compute the integral in units of digitizer counts·samples. We fit the distribution of the integral for each PMT to a sum of four Gaussian functions:

$$f(x, \mu, \sigma^2, c_1, c_2, c_3, c_4) = c_1 \cdot \mathrm{Gaus}(x, \mu, \sigma^2) + c_2 \cdot \mathrm{Gaus}(x, 2\mu, 2\sigma^2)$$
$$+ c_3 \cdot \mathrm{Gaus}(x, 3\mu, 3\sigma^2) + c_4 \cdot \mathrm{Gaus}(x, 4\mu, 4\sigma^2), \tag{7.1}$$

where $\mathrm{Gaus}(x, \mu, \sigma^2) = \exp[-(x - \mu)^2/(2\sigma^2)]$. Two fit function calls were issued. The first iteration searched for good estimates of μ, σ and the normalization constants c_1 to c_4 for use as starting values for the second iteration. In the second iteration, the fit region was fixed
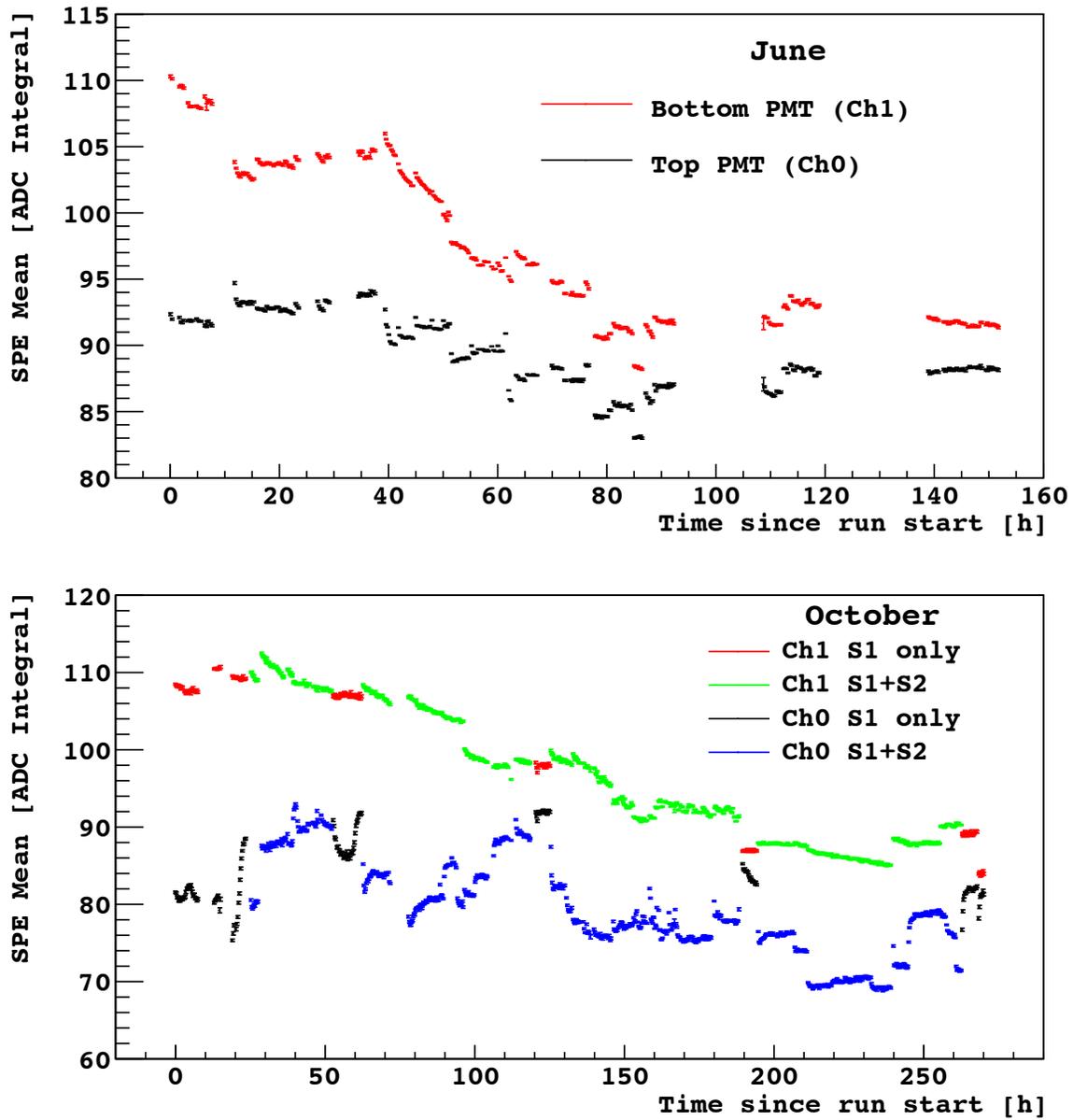
Figure 7.3: SPE mean calibration for the June and October runs. Each data point is the fit result on a 15-minute block of data. The data sets from the October run are divided into those with only S1 signals and those with both S1 and S2 signals.

to $(\mu_1\text{-}\sigma_1, 4\mu_1)$, where μ_1 and σ_1 are the best fit values in the first iteration. The results obtained with applying this procedure to all data sets from the June and October runs are shown in Fig. 7.3 and 7.4.
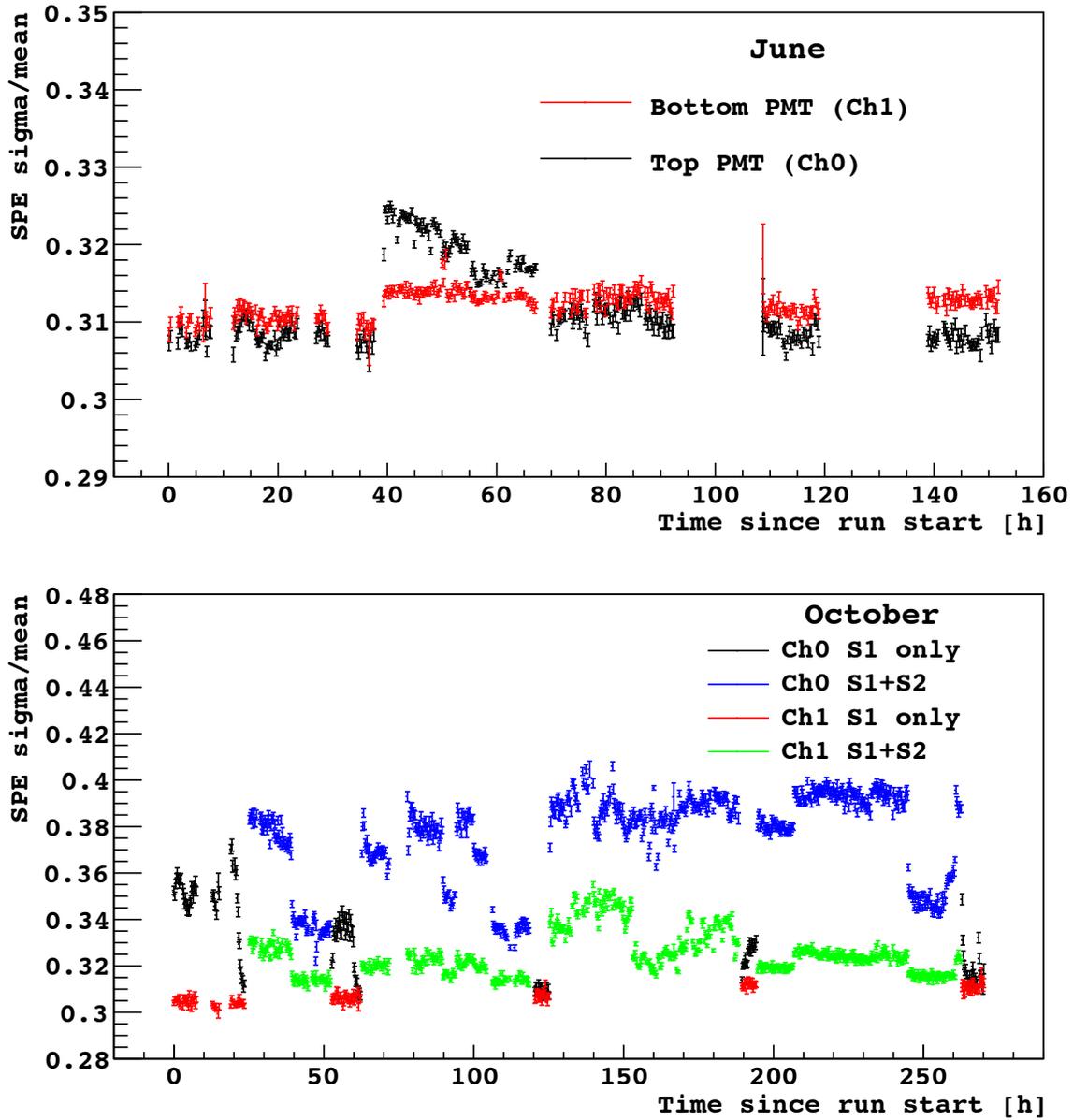
Figure 7.4: SPE sigma/mean calibration for the June and October runs. Each data point is the fit result on a 15-minute block of data. The data sets from the October run are divided into those with only S1 signals and those with both S1 and S2 signals.

7.3   LED calibration

During the October run, we injected light pulses of 355 nm and ∼1 ns width from an Ocean Optics LED [86] at a rate of 1 Hz through an optical fiber into the TPC, and recorded the corresponding data by forcing the simultaneous trigger of the data acquisition system. As
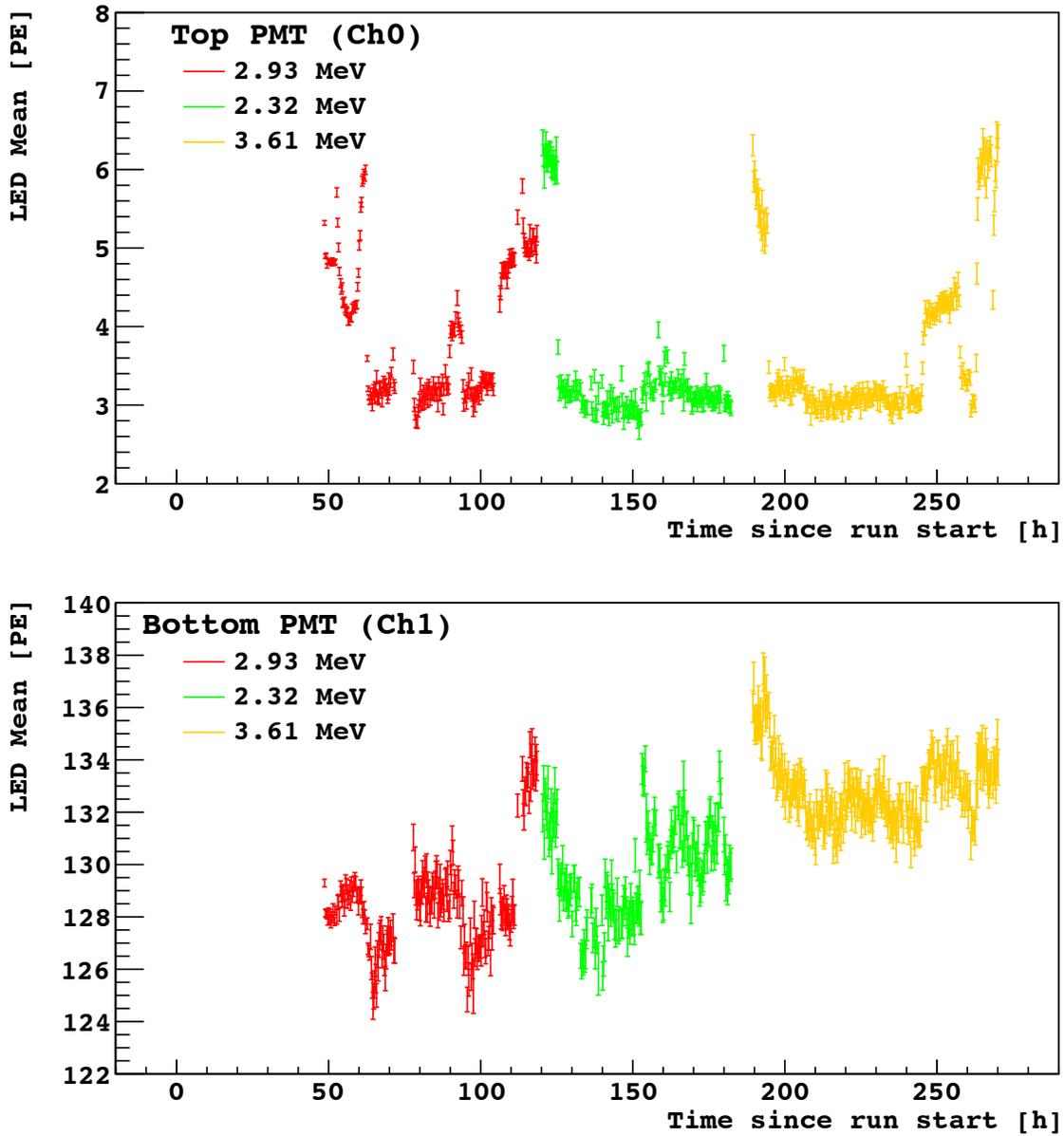
Figure 7.5: The mean of LED pulses observed by the TPC PMTs. Each data point corresponds to the statistics of a 15-minute block of data. The data are divided into three periods according to the proton beam kinetic energies as labeled. An hardware issue caused the data from the beginning 45 hours incompatible with the remaining set of data. This portion of data is omitted from the plots.

shown in the bottom plot of Fig. 7.5, the mean pulse integral in PE on the bottom PMT

drifted in a range of ±4% over the entire run (assuming perfect stability of the LED system).
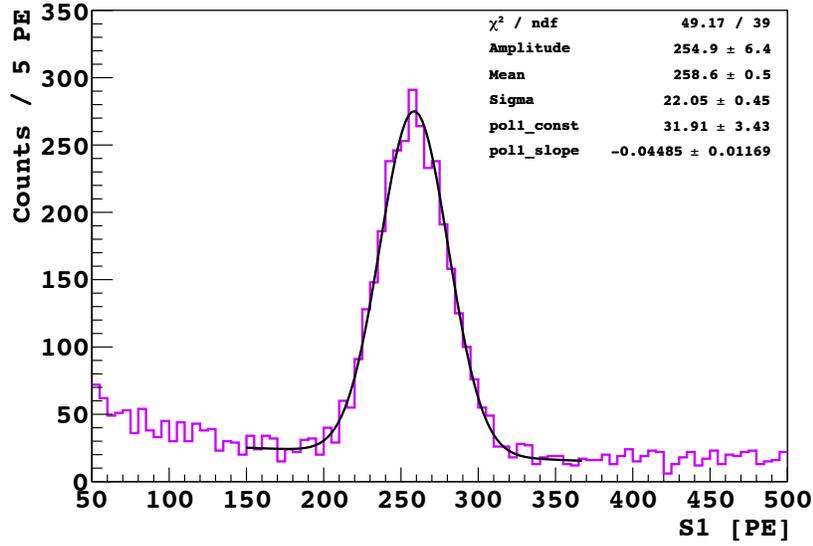
Figure 7.6: Example of S1 light yield calibration with ^{83m}Kr source. The S1 spectrum is extracted from Run 557. The ^{83m}Kr peak region is fit with a Gaussian plus a first order polynomial. The mean of the Gaussian function and its error is taken as the input for Fig. 7.7.

We did not observe any change in the mean pulse integral immediately following the changes to the cathode voltage i.e. the drift field.

The mean response of the top PMT to LED pulses (normalized to the SER) reversibly decreased by about a factor of $\sim$2 whenever ionization signals were turned on (see the top plot of Fig. 7.5). We believe this represents a reduction in quantum efficiency at the high light levels produced in the top PMT by the S2 signals. Manufacturer's data shows a reduction in the maximum allowable cathode current density at reduced temperature [87]. The reduction also depended on the drift field. Higher drift field reduced the electron-ion recombination in LAr, which increased the amplitude of S2 signals. To correct for this variation in response, we divided the data into 15-minute blocks and within each block, normalized the top PMT signals to the LED response.
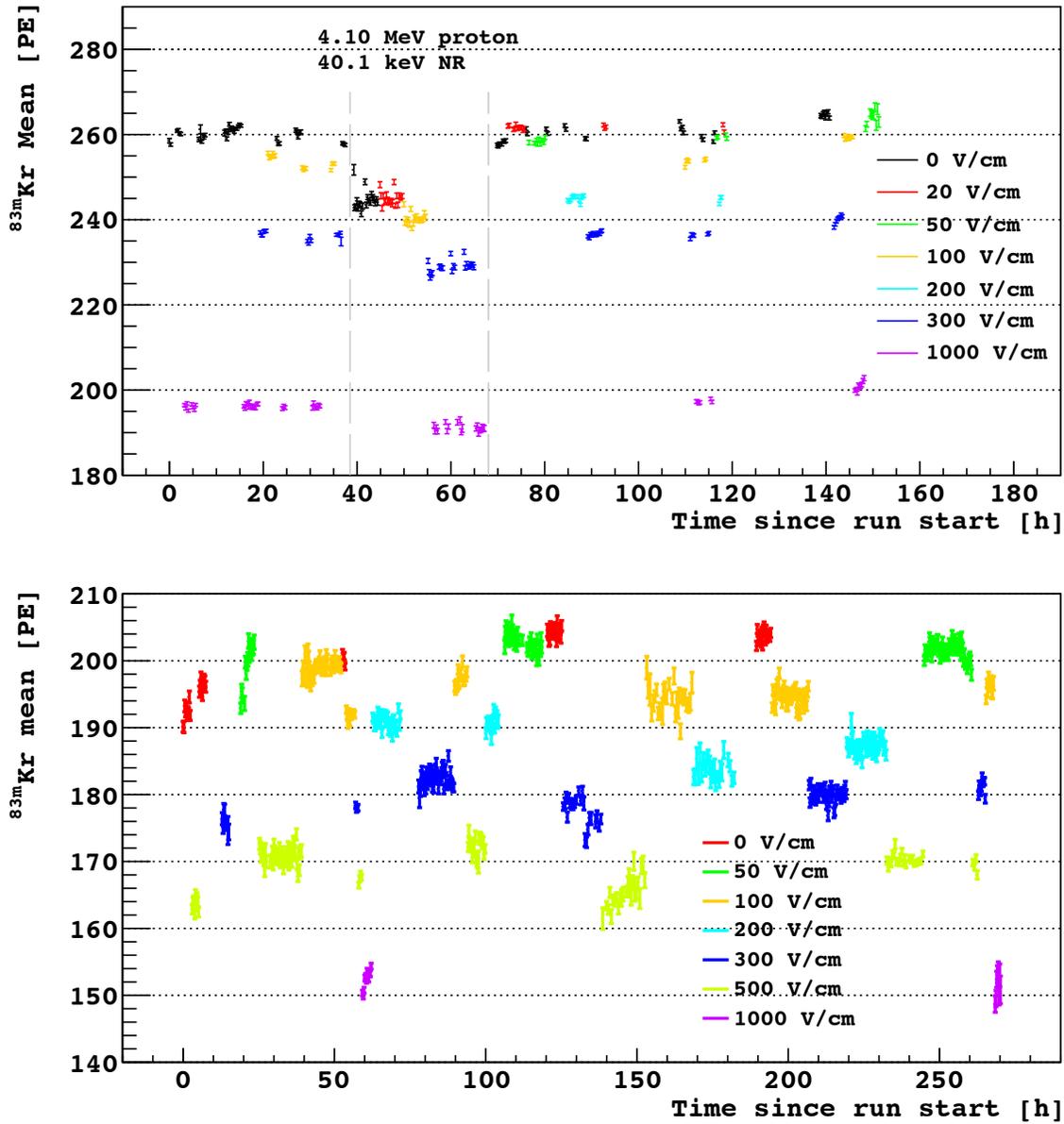
Figure 7.7: ^{83m}Kr S1 light yield calibration for the June (top) and October (bottom) runs. Each data point is the fit result on a 15-minute block of data. During the June run, when a proton beam energy of 4.10 MeV was selected, the light yield of the TPC dropped by 6%. This drop was likely due to a decrease in the PMT photon detection efficiency as a result of the higher γ-ray rate produced by the beam.

7.4   S1 light yield calibration

To monitor the scintillation yield from the LAr, ^{83m}Kr was continuously injected by including a ^{83}Rb trap [88–90] in the recirculation loop (see Fig. 6.7). ^{83m}Kr has a half life of 1.83 hours

and decays via two sequential electromagnetic transitions with energies of 9.4 and 32.1 keV and a mean separation of 223 ns [91]. Because scintillation signals in LAr last for several microseconds [92], the two decays are detected in a single scintillation pulse. The activity of ^{83m}Kr in the TPC was 1.2 kBq (reduced to 0.5 kBq in the October run).

The stability of the entire system was assessed throughout the data taking by monitoring the ^{83m}Kr peak position (see Fig 7.6 and 7.7). At zero field, the position of the ^{83m}Kr peak was measured to be 260 (200) PE in June (October) and varied by less than $\pm 4\%$ ($\pm 4\%$) over the entire run. The reduction in light yield in October was a result of operating the TPC with the liquid level above the grid (to allow S2 collection). The short term stability within a data set was checked with ^{83m}Kr spectra accumulated every 15 minutes; these show negligible variations over several hours.

Our data included a population of prompt events characterized by narrow pulses in the TPC PMT's with timing slightly earlier than photon-induced scintillation events (see Fig. 8.1 (a)), and data taken with no liquid in the TPC contained a similar collection of events. The light from those events was typically concentrated in either one of the PMT's. We interpreted these signals as Cerenkov radiation from fast electrons passing through the fused silica windows, and therefore independent of scintillation processes in the argon. We used them to monitor for any dependence of the apparatus response on the drift field. The spectrum of these events showed a peak at ~ 80 PE in June which was stable within $\pm 2.5\%$ over all the electric field settings.

7.5 Position dependence of S1 light yield along the vertical axis

The geometry of TPCs normally cause the partition of photons on the top and bottom PMTs to depend on the scintillation event's position along the vertical (or z) axis. This creates a detector-specific S1 light yield dependence along the z-axis. This dependence can
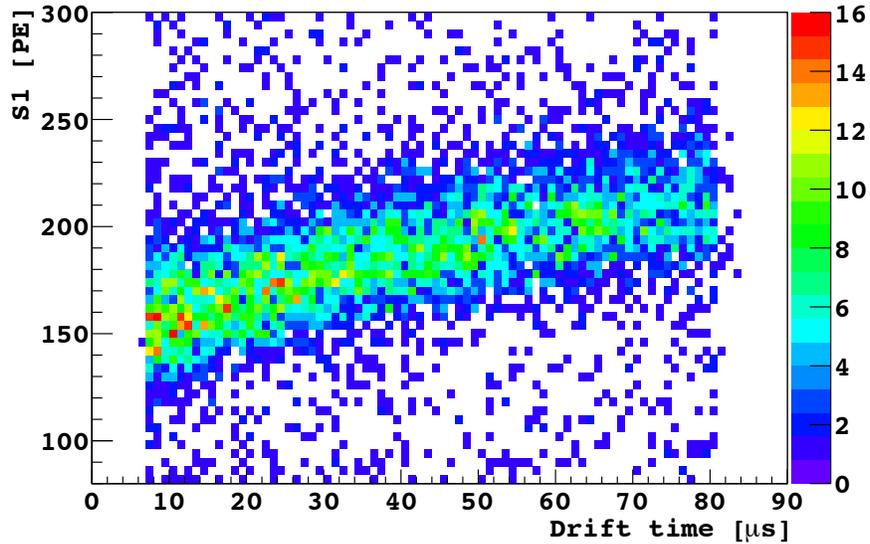
Figure 7.8: 2D distribution of S1 vs. drift time for the events with S1 in the ^{83m}Kr window. Data are extracted from Run 1197, where the drift electric field is 200 V/cm.

be calibrated quite precisely in TPCs with a localized mono-energetic source such as ^{83m}Kr, since the electron drift time (the difference between the start time of S1 and S2) determines the z-position of each event. This calibration can be applied to other data sets to improve the energy resolution of the TPC.

Due to the presence of the mesh and the gas phase, there is an asymmetry to the light collection of the dual phase TPC design. For all events except those located much closer to the top PMTs, the bottom PMTs typically receive a larger fraction of the S1 photons due to the imperfect transparency of the mesh and the reflection at the phase boundaries. In the SCENE TPC, a strong asymmetry was observed, possibly as a result of both the dual phase design and a lower photon detection efficiency on the top PMT (which exhibited efficiency decline during data sets with S2s) than the bottom PMT.

For the data sets where S2 was measured simultaneously with S1, we calibrated this position dependence with the ^{83m}Kr events. An example of the distribution of S1 pulse integral versus drift time in the TPC is shown in Fig. 7.8. The events included in this measurement contain a second pulse of light that starts at least 7 μs after the first pulse,
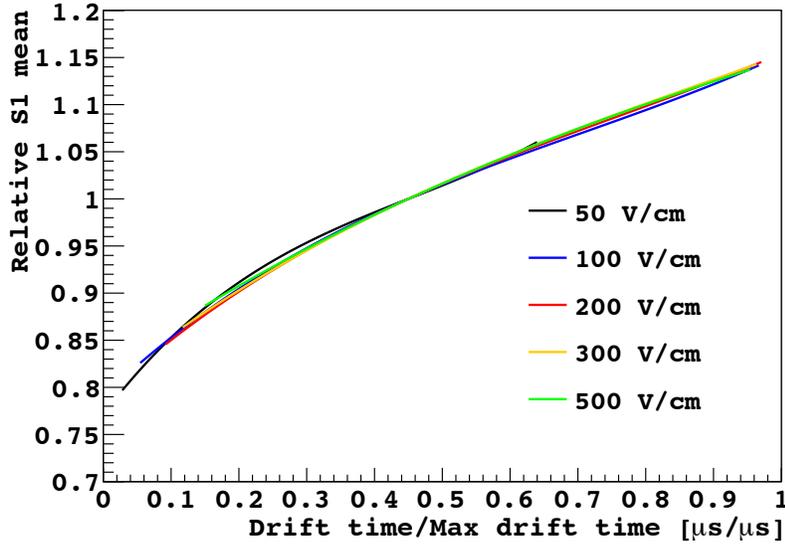
Figure 7.9: Mean ^{83m}Kr S1 light yield dependence on drift time for the October run (see text). The y-values are normalized to the mean ^{83m}Kr S1 yield at $(0.45 \times$ maximum drift time) for all the drift fields studied.

and its pulse shape is different from an S1 pulse - this is determined by whether the pulse shape parameter $\mathtt{f}_{90}$ is less than 0.1 (see the definition of $\mathtt{f}_{90}$ in Sec. 8.1).

For each y-slice of the 2D histogram in Fig. 7.8, we fit the distribution of S1 with a Gaussian function plus a first order polynomial. The fit mean of the Gaussian function is considered the mean ^{83m}Kr S1 yield for this drift time bin, which corresponds to a slice of LAr volume with the same z-position. We fit a third order polynomial, $p(t_{\mathrm{d}})$, to the ^{83m}Kr S1 mean as a function drift time, t_{d}. This procedure was applied to the data sets acquired under different drift fields. Fig. 7.9 shows the comparison among the polynomials for the full range of drift fields. Each curve is normalized by factoring out the ^{83m}Kr S1 yield field dependence and the electron-drift speed field dependence.

We divided the third order polynomial $p(t_{\mathrm{d}})$ by the ^{83m}Kr S1 yield measured in S1 only data sets (*i.e.*, no extraction field) for each drift field. This new polynomial $p_2(t_{\mathrm{d}})$ is used as the calibration for the S1 dependence on drift time for each drift field setting. To correct for the drift time dependence, the S1 for each event is divided by $p_2(t_{\mathrm{d}})$. The motivation for

63

dividing $p(t_\mathrm{d})$ by the ^{83m}Kr S1 yield measured in S1 only data sets is such that the corrected ^{83m}Kr S1 in the S1+S2 data sets has the same mean as in the S1 only data sets.

7.6 Electron-drift lifetime and S2 light yield calibrations

During the data sets where ionization was measured simultaneously with scintillation, we also tracked the electron-drift lifetime [25, 93] with ^{83m}Kr. This was done by measuring the correlation between S2 pulse integral and drift time in the TPC (see Fig. 7.10). The events included in this measurement contain a second pulse of light that starts at least $7\,\mu$s after the first pulse, and its pulse shape is different from an S1 pulse - this is determined by whether the pulse shape parameter $\mathtt{f}_{90}$ is less than 0.1 (see the definition of $\mathtt{f}_{90}$ in Sec. 8.1).

As shown in Fig. 7.11, the electron-drift lifetime was greater than $40\,\mu$s for the entire October run and we improved it by recirculating argon gas through the getter over the course of the data taking, where it reached $120\,\mu$s at the end of the run. Maximum drift time in the TPC ranged from $300\,\mu$s (drift field $50\,$V/cm) to $46\,\mu$s ($500\,$V/cm), as electron drift velocity increases with drift field [94]. The S2 signals were corrected for attachment of the drifting electrons using the measured electron-drift lifetime.
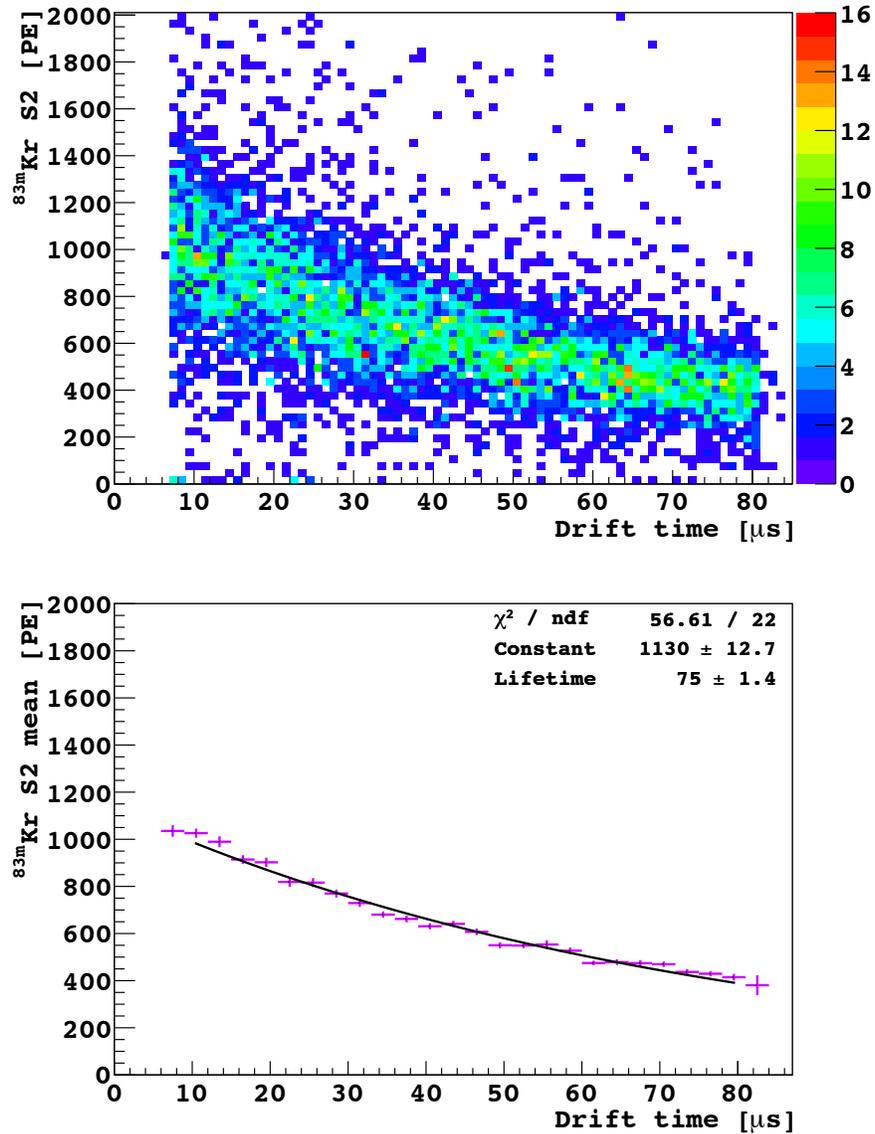
Figure 7.10: **Top:** 2D distribution of S2 vs. drift time for the events with S1 in the ^{83m}Kr window. Data are extracted from Run 1197, where the drift electric field is 200 V/cm. **Bottom:** The S2 mean of 3 μs-wide bins vs. drift time for the same data set on the top plot. The data points are fit to an exponential decay function. The "lifetime" parameter is the input for the top plot of Fig. 7.11 and the "constant" parameter is the input for the bottom plot of Fig. 7.11.
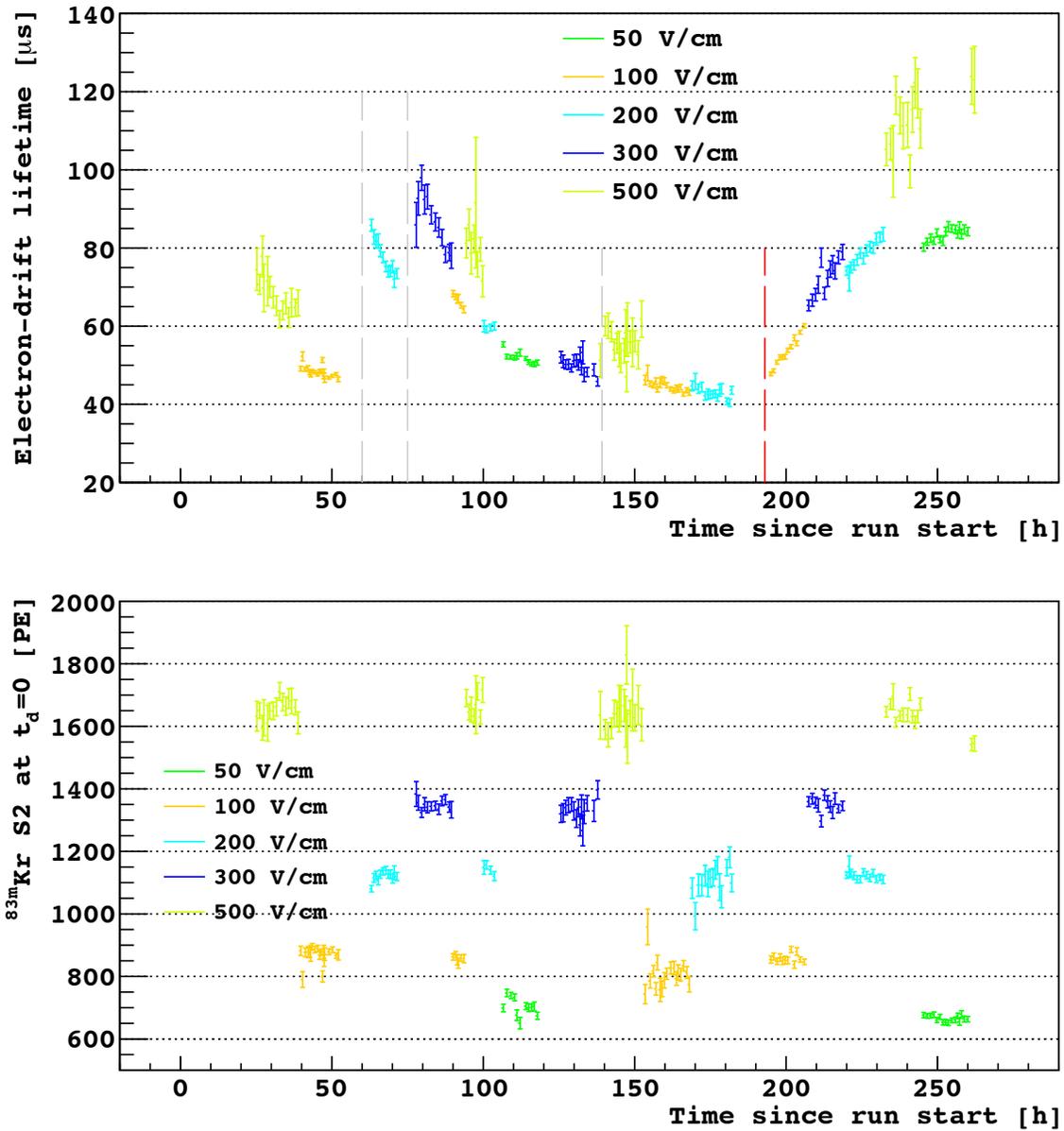
Figure 7.11: Electron-drift lifetime and S2 light yield calibration with ^{83m}Kr source for the October run. **Top:** Electron-drift lifetime as a function of time. The recirculation flow rate *during the S2 data taking* was kept at 1 slpm before the red dashed line, and the flow rate after it was increased to 3 slpm. The gaps marked by gray dashed lines between data points were the periods of S1 data taking when we raised the recirculation flow rate to 6 or 7 slpm. **Bottom:** The S2 mean of ^{83m}Kr after applying the electron-drift lifetime correction - this corrected mean is equal to the S2 mean if the exponential fit is extrapolated to 0 drift time.

Chapter 8

Analysis and results

In this chapter, I present the detailed set of results on the S1 and S2 measurements. I also report the first observation in LAr of an anti-correlation between scintillation and ionization from neutron-induced nuclear recoils; this closely resembles the anti-correlation between scintillation and ionization from electrons [95], relativistic heavy ions [96], α particles and fission fragments [97]. With the aid of a model describing the relationship between the number of ion pairs (N_i) and the magnitude of S2, we extracted the numbers of excitons (N_{ex}) and ion pairs (N_i) and their ratio (N_{ex}/N_i) produced by nuclear recoils from 16.9 to 57.2 keV. Finally, I report a preliminary comparison of the S1 and S2 yields for recoils parallel and perpendicular to the applied field.

8.1   Event selection

We focus on the case of events taken in a specific configuration - 57.2 keV nuclear recoils with a 200 V/cm drift field, a 3.0 kV/cm extraction field, and a 4.5 kV/cm multiplication field - to illustrate the criteria for event selection that were applied to the analysis of the entire set of data. Fig. 8.1 shows, for this data set, the relevant distributions in pulse shape discrimination parameters and time-of-flight. The distributions were similar under other drift fields and recoil energies.
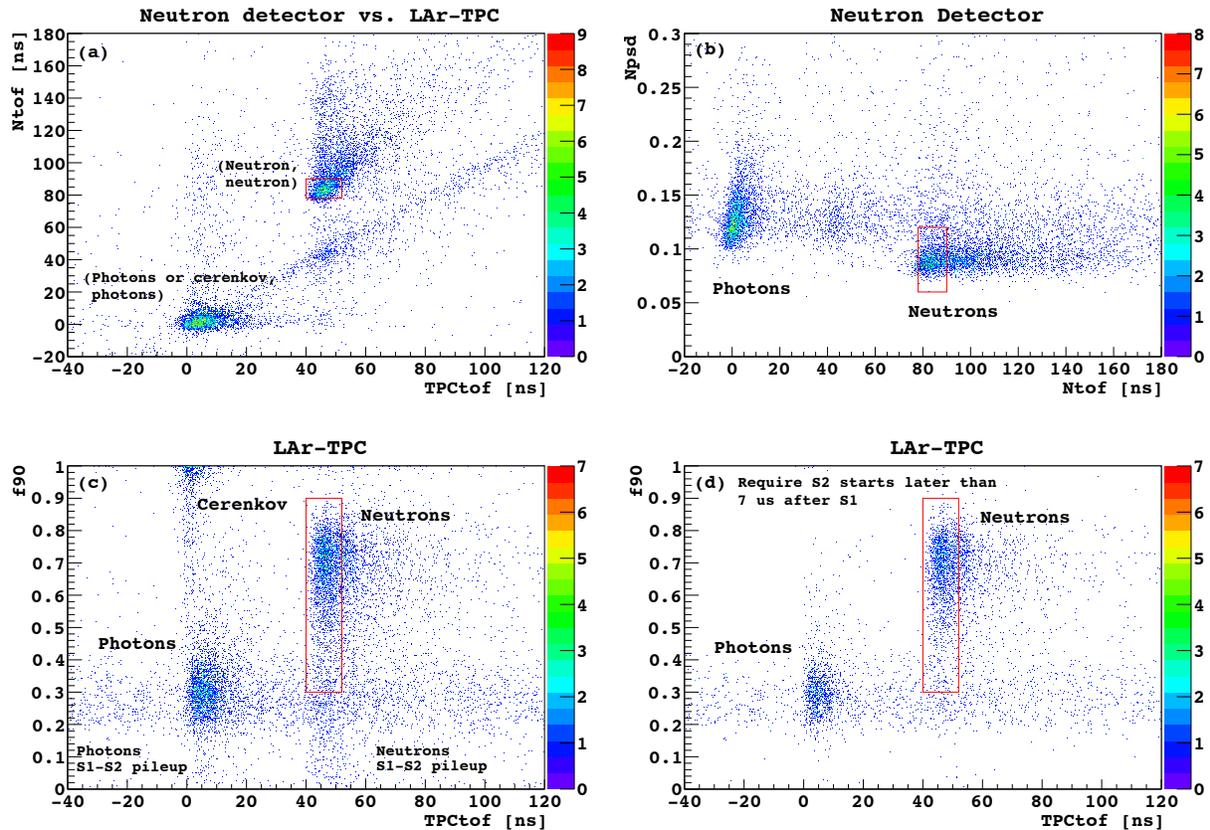
Figure 8.1: Distributions of time of flight vs. time of flight and pulse shape discrimination vs. time of flight for data taken in the 57.2 keV configuration described in the text. See the text for the definition of the variables. The red boxes define the acceptance regions for TOF and PSD parameters in the TPC and neutron detector. Panel (a) shows the time of flight to one neutron detector vs. the time of flight to the TPC. Panel (b) describes the neutron detector response and Panels (c) and (d) the TPC response. In panel (c), the clusters of events with $f_{90} < 0.1$ have S2 signals that start before the termination of S1 signals. Panel (d) shows the distribution of events selected with the requirement that S1 and S2 signals are properly resolved.

Fig. 8.1c shows a scatterplot of the discrimination parameter f_{90} [98], defined as the fraction of light detected in the first 90 ns of the S1 signal, vs. the time difference between the proton-beam-on-target and the TPC signal (TPCtof). Times of arrival for the TPC pulses - the output of the TimeOfFlight module - were determined by interpolating the waveform of each pulse to a threshold of 50% peak amplitude. On the other hand, the accelerator buncher provides a periodic waveform with the period equal to the time separation between proton pulses. Also in the TimeOfFlight module, we use an arbitrary fixed threshold (around

68

where the periodic waveform has the maximum slope) on the buncher waveform to obtain the proton-beam-on-target time with an offset. This offset can be determined approximately with the arrival time of γ-rays or neutron events, since the time of flight is well defined by the speeds of light and of neutrons. The determination of this offset is completely optional as it affects the arrival times of all TPC and neutron detector signals equally. With the offset subtracted, beam-associated events with γ-like and neutron-like $\mathtt{f}_{90}$ are clustered near 5 and 45 ns respectively, as expected given the approximate 1.8 cm/ns speed for 1.773 MeV neutrons. Cerenkov events are characterized by $\mathtt{f}_{90}$ close to 1.0 and γ-like timing. The ^{83m}Kr events appear with β/γ-like $\mathtt{f}_{90}$, and are uniformly distributed in the TPCtof variable as expected. For the events with vertices located a short distance from the grid, S1 and S2 arrived too close in time to be resolved, resulting in a smaller than usual $\mathtt{f}_{90}$ (S1-S2 pileup). These events were removed by requiring each event to contain a second pulse that started at least 7 μs after the first, with the second pulse's $\mathtt{f}_{90}$ less than 0.1. Fig. 8.1d shows the same scatterplot after removal of these events.

Fig. 8.1b shows a scatterplot of the neutron pulse shape discriminant (Npsd), defined as peak amplitude divided by area in the neutron detectors, vs. the time difference between the proton-beam-on-target and the neutron detector signal (Ntof). The signal time in the neutron detector is determined with the same method used in the TPC. Neutron events cluster near a Npsd of 0.09 and a Ntof of 85 ns, while β/γ events cluster near a Npsd of 0.13 and a Ntof of 2 ns. Random coincidences from environmental backgrounds are visible at intermediate times. Fig. 8.1a shows a scatterplot of Ntof vs. TPCtof.

Fig. 8.2 shows, for the same data set, the impact of the cuts based on the pulse shape discrimination parameters and time-of-flight distributions. Again, the results of this selection

| 78 < Ntof (ns) < 90 | 0.06 < Npsd < 0.12 |
| 40 < TPCtof (ns) < 52 | 0.3 < $\mathtt{f}_{90}$ < 0.9 |

Table 8.1: The cuts applied for the 57.2 keV nuclear recoil data sets.
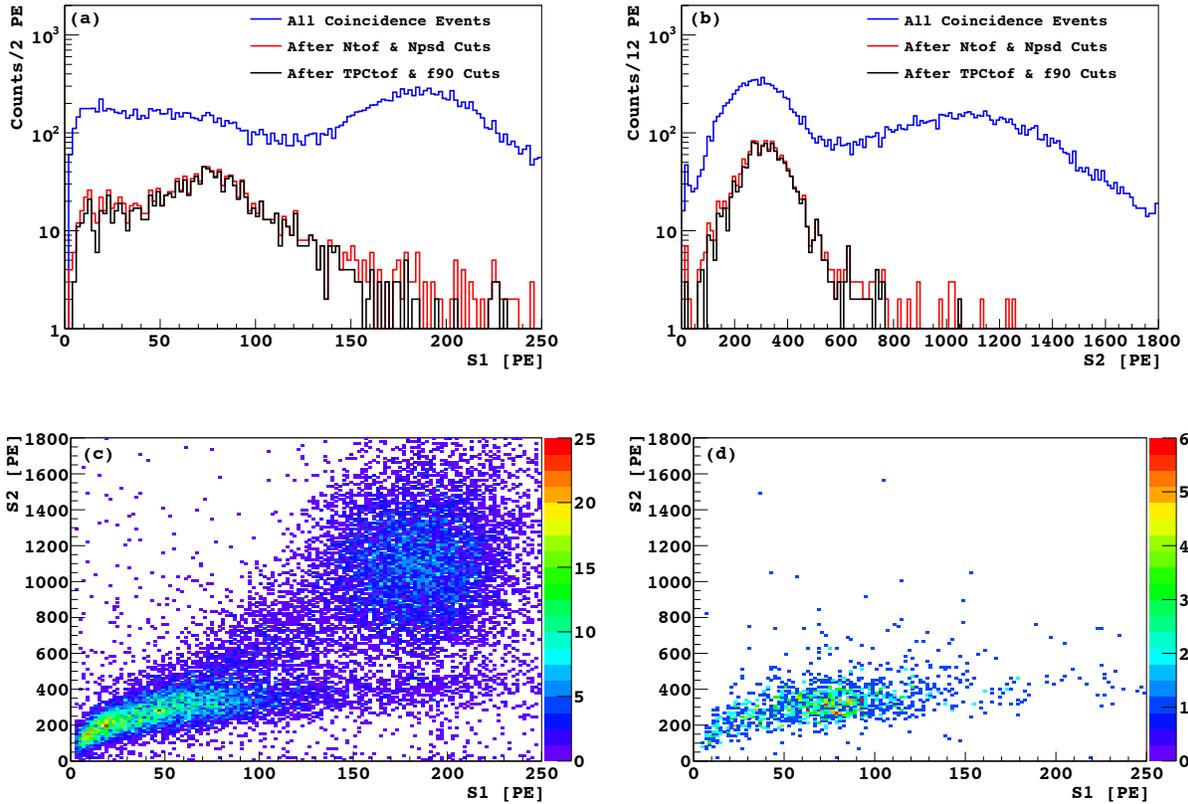
Figure 8.2: (a) Surviving primary scintillation light (S1) distributions for 57.2 keV nuclear recoils as the neutron selection cuts described in the text were imposed sequentially. Data were collected with a drift field of 200 V/cm and an extraction field of 3 kV/cm. The high energy peak around 187 PE is due to the ^{83m}Kr source used for continuous monitoring of the detector. (b) Surviving distributions of electroluminescence light from ionization (S2) for 57.2 keV nuclear recoils after the same cuts. (c) S2 vs. S1 distribution for all events with resolved/non-overlapping S1 and S2 before the neutron selection cuts. (d) S2 vs. S1 distribution for the events surviving the neutron selection cuts.

were similar for all data sets within this experiment. We selected nuclear recoil events with Ntof and TPCtof within ±6 ns of the peak from neutrons. For pulse shape we imposed the requirements of $0.06 <$ Npsd < 0.12, and $0.3 <$ f$_{90} < 0.9$. The TOF and PSD cuts for the 57.2 keV data sets are also shown in Fig 8.1 and listed in Table 8.1. Fig. 8.2a shows the S1 spectra as cuts based on the pulse shape discrimination parameters and time-of-flight distributions are imposed in sequence. The high energy peak around 187 PE is the signal from the ^{83m}Kr source used for continuous monitoring of the detector. Similarly, Fig. 8.2b
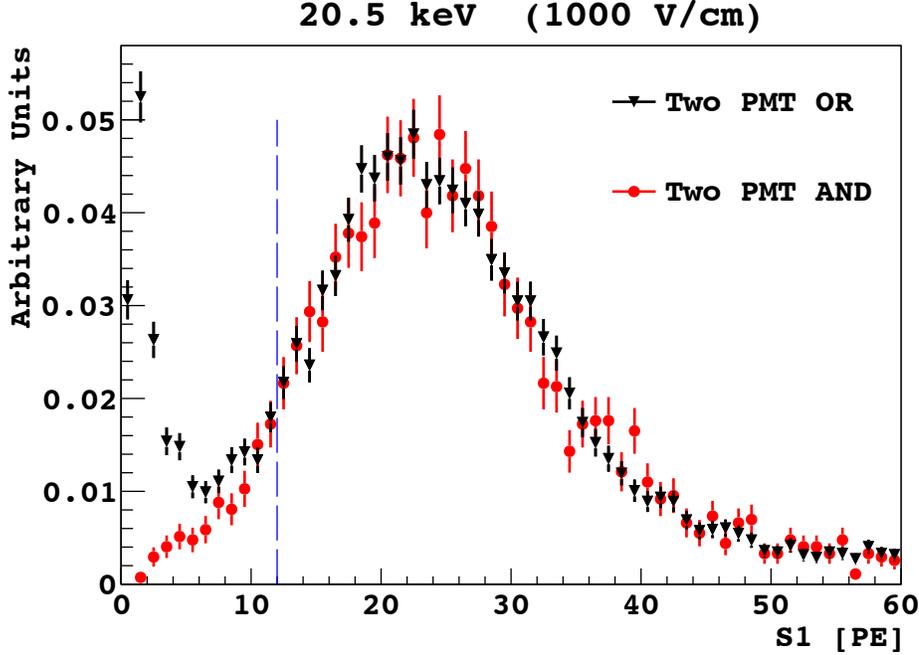
Figure 8.3: Comparison of recoil S1 spectra taken with the TPC PMT's OR (**black**) and AND (**red**) trigger. The integral between 12 and 60 PE for each spectrum is normalized to 1. Use of coincidence trigger had no significant effect on the spectral shape above ~12 PE.

shows the S2 spectra as the same cuts are imposed. The S2 peak from the ^{83m}Kr source is located near 1100 PE. Fig. 8.2c and 8.2d provide a comparison of the S2 vs. S1 distribution before and after the neutron selection cuts. The outstanding signal to background ratio that emerges as the cuts are applied in sequence shows the power of this technique.

8.2 Impact of trigger efficiency on S1 spectra

To assess possible distortions of the S1 spectra due to the trigger efficiency introduced by the AND trigger described earlier, we analyzed two subsets of 20.5 keV nuclear recoils data taken with the two different TPC triggers. As shown in Fig. 8.3, the spectrum distortion induced by the choice of trigger is significant only below 10 PE. This is in good agreement with the independent measurement of the trigger efficiency performed with the ^{22}Na source (see Fig. 6.10). We conclude that all spectra collected with the trigger condition requiring the AND of the TPC PMT's produced undistorted spectra above 12 PE and could be used

reliably, while helping reduce the amount of data written to disk by efficiently rejecting the rising background below 5 PE.

8.3 Analysis of the S1 spectra and determination of $\mathcal{L}_{\text{eff}, \, 83\text{m}\text{Kr}}$

We define $\mathcal{L}_{\text{eff}, \, 83\text{m}\text{Kr}}$ as the scintillation efficiency of nuclear recoils relative to that of electron recoils from ^{83m}Kr at zero field:

$$\mathcal{L}_{\text{eff}, \, 83\text{m}\text{Kr}} \left(E_{\text{nr}}, \, \mathcal{E}_{\text{d}} \right) = \frac{S1_{\text{nr}} \left(E_{\text{nr}}, \, \mathcal{E}_{\text{d}} \right) / E_{\text{nr}}}{S1_{\text{Kr}} \left(\mathcal{E}_{\text{d}} = 0 \right) / E_{\text{Kr}}}, \tag{8.1}$$

where E_{Kr} is 41.5 keV, E_{nr} is the recoil energy and $\mathcal{E}_{\text{d}}$ is the drift electric field. The measurement of $\mathcal{L}_{\text{eff}, \, 83\text{m}\text{Kr}}$ in this experiment permits the unbiased and straightforward computation of nuclear recoil scintillation yield from the measured light yield of ^{83m}Kr in any liquid argon scintillation detector. The first results of our experiment [29] demonstrated that $\mathcal{L}_{\text{eff}, \, 83\text{m}\text{Kr}}$ depends not only on E_{nr} but also on $\mathcal{E}_{\text{d}}$.

With the experiment described here we have obtained a precise determination of $\mathcal{L}_{\text{eff}, \, 83\text{m}\text{Kr}}$ in LAr. The crucial step in the analysis of our data was the determination of the overall S1 yield, $S1_{\text{nr}}$, as a function of E_{nr} and $\mathcal{E}_{\text{d}}$.

This was accomplished by fitting the data for each recoil angle setting (with PE as the ordinate) to Monte Carlo energy deposition spectra (with keV as the ordinate), using a single scale factor for each experimental geometry. The ordinates for the data were computed based on a light yield 6.3±0.3 (4.8±0.2) PE/keV measured in June (October) using ^{83m}Kr.

The simulations computed the energy deposition in the LAr, taking into account the complete kinematics and geometry of the LAr-TPC and the coincidence detectors, as well the TOF analysis cuts. Before fitting, the MC distribution was convolved with a Gaussian energy resolution function with σ_1 parametrized as $\sigma_1 = \sqrt{S1_{\text{nr}}} \, R_1(E_{\text{nr}}, \mathcal{E}_{\text{d}})$, where R_1 is a
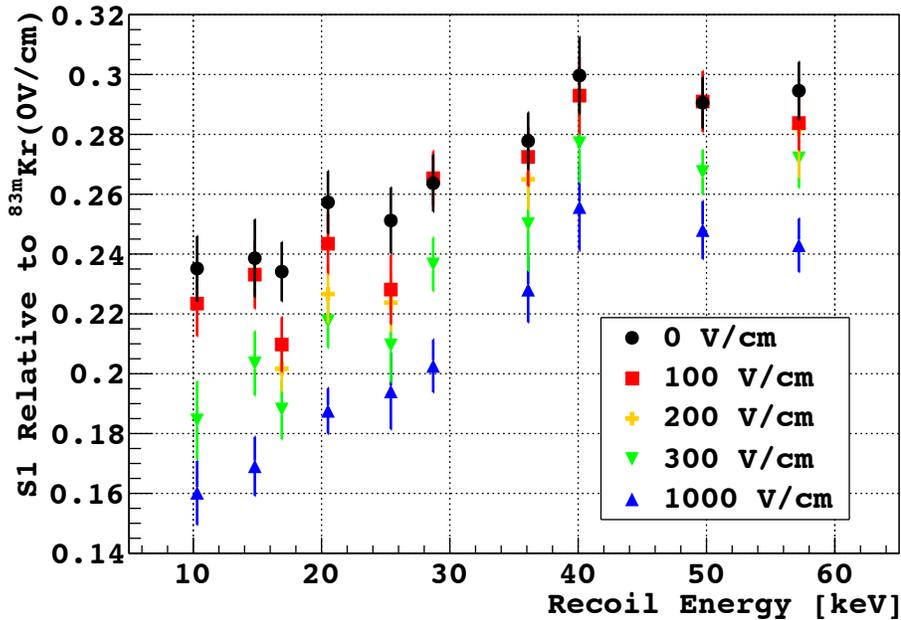
Figure 8.4: S1 yield as a function of nuclear recoil energy measured at 5 drift fields (0, 100, 200, 300 and 1000 V/cm) relative to the light yield of ^{83m}Kr at zero field.

free parameter of the fit. The fit procedure varies $S1_{\mathrm{nr}}$ and R_1 to minimize the χ^2 defined as:

$$\chi^2(S1_{\mathrm{nr}},\, R_1) = \sum_{i=1}^{n} \frac{(O_i - S_i)^2}{S_i}, \tag{8.2}$$

where n is the total number of bins in the chosen fit region, O_i is the number of events observed in bin i, and S_i is the number of events in bin i resulting from simulations.

The fit results for all ten recoil energies measured - ranging from 10.3 to 57.2 keV - and all drift fields investigated - ranging from 0 to 1 kV/cm - are shown in Figs. B.1, B.2, B.3, B.4, B.5, B.6, B.7, B.8, B.9, and B.10. In each of the figures, the plot in the top left panel shows the simulated energy spectrum fit with a Gaussian plus a first order polynomial modeling the background (the plot for the 10.3 keV nuclear recoils is absent in Fig. B.1 since it is already shown in Fig. 6.6). All other panels show the experimental data at a given drift field fit with Monte Carlo data. Apart from the low S1 region, the agreement between the data and the MC prediction is remarkably good.

Recoil Energy [keV]	10.3	14.8	16.9	20.5	25.4	28.7	36.1	40.1	49.7	57.2
$\mathcal{L}_{\text{eff},^{83\text{m}}\text{Kr}}$	0.235	0.239	0.234	0.257	0.251	0.264	0.278	0.300	0.291	0.295
Statistical error	0.003	0.005	0.004	0.001	0.005	0.004	0.003	0.005	0.005	0.004
Systematic error source										
Fit method	0.001	0.000	0.004	0.004	0.002	0.001	0.003	0.003	0.001	0.002
Fit range	0.000	0.002	0.000	0.001	0.002	0.000	0.001	0.000	0.000	0.000
TPCtof cut	0.002	0.003	0.003	0.001	0.002	0.001	0.001	0.002	0.001	0.001
Ntof cut	0.004	0.002	0.001	0.001	0.002	0.004	0.001	0.002	0.003	0.001
f90 cut	0.004	0.004	0.003	0.001	0.000	0.001	0.000	0.001	0.000	0.000
$^{83\text{m}}$Kr light yield	0.005	0.005	0.005	0.005	0.005	0.005	0.006	0.006	0.006	0.006
Recoil energy										
TPC position	0.001	0.001	0.001	0.001	0.001	0.001	0.001	0.001	0.001	0.001
EJ301 position	0.007	0.010	0.005	0.008	0.008	0.005	0.006	0.009	0.003	0.006
Combined error total	0.011	0.013	0.010	0.010	0.011	0.009	0.010	0.013	0.009	0.010

Table 8.2: Summary of error contributions to individual $\mathcal{L}_{\text{eff},^{83\text{m}}\text{Kr}}$ measurements at $\mathcal{E}_{\text{d}} = 0$. Only minor variations in the magnitude of systematic errors were observed across the range of drift field explored. The combined error for each measurement is shown Fig. 8.4.

Fig. 8.4 shows the resulting values of $\mathcal{L}_{\text{eff},^{83\text{m}}\text{Kr}}$ as a function of E_{nr} as measured at 5 different drift fields (0, 100, 200, 300 and 1000 V/cm). The error bar associated with each $\mathcal{L}_{\text{eff},^{83\text{m}}\text{Kr}}$ measurement represents the quadrature combination of the statistical error returned from the fit and the systematic errors due to each of the sources accounted for. See Table 8.2 for a detailed account of systematic errors at null drift field and Table C.1, C.2, C.3, C.4, C.5 and C.6 for other drift fields.

In order to assess any bias introduced by our Monte Carlo model in the fit, we also fit each of the data sets with a Gaussian function plus a first order polynomial to account for background. The difference between the results of the two methods is listed in Table 8.2 in the row "Fit Method" for $\mathcal{E}_{\text{d}} = 0$. Across all measured recoil energies and drift electric fields, this systematic error is typically 1-2%, with the largest at 4%. The sensitivity of $\mathcal{L}_{\text{eff},^{83\text{m}}\text{Kr}}$ to the fit range selection is characterized by comparing the fit results to those obtained with a reduced fit range. We define the reduced range by raising the lower bound by 10% of the original fit range and lowering the upper bound by the same amount. The original fit ranges can be found in Figs. B.1 to B.10.
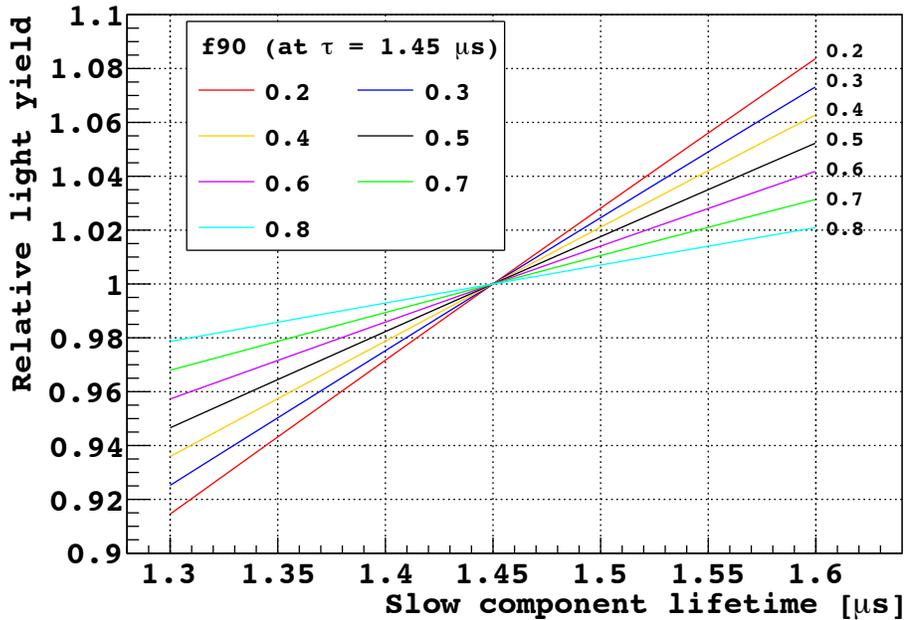
Figure 8.5: Systematic error induced by chemical impurities affecting the mean life of the triplet component of the S1 scintillation spectrum, as a function of mean life in the range of interest. S1 time profile was simulated with two exponential decay terms. Each line represents the events with a given f_{90} when the slow component lifetime is 1.45 μs. Note that f_{90} increases slightly with the decrease in the slow component lifetime.

We evaluated the systematic error in $\mathcal{L}_{\text{eff, }^{83m}\text{Kr}}$ from the TOF window selection by advancing or delaying the TPCtof cut by 3 ns while holding the Ntof cut constant, and vice versa, while keeping the same fit function described above and based on the Monte Carlo-generated spectra. We determined the associated systematic error as the average of the absolute difference in $\mathcal{L}_{\text{eff, }^{83m}\text{Kr}}$ obtained by either advancing or delaying the TOF window.

Within the dataset from a specific recoil energy and field setting, the LAr-TPC light yield determined with the ^{83m}Kr source fluctuated with a standard deviation of about 1%. In addition to such short term fluctuations, changes in the purity of the LAr result in variations of the light yield. The purity affects the mean life of the triplet state of the S1 scintillation time profile [99–101], which we measured to lie in the range from 1.39 to 1.48 μs. As shown in Fig. 8.5, this introduced an additional $\pm 2\%$ systematic uncertainty for ^{83m}Kr light yield, as its f_{90} is in the range of 0.2 to 0.3.

The uncertainty due to the alignment of the TPC and neutron detectors was calculated assuming a $\pm 1\,\mathrm{cm}$ uncertainty in our determination of their absolute positions relative to the beam stop.

8.4 Energy resolution

A number of factors, including the width of SER of the PMT's, the position dependence of light collection in the LAr TPC, PE counting statistics, and the intrinsic resolution of LAr scintillation, contributed to the energy resolution of the detector $\sigma_1 = \sqrt{S1_{\mathrm{nr}}} R_1(E_{\mathrm{nr}}, \mathcal{E}_{\mathrm{d}})$.

We assumed that the contribution from the spread in nuclear recoil energy due to the geometry of the detectors was fully accounted for by the Monte Carlo fit function. Our measurement of R_1 as a function of recoil energy and drift field showed a dependence of σ_1 upon $S1_{\mathrm{nr}}$ deviating from Poisson statistics. Results from the June and October 2013 runs are plotted separately in Fig. 8.6. The dependence of σ_1 on S1 is in both cases well described by:

$$\sigma_1^2 = \left(1 + a^2\right) S1 + b^2\, S1^2, \tag{8.3}$$

where a is the ratio of the measured width of the SER to its mean, and b is the combined effect of the intrinsic resolution of LAr and the dependence of the TPC light collection upon the position of the event. We fixed a to the measured value, $a = 0.3$, and extracted b from a fit of σ_1 versus S1.

Comparing the resolution fits for nuclear recoils vs. $^{83m}\mathrm{Kr}$, there is a substantial difference in the resolution fit parameters between the nuclear recoils and the β-like events. This could be attributed to the different contributions of recombination light for the two particle types.

The fitted value of the parameter b increased between the June and October runs. We believe this was related to the observed decrease in the resolution of the $^{83m}\mathrm{Kr}$ peak, also shown in Fig. 8.6. For the $^{83m}\mathrm{Kr}$ data, we calculated the resolution by a simple Gaussian
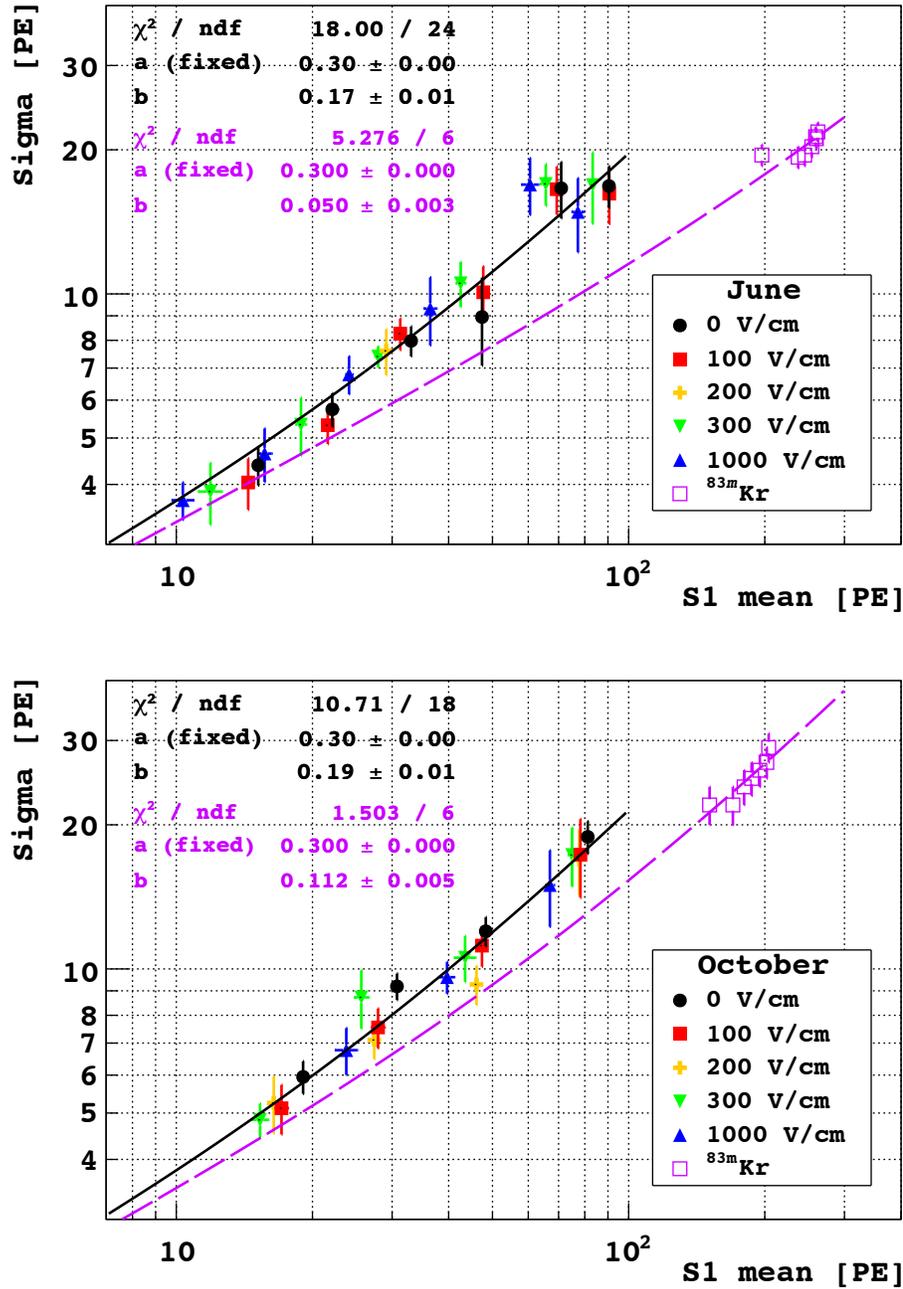
Figure 8.6: Energy resolution, σ_1, of the nuclear recoils extracted from the Monte Carlo fit, as a function of recoil energy for all drift field combinations. We separate the results from the June and October 2013 runs. The resolution for the nuclear recoils, σ_1, is fit (**black continuous curve**) with the function described in the text and compared with the fit obtained for the ^{83m}Kr (**purple dashed curve**) with the same function.

plus first order polynomial fit of the spectrum, then fit the data points with the same model described by Eq. 8.3.

We attribute the origin of the decrease in energy resolution for both nuclear recoils and ^{83m}Kr from the June to the October run to the change in the liquid level. The level was kept below the mesh during the June run and was raised $1\,\text{mm}$ above the mesh for the October run to ensure the proper production of S2 signals. The latter configuration was less favorable for light yield and resolution of the TPC as a number of scintillation photons undergoing internal reflection at the liquid-gas boundary passed multiple times through the mesh obstruction.

8.5   Distribution of $\mathtt{f}_{90}$ pulse shape parameter

We have used the S1 data from our experiment for a careful determination of the $\mathtt{f}_{90}$ parameter as a function of recoil energy. For this determination, we first selected events by applying the Ntof, Npsd and TPCtof cuts described above, then by requiring in addition that S1 lay in the range $[\mu - \sigma,\, \mu + \sigma]$, where μ and σ are the average value and the standard deviation of S1 as determined with the second fit method (Gaussian plus first order polynomial). This additional criterion further reduces the contribution of multiple-scatter events. As an example of this selection, Fig. 8.7(a) shows the 2D distribution of $\mathtt{f}_{90}$ vs. S1 for $20.5\,\text{keV}$ nuclear recoils at $\mathcal{E}_{\mathrm{d}} = 200\,\text{V/cm}$: in this case, the S1 selection range is the region bounded by the vertical dashed lines. The resulting $\mathtt{f}_{90}$ distribution is shown in Fig. 8.7(b). We define the nuclear recoil acceptances with the corresponding percentiles from this distribution.

Following this procedure, we determine the median $\mathtt{f}_{90}$ and the $\mathtt{f}_{90}$ acceptance curves for nuclear recoils as a function of recoil energy. The results are plotted in Fig. 8.8. Changes in the light yield of the TPC can affect the width of the $\mathtt{f}_{90}$ distribution but have little impact on the mean and the median. As the null field light yields of the October run was lower than the June run, the distributions for 16.9, 25.4, 36.1, and $57.2\,\text{keV}$, which were acquired in October (see Table 6.1), were expected to have larger widths than if they were acquired at the same light yield. The acceptance curves show only small variations with changes in drift
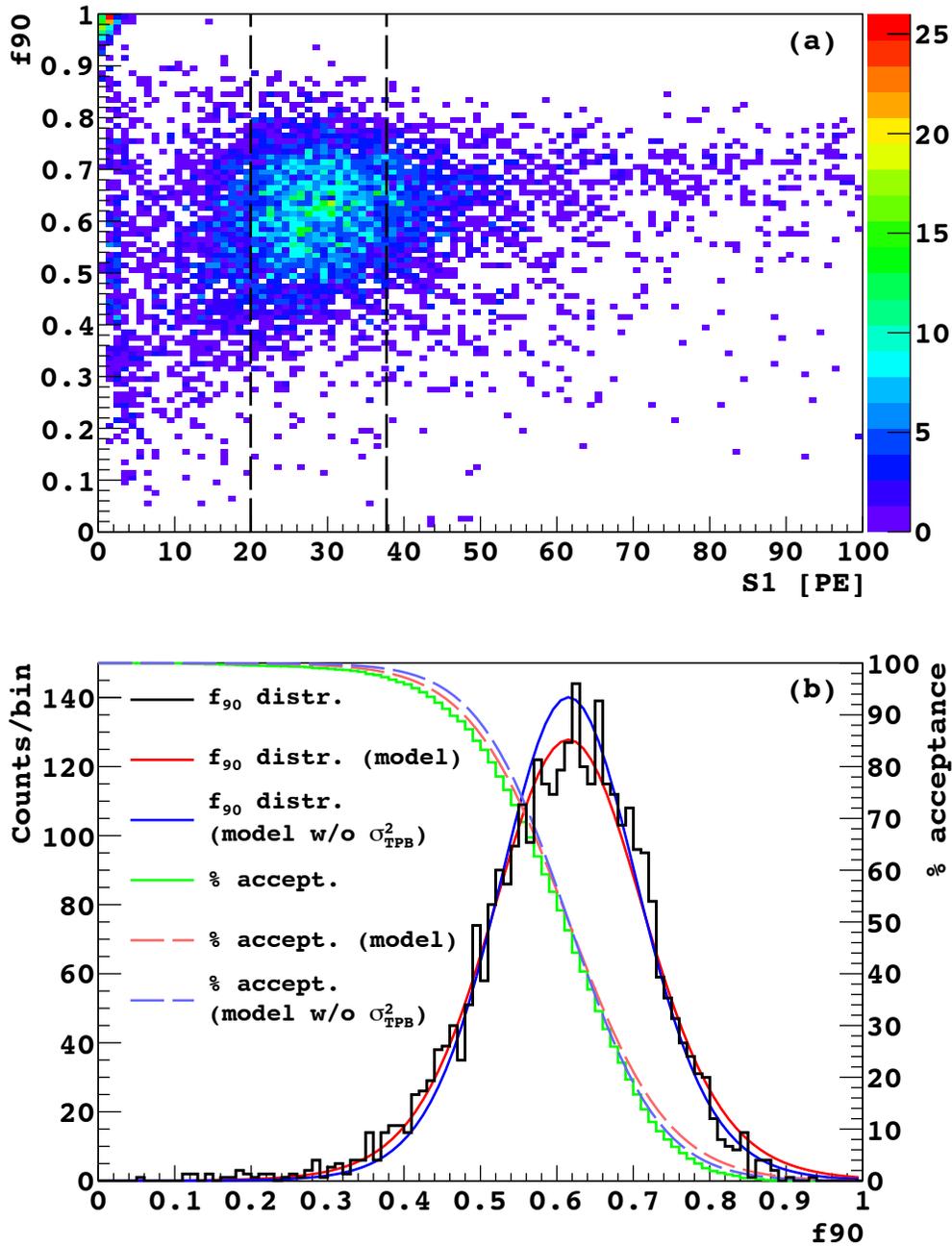
Figure 8.7: (a) Distribution of f_{90} vs. S1 for 20.5 keV recoil data taken at $\mathcal{E}_d = 200\,\text{V/cm}$. The vertical dashed lines indicate the boundaries of the region where S1 is within 1σ of the mean of the Gaussian fit μ, as described in the text. (b) **Black:** f_{90} distribution for the 20.5 keV nuclear recoil events with S1 falling in the region in $[\mu - \sigma, \mu + \sigma]$ *i.e.*, for the events fall in between the vertical dashed lines in panel (a). **Red:** f_{90} distribution model prediction (not a fit, see text).
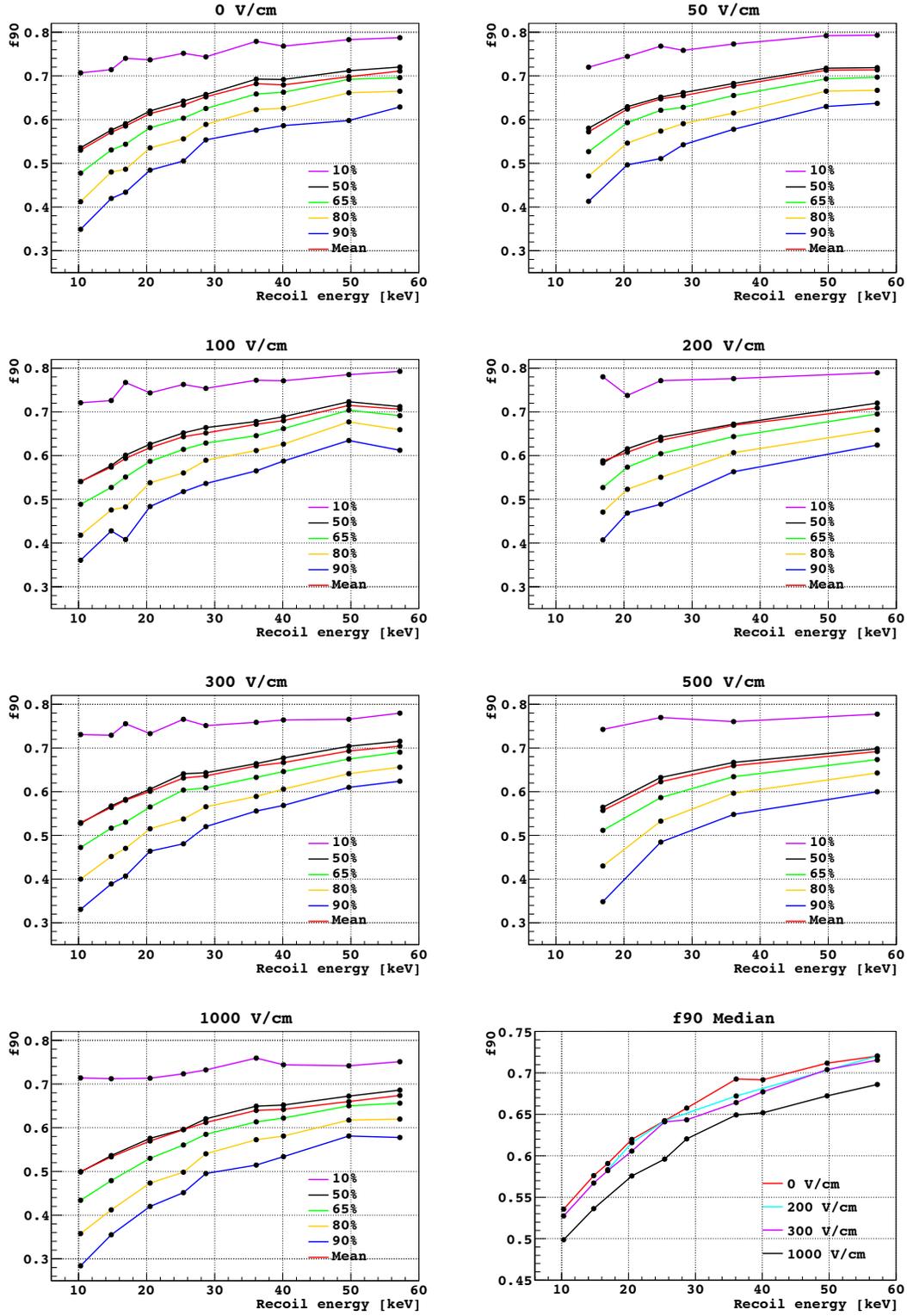
Figure 8.8: Mean f_{90} and 10, 50, 65, 80 and 90% acceptance curve of nuclear recoils in f_{90} as a function of energy. The drift field value is indicated above each graph. The f_{90} median points at $\mathcal{E}_d = 0$, 200, 300 and 1000 V/cm are plotted together in the last graph.

field. The median $\mathtt{f}_{90}$ (or 50% acceptance) as shown in the last graph of Fig. 8.8, decreases by $\sim$0.01 as drift field increases from 0 to $300\,\mathrm{V/cm}$, and by another $\sim$0.03 from $300\,\mathrm{V/cm}$ to $1\,\mathrm{kV/cm}$.

We found good agreement between our measured nuclear recoil $\mathtt{f}_{90}$ distributions and the predictions of the "ratio-of-Gaussians" model described in [98, 102]. The "ratio-of-Gaussians" model assumes that the number of photoelectrons in the prompt and late time windows, N_p and N_l, are normally distributed, independent random variables. By definition $\mathtt{f}_{90} = N_p/(N_p + N_l)$, therefore the assumption on N_p and N_l turns $\mathtt{f}_{90}$ into a ratio of two normally distributed, correlated random variables. Eq. (11) of Ref. [98] gives a close approximation to the probability density function of $\mathtt{f}_{90}$ [1], which we re-expressed as:

$$\frac{\mu x f_p \sigma_l^2 + \mu\left(1 - x\right)\left(1 - f_p\right)\sigma_p^2}{\sqrt{2\pi\left(x^2\sigma_l^2 + \sigma_p^2\left(1 - x\right)^2\right)^3}} \exp\left[-\frac{\left(\mu x\left(1 - f_p\right) - \mu\left(1 - x\right)f_p\right)^2}{2\left(x^2\sigma_l^2 + \left(1 - x\right)^2\sigma_p^2\right)}\right], \qquad (8.4)$$

where x is the fraction of prompt light (*i.e.*, the variable of the $\mathtt{f}_{90}$ axis), μ is the mean number of photoelectrons in the given energy bin, f_p is the median value of the fraction of photoelectrons detected in the first $90\,\mathrm{ns}$ (prompt photoelectrons), $(1 - f_p)$ is the median value of the fraction of photoelectrons detected after $90\,\mathrm{ns}$ (late photoelectrons), σ_p^2 is the variance of the prompt photoelectrons, and σ_l^2 is the variance of the late photoelectrons. Ref. [98, 102] have shown that this model describes the $\mathtt{f}_{90}$ distributions of electron recoil to good precision. The lack of a clean sample of single-scatter nuclear recoils previously prevented the application of this model to nuclear recoils.

In a recent analysis of DarkSide-50 ^{39}Ar background [103], we found that this model gives the best agreement with data when the variance terms are expressed as:

$$\sigma_p^2 = \mu f_p\left(1 + \sigma_{\mathrm{SPE}}^2 + \sigma_{\mathrm{TPB}}^2\right) + \sigma_{n,p}^2, \qquad (8.5)$$

[1]There is a misplaced exponent in Ref. [98].

$$\sigma_l^2 = \mu \left(1 - f_p\right) \left(1 + \sigma_{\mathrm{SPE}}^2 + \sigma_{\mathrm{TPB}}^2\right) + \sigma_{n,l}^2, \tag{8.6}$$

The σ_{SPE}^2 term corresponds to the variance of the SER and σ_{TPB}^2 term describes the statistical fluctuation due to the wavelength-shifter TPB's absorption and re-emission processes of extreme ultraviolet photons. The mean fluorescence efficiency of TPB measured in Ref [104] at 128 nm is $\sim$1.22 with a large uncertainty. If TPB wavelength-shifting follows Poisson statistics, the variance of this process, $1 + \sigma_{\mathrm{TPB}}^2$, should be equal to 1.22. This value agrees well with DarkSide-50 ^{39}Ar data. The $\sigma_{n,p}^2$ and $\sigma_{n,l}^2$ are the variances due to electronic noise in the prompt and late regions.

To use this model on the SCENE data, we plugged in our measured S1 means and $\mathtt{f}_{90}$ medians of nuclear recoils as μ and f_p. For the variances, in addition to Poisson counting statistics, we included the variance due to the width of the SER, $a^2 \mu_p$ and $a^2 \mu_l$, in σ_p^2 and σ_l^2, respectively, and fixed σ_{TPB}^2 to 0.22. In our experiment, at the recoil energies of interest, the variance due to electronic noise is negligible compared to the contribution from counting statistics. We superimposed the model output (with or without σ_{TPB}^2) over the measured $\mathtt{f}_{90}$ distribution for 20.5 keV at $\mathcal{E}_\mathrm{d} = 200\,\mathrm{V/cm}$ in Fig. 8.7(b). The broadening effect of the σ_{TPB}^2 term is only significant for the tails of the distributions. With existing SCENE data, due to low statistics, we cannot justify or reject the presence the σ_{TPB}^2 term. The comparison between data from the rest of the configurations and the model can be found in Appendix D.1.

Although we do not expect an exact match between the model and the measured distribution because of the multiple-scattered neutron background and electron/neutron recoil background from random coincidence, the level of agreement suggests that the model is suitable for application on the $\mathtt{f}_{90}$ distribution of nuclear recoils as well as electron recoils (see Appendix D.2).

With the model, one can use the $\mathcal{L}_{\mathrm{eff},\,^{83\mathrm{m}}\mathrm{Kr}}$ and $\mathtt{f}_{90}$ medians reported here to deduce $\mathtt{f}_{90}$ acceptance in any LAr dark matter detector, whether single or double-phase, either in absence or as a function of the drift field value, as a function of the light yield, electronics,

and noise specific for the dark matter detector of interest. The starting elements are the $\mathcal{L}_{\mathrm{eff},\,^{83m}\mathrm{Kr}}$ and $\mathtt{f}_{90}$ medians reported here as a function of the applied drift field. With the additional input of the light yield of the LAr dark matter detector at null field, one can calculate precisely the correspondence between the nuclear recoil energy scale and the PE scale, and assign a median of the $\mathtt{f}_{90}$ distribution as a function of the detected number of PE. At this point, with the final input coming from the contributions of the electronics and noise specific to the LAr detector under consideration, fluctuations of the $\mathtt{f}_{90}$ distribution and acceptance curves as a function of the detected number of PE can be calculated using the "ratio-of-Gaussians" model introduced in Ref. [98, 102] and elaborated here and in Ref. [103].

8.6 Analysis of the S2 Spectra and determination of $\mathcal{Q}_{\mathrm{y}}$

We define $\mathcal{Q}_{\mathrm{y}}$ as the ionization yield of nuclear recoils. Earlier measurements have shown that ionization yield from electrons, relativistic heavy ions, α particles, fission fragments [95–97] and 6.7 keV nuclear recoils [52] can be enhanced by stronger drift electric fields ($\mathcal{E}_{\mathrm{d}}$). Our data confirmed this for internal conversion electrons from $^{83m}\mathrm{Kr}$, and nuclear recoils in the energy range of 16.9 - 57.2 keV. Ideally, $\mathcal{Q}_{\mathrm{y}}$ should be expressed in detector-independent units of extracted electrons per unit of recoil energy (such as $\mathrm{e}^-/\mathrm{keV}$), but in practice conversion to these units is susceptible to significant systematic uncertainties due to the requirement of single electron calibration for S2. With an extraction field of 3.0 kV/cm, a multiplication field of 4.5 kV/cm and a gas region of 6 mm in height, we did not observe resolved single-electron S2 signals by applying the technique described in Ref. [105]. I will show in the next section an indirect method of determining the single electron S2 gain in a LAr-TPC by taking advantage of the simultaneous measurements of scintillation and ionization. The single electron S2 gain of our data was estimated to be $3.1 \pm 0.3\,\mathrm{PE/e^-}$ by this method.

We also report $\mathcal{Q}_y$ in detector-dependent units of PE/keV along with the ionization yield of ^{83m}Kr. $\mathcal{Q}_y$ relative to the ionization yield of ^{83m}Kr, like $\mathcal{L}_{\text{eff}, \, ^{83m}\text{Kr}}$, permits direct computation of the nuclear recoil ionization yield from the measured ionization yield of ^{83m}Kr in any liquid argon LAr-TPC.

We determined $\mathcal{Q}_y$ in a manner similar to $\mathcal{L}_{\text{eff}, \, ^{83m}\text{Kr}}$, *i.e.* by fitting experimental data with Monte Carlo-generated spectra that took into account the complete geometry of the experiment. But instead of extracting $\mathcal{Q}_y$ independently for each E_{nr} and $\mathcal{E}_{\text{d}}$, we assumed that $\mathcal{Q}_y$ at a given drift field can be modeled by a second order polynomial in recoil energy, and fit together all S2 spectra acquired at the same $\mathcal{E}_{\text{d}}$ with the same polynomial for $\mathcal{Q}_y$. All coefficients of the polynomial were treated as free parameters. This procedure improved the goodness of the fit between data and Monte Carlo, particularly on the left (low PE) side of the peak, as $\mathcal{Q}_y$ depends more strongly on recoil energy than $\mathcal{L}_{\text{eff}, \, ^{83m}\text{Kr}}$ does. In our S1 fits, we assumed $\mathcal{L}_{\text{eff}, \, ^{83m}\text{Kr}}$ is approximately constant in the fit region. Also similar to what was done before for the S1 study, the resolution in S2 was taken as a free parameter in the fit. The resolution in S2 was parametrized as $\sigma_2 = \sqrt{(1 + a^2) \, S2 + R_2^2 S2^2}$, where the ratio of the width of the SER to its mean, a was fixed to 0.3.

By varying R_2 and the coefficients of the $\mathcal{Q}_y$ polynomial, the fit procedure minimizes the χ^2 defined as:

$$\chi^2(\mathcal{E}_{\text{d}}) = \sum_{j=1}^{m} \sum_{i=1}^{n_j} \frac{(O_{j,i} - S_{j,i})^2}{S_{j,i}}, \tag{8.7}$$

where m is the number of recoil spectra acquired with the same $\mathcal{E}_{\text{d}}$, n_j is the total number of bins in the chosen fit region for the j-th spectrum, $O_{j,i}$ is the number of events observed in bin i for the j-th spectrum, and $S_{j,i}$ is the number of events in bin i of the j-th spectrum generated by the Monte Carlo simulations. Each Monte Carlo-generated spectrum was normalized so that within the fit range the total number of events was equal to that in the corresponding experimental spectrum.

The fit results for all five drift fields investigated - ranging from 50 to 500 V/cm - and all four recoil energies under consideration - ranging from 16.9 to 57.2 keV are shown in
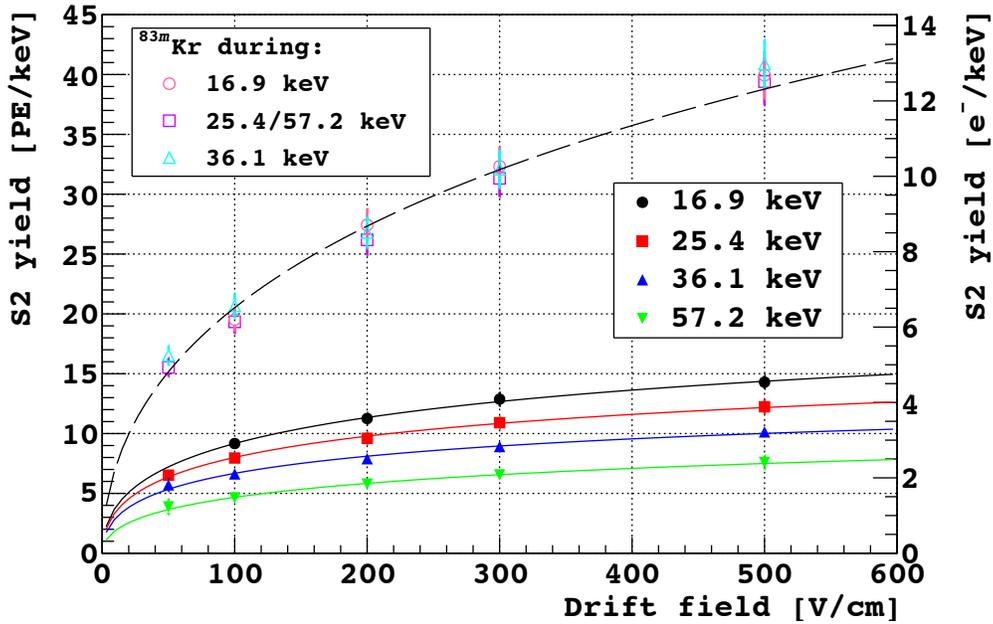
Figure 8.9: Measured S2 yield as a function of $\mathcal{E}_{d}$ at 4 recoil energies. Extraction field is fixed at $3.0\,\mathrm{kV/cm}$ and multiplication field at $4.5\,\mathrm{kV/cm}$. To quote S2 yield in $[\mathrm{e^-/keV}]$, an additional 10% systematic uncertainty is needed to be combined with each error bar to take the uncertainties due to the single electron calibration into account. The dashed curve shows the best fit of the modified Thomas-Imel model (see text) to $^{83m}\mathrm{Kr}$ data. The solid curves show the best fits of the same model (see text) to the nuclear recoil data.

Figs. E.1, E.2, E.3, E.4, and E.5. In each of the figures, the panels show the experimental data at a given recoil energy fit with Monte Carlo data. The χ^2 and the total degree of freedom (ndf) are shown in the last ($57.2\,\mathrm{keV}$) panel of each figure. The agreement between the data and the MC is adequate, although the data is systematically lower than MC on the left tail. This deficit could be a result of limited electron-drift lifetime. Small S2s with larger drift time could more easily drop below the S2 detection threshold.

Fig. 8.9 shows the resulting values of $\mathcal{Q}_{y}$, evaluated with the polynomial at each recoil energy, as a function of $\mathcal{E}_{d}$. The charge yield of $^{83m}\mathrm{Kr}$ is plotted in the same figure for comparison. Fig. 8.10 shows the polynomials of $\mathcal{Q}_{y}$ as a function of E_{nr} measured at 5 different drift fields (50, 100, 200, 300 and $500\,\mathrm{V/cm}$). The error bar associated with each evaluated $\mathcal{Q}_{y}$ represents the quadrature combination of the statistical error returned from the fit and the systematic errors due to each of the sources accounted for. See Table 8.3 for
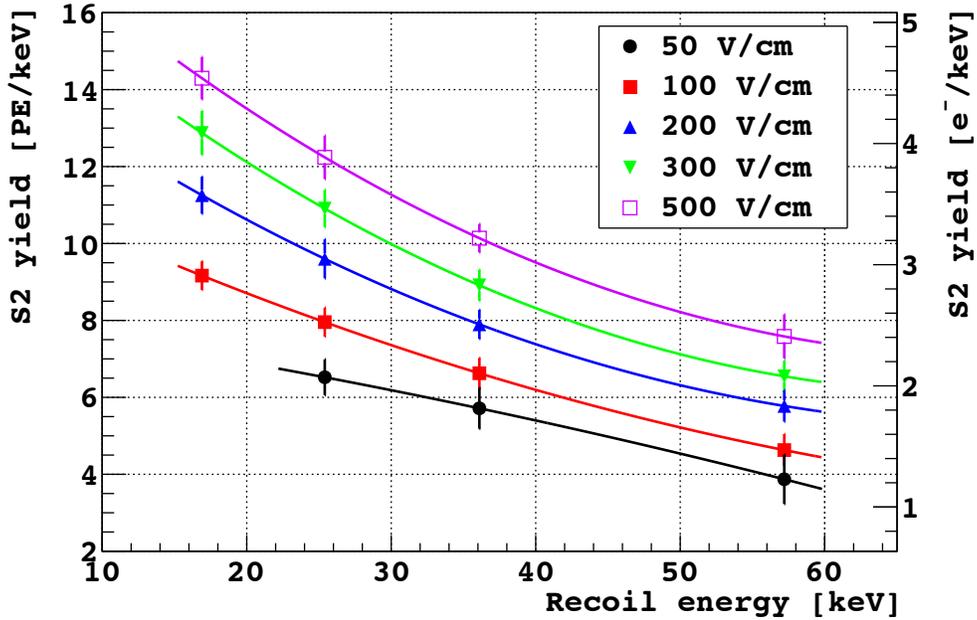
Figure 8.10: Best fit S2 yield as a function of recoil energy at 5 different drift fields (50, 100, 200, 300 and 500 V/cm), with a fixed extraction field of $3.0\,\mathrm{kV/cm}$ and multiplication field of $4.5\,\mathrm{kV/cm}$. To quote S2 yield in $[\mathrm{e^-/keV}]$, an additional 10% systematic uncertainty is needed to be combined with each error bar to take the uncertainties due to the single electron calibration into account.

a detailed account of systematic errors at $\mathcal{E}_\mathrm{d}= 200\,\mathrm{V/cm}$ and Table F.1, F.2, F.3 and F.4 at the other drift fields.

We evaluated the systematic uncertainties of $\mathcal{Q}_\mathrm{y}$ following the same procedures described in the section of $\mathcal{L}_\mathrm{eff,\,^{83m}Kr}$ analysis. In Table 8.3, we show, as an example, the statistical, systematic and combined errors for $\mathcal{Q}_\mathrm{y}$ at $\mathcal{E}_\mathrm{d}= 200\,\mathrm{V/cm}$.

Fits of the resolution of S2 to $\sigma_2 = \sqrt{(1+a^2)\,S2 + R_2^2 S2^2}$, shown in Fig. 8.11, indicates a better resolution of nuclear recoils than β-like events. This is opposite to the S1 case. Differences in how the recombination ratio fluctuates could again play a role in determining this result.

Recoil Energy [keV]	16.9	25.4	36.1	57.2
$\mathcal{Q}_y$ [PE/keV]	11.3	9.6	7.9	5.8
Statistical error	0.1	0.1	0.2	0.3
Systematic errors				
Fit method	0.1	0.2	0.0	0.2
Fit range	0.1	0.1	0.1	0.0
TPC tof	0.1	0.1	0.1	0.1
N tof	0.2	0.2	0.1	0.0
f90	0.2	0.2	0.2	0.0
Kr LY	0.2	0.2	0.2	0.1
Recoil energy				
TPC pos	0.1	0.0	0.0	0.0
EJ pos	0.2	0.3	0.2	0.1
Combined error total	0.5	0.5	0.4	0.4

Table 8.3: Summary of error contributions to individual $\mathcal{Q}_y$ measurements at $\mathcal{E}_d = 200\,\mathrm{V/cm}$. Only minor variations in the magnitude of systematic errors are observed across the range of drift field explored. The combined error for each measurement is shown Fig. 8.10.
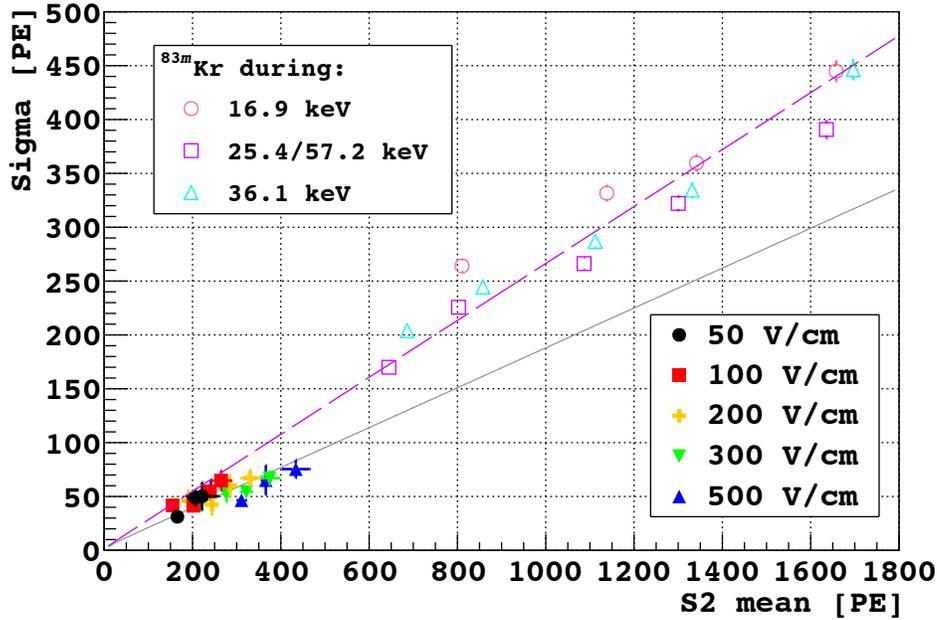
Figure 8.11: Resolution vs. S2 in PE at each recoil energy and drift field. The resolution is determined through the Monte Carlo fit. The resolutions of ^{83m}Kr are shown in the same plot. The best overall fits of R_2 (indicated by the fit curves) are 0.19 ± 0.1 for nuclear recoils and 0.26 ± 0.2 for ^{83m}Kr.

8.7 Anti-correlation between S1 and S2

Fig. 8.12 shows our simultaneous measurement of S1 and S2 yields for both ^{83m}Kr and nuclear recoils up to $\mathcal{E}_{\mathrm{d}} = 500\,\mathrm{V/cm}$. We found in both cases the decrease of S1 yield with drift field, was accompanied by an increase in S2 yield. Such anti-correlation was previously observed and reported for electrons, relativistic heavy ions, α particles and fission fragments [95–97]. In liquid xenon, S1-S2 anti-correlation has also been observed for β-like events (see Ref. [95] for ^{207}Bi response in LXe TPCs and Ref. [106] for studies on γ-ray response). Our observation is the first reported for nuclear recoils. In the case of β-like events, the decrease of S1 and increase of S2 is linked to the partial inhibition of the recombination of electron-ion pairs caused by the drift fields [95]. It is not surprising that the anti-correlation is observed for nuclear recoils in argon, given the documented dependence of the S1 yield on the drift field [29].

The S1-S2 anti-correlation can be helpful in determining the S1 and S2 measurement gains, if we consider the recombination model a good approximation in this drift field and ionization density regime. In this model, the origin of scintillation produced by ionizing radiation in a liquefied noble gas is attributed to the ions R^+ and excitons R^* created along the particle track. Each R^+ (after recombination with e^-) and each R^* quickly form an excited dimer R_2^*, and de-excitation of this dimer to the ground state, $\mathrm{R}_2^* \rightarrow 2\mathrm{R} + h\nu$, is assumed to emit a single UV photon due to the transition between the lowest excited molecular level and the ground level [63].

Ref. [9] provided a detailed description of the recombination model that illustrates the relationship between the number of excitons, N_{ex} and electron-ion pairs, N_{i} produced by an ionizing radiation, and the S1 and S2 signals in a liquid noble gas TPC, which we summarize below. The total number of scintillation photons can be written as,

$$N_{\mathrm{ph}} = \eta_{\mathrm{ex}} N_{\mathrm{ex}} + \eta_{\mathrm{i}} r N_{\mathrm{i}}, \tag{8.8}$$
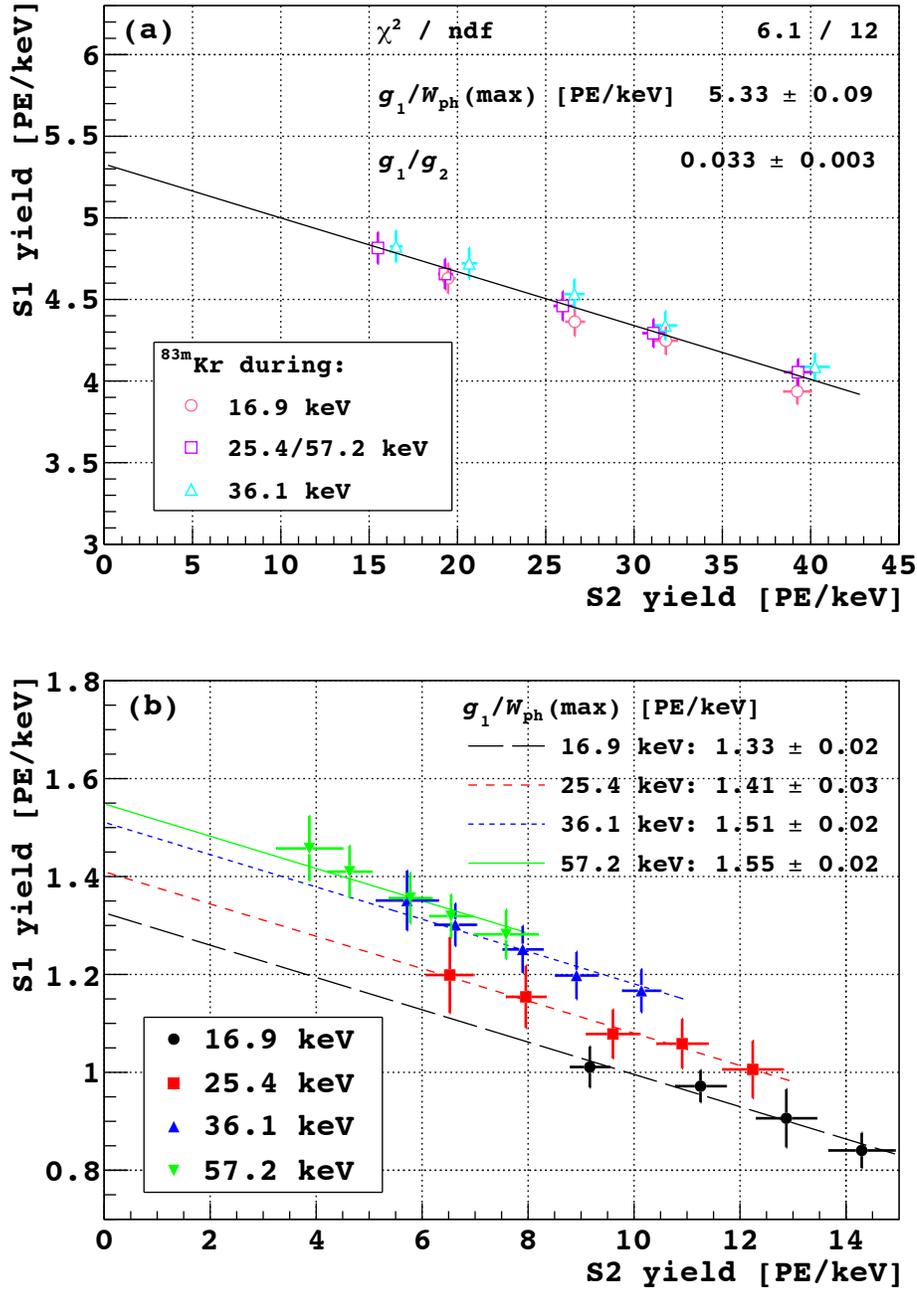
Figure 8.12: (a) S1 yield vs. S2 yield for ^{83m}Kr. The best fit results for Eq. 8.12 are shown. (b) S1 yield vs. S2 yield for nuclear recoils. The slopes of the fit lines in (b) are fixed to the value obtained in (a).

where r is the fraction of ions that recombine, and η_{ex} and η_i are the efficiencies with which direct excitons and recombined ions produce scintillation photons respectively. In the absence of any photon reduction process, we expect η_{ex} and η_i to remain unity. We define the S1 and

S2 measurement gains g_1 and g_2 such that

$$S1 = g_1 N_{\mathrm{ph}}, \text{ and} \tag{8.9}$$

$$S2 = g_2 \left(1 - r\right) N_{\mathrm{i}}, \tag{8.10}$$

where $S1$ and $S2$ are the scintillation and ionization signals respectively in units of PE (both are corrected for z-dependence, see Sec. 7.5 and 7.6). We believe g_1 and g_2 are detector properties, hence they remain constant from electron recoils to nuclear recoils. The average energy required for the production of a single photon in the limit $r \to 1$, $W_{\mathrm{ph}}(\mathrm{max})$, can be written as [63],

$$W_{\mathrm{ph}}(\mathrm{max}) = \frac{E}{N_{\mathrm{ex}} + N_{\mathrm{i}}} = \frac{W}{1 + N_{\mathrm{ex}}/N_{\mathrm{i}}}. \tag{8.11}$$

Here the average energy required for an electron-ion pair production, the so-called W-value, $(W = E/N_{\mathrm{i}}$, where E is the energy of the recoil), is determined to be $23.6 \pm 0.3\,\mathrm{eV}$ in LAr using internal conversion electrons emitted from ^{207}Bi [107]. The inherent S1-S2 anti-correlation in the recombination model can now be expressed as,

$$\frac{S1}{E} = \frac{g_1}{W_{\mathrm{ph}}(\mathrm{max})} - \frac{g_1}{g_2}\frac{S2}{E} \tag{8.12}$$

Taking $W_{\mathrm{ph}}(\mathrm{max}) = 19.5 \pm 1.0\,\mathrm{eV}$ as determined by Doke et al. [63] for ^{83m}Kr internal conversion electrons (assuming same as ^{207}Bi), we obtain $g_1 = 0.104 \pm 0.006\,\mathrm{PE/photon}$, and $g_2 = 3.1 \pm 0.3\,\mathrm{PE/e^-}$ from the fitted parameters in Fig. 8.12(a). We used this g_2 value to convert our measured $\mathcal{Q}_{\mathrm{y}}$ into units of $\mathrm{e^-/keV}$ in the previous section. For the nuclear recoil data shown in Fig. 8.12(b), we fixed the slope of the first order polynomial fit to the value obtained from ^{83m}Kr. As g_1 is constant, the y-intercepts of the fits show an increase of $1/W_{\mathrm{ph}}(\mathrm{max})$ with recoil energy.

Recoil Energy [keV]	C [$\mathrm{e}^-(\mathrm{V/cm})^B$]	N_i	$N_\mathrm{ex}+N_\mathrm{i}$	$N_\mathrm{ex}/N_\mathrm{i}$	$\mathcal{L}$
16.9	0.61±0.12	135±21	216±22	0.6±0.3	0.250±0.006
25.4	0.42±0.08	161±22	345±35	1.2±0.4	0.265±0.007
36.1	0.34±0.07	183±25	524±53	1.9±0.5	0.283±0.006
57.2	0.38±0.13	253±77	853±86	2.4±1.1	0.291±0.006

Table 8.4: Columns C and N_i are the fit results of nuclear recoil data in Fig. 8.9 to the modified Thomas-Imel box model with B fixed to the value obtained with the fit to ^{83m}Kr (see text). Columns $N_\mathrm{ex}+N_\mathrm{i}$ and $\mathcal{L}$ are the computed values based on Fig. 8.12 (see text). Column $N_\mathrm{ex}/N_\mathrm{i}$ is computed with Columns N_i and $N_\mathrm{ex}+N_\mathrm{i}$.

We fit our measured S2 yields as a function of drift field shown in Fig. 8.9 with an empirical modification [52] of the Thomas-Imel box model [108],

$$Q_\mathrm{y} = \frac{N_\mathrm{i}}{E\xi}\ln\left(1+\xi\right), \; \xi = \frac{N_\mathrm{i}C}{\mathcal{E}_\mathrm{d}^B}, \tag{8.13}$$

where B and C are constants. In this modified model, $\xi \propto \mathcal{E}_\mathrm{d}^{-B}$ instead of $\mathcal{E}_\mathrm{d}^{-1}$ as originally assumed by Thomas and Imel. Following our earlier assumption that the W-value of ^{83m}Kr is the same as ^{207}Bi, we obtain $N_\mathrm{i}=1.76\times10^3\,\mathrm{e}^-$ for ^{83m}Kr and plugged this value in Eq. 8.13 for the fit. The best fit to ^{83m}Kr calibration data yields $C_{83m\mathrm{Kr}}=0.19\pm0.03\,(\mathrm{V/cm})^B/\mathrm{e}^-$ and $B=0.62\pm0.03$.

Using this value of B, we left C and N_i as the free parameters for the fits to the nuclear recoil data in Fig. 8.9. The best fit values and errors for C and N_i are listed in Table 8.4. We also calculated the values in the $N_\mathrm{ex}+N_\mathrm{i}$ column based on the x-intercepts of Fig. 8.12(b) and the value of g_2. We then used the N_i and $N_\mathrm{ex}+N_\mathrm{i}$ columns to compute $N_\mathrm{ex}/N_\mathrm{i}$. The last column, $\mathcal{L}$, is the overall quenching factor of nuclear recoils. It is equal to the ratio of each y-intercept in Fig. 8.12(b) to the y-intercept of Fig. 8.12(a).

Mei et al. attributed the reduction of scintillation efficiency to two major mechanisms: (1) energy loss due to nuclear collisions, and (2) scintillation quenching due to high ionization and excitation density induced by nuclear recoils [109]. Lindhard's theory describes the first mechanism (f_n), and Birks' saturation law models the latter (f_l). They argued that since
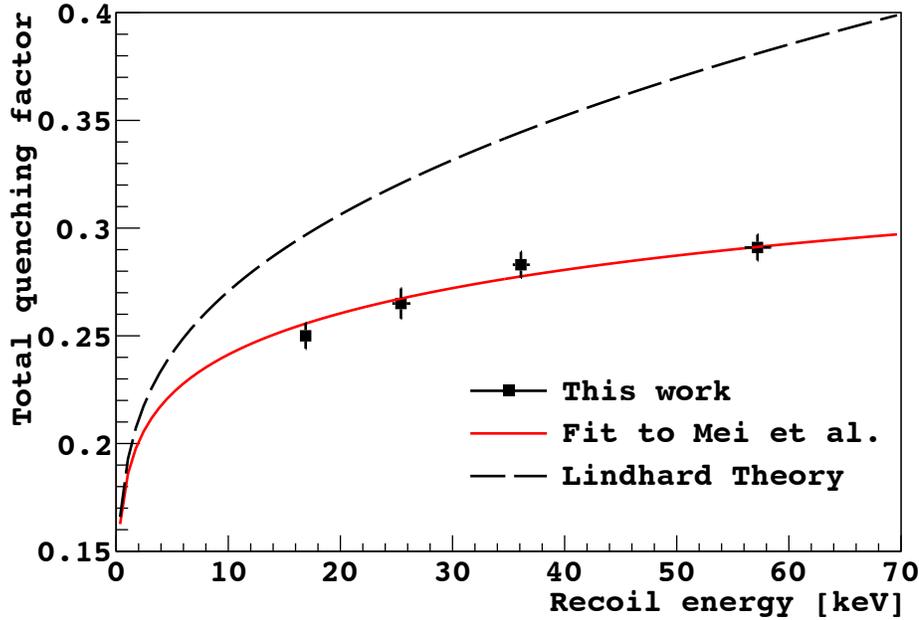
Figure 8.13: Total quenching factor $\mathcal{L}$ compared to Lindhard's theory and the Lindhard-Birks combined model proposed by Mei et al. The best fit curve to Mei's model with Birks' constant kB as free parameter yields $kB = 4.8 \pm 0.5 \times 10^{-4}\,\mathrm{MeV}^{-1}\mathrm{g\,cm}^{-2}$.

these two effects are independent of each other, one could combine the two directly ($f_\mathrm{n} \cdot f_\mathrm{l}$) to explain the observed reduction of scintillation yield for nuclear recoils in noble liquids. We compared their prediction to our data. But in stead of interpreting $f_\mathrm{n} \cdot f_\mathrm{l}$ as the reduction in scintillation alone, we consider it equal to the total reduction factor of scintillation and ionization combined, i.e., $\mathcal{L} = f_\mathrm{n} \cdot f_\mathrm{l}$. The best fit curve to Mei's model with Birk's constant kB as free parameter yields $kB = 4.8 \pm 0.5 \times 10^{-4}\,\mathrm{MeV}^{-1}\mathrm{g\,cm}^{-2}$. This is close to the value determined by Mei [109] with the experimental results of [110]. It would be the same if the quenching factor of ^{36}Ar ion at $\mathcal{E}_\mathrm{d} = 3.2\,\mathrm{kV/cm}$ instead of at null field was used in Mei's method.
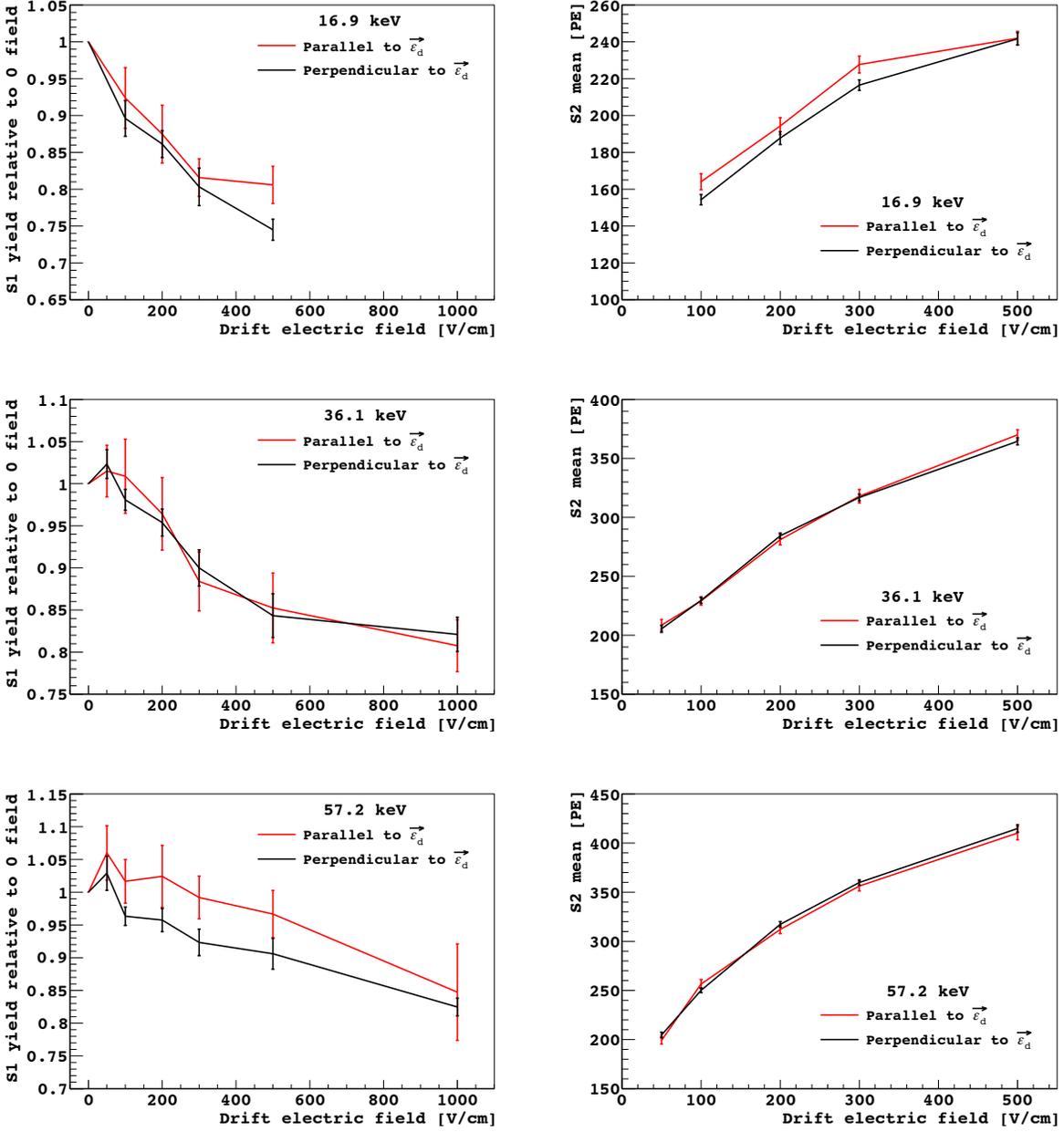
Figure 8.14: Scintillation yield relative to null field (left panels) and ionization yield with non-zero drift field (right panels) of nuclear recoils at 16.9, 36.1 and 57.2 keV. **Black:** momentum of nuclear recoil is perpendicular to $\mathcal{E}_d$. **Red:** momentum of nuclear recoil is parallel to $\mathcal{E}_d$. Sources of systematic uncertainties common to both field orientations are not included in the error bars.

8.8 Comparison of scintillation and ionization from recoils parallel and perpendicular to the drift field

Sensitivity to the direction of detected WIMP recoils would give a powerful signature for identifying a signal observed in a direct-detection dark matter experiment with the galactic dark matter [111].

Applied electric fields are known to modify the recombination of electron-ion pairs in ionizing radiation tracks. Columnar recombination [112–114] models suggest that the magnitude of these effects should in some circumstances vary with the angle between the field and the track direction, and these effects have been discussed as possible ways to achieve direction sensitive WIMP recoil detection in LAr or GXe targets [115, 116]. Such directional effects have been reported from experiments using tracks from α particles [117] and protons [118] in liquid argon.

As we have shown, electron-ion recombination for nuclear recoil tracks in liquid argon also depends strongly on the applied electric field. If a directional effect on recombination is present in LAr, we would expect to measure different scintillation and/or ionization responses for nuclear recoils of the same energy but with different track orientations. We therefore configured our neutron beam and neutron detector placement so as to allow us to simultaneously record nuclear recoil events with tagged initial momentum in directions parallel and perpendicular to the drift field applied to the liquid argon TPC. The neutron beam direction was selected at a downward angle with respect to the horizontal, dictated by the kinematics at the neutron energy in use. The two-angle goniometric mount then allowed the neutron detectors to be placed at positions corresponding to a single scattering angle but at different azimuthal angles corresponding to recoil nucleus directions parallel or perpendicular to the (vertical) drift field. The results reported in the preceding sections of this paper combined the data from the two neutron counters with the initial recoil direction perpendicular or near perpendicular to the drift field.

In order to produce a direction-sensitive response, the recoil nucleus must have enough energy (range) to form a track with a definite direction. Following the arguments of [116], one might expect such a response to start for recoils above the energy where the length of the track exceeds the Onsager radius, $r_O = e^2/4\pi\epsilon K$. This is the distance between a positive ion and a free electron for which the potential energy of the electrostatic field, $e^2/4\pi\epsilon r_O$, is equal to the kinetic energy of a thermal electron, $K = 3kT/2$. In liquid argon ($T = 87\,\mathrm{K}$, $\epsilon = 1.5$) $r_O \simeq 80\,\mathrm{nm}$. The range of argon recoils in liquid argon [119] is about $90\,\mathrm{nm}$ at $36.1\,\mathrm{keV}$. It increases to $135\,\mathrm{nm}$ at $57.2\,\mathrm{keV}$, substantially exceeding the r_O. A similar value for the energy at which directional effects might start is obtained in the line-charge model of Ref. [120].)

Fig. 8.14 shows the comparison of average S1 and S2 responses for the two track orientations. The scintillation and ionization yields normalized to their values at zero field are plotted as a function of the applied electric field. Any differences for parallel and perpendicular tracks for both signals are seen to be very small compared to the statistical errors and the overall trend of field dependence for the 16.9 and $36.1\,\mathrm{keV}$ energies. The S1 response at $57.2\,\mathrm{keV}$ does exhibit an orientation difference, but with marginal statistical significance. Further investigation with more precise measurements at higher recoil energies may be interesting for deciding the potential of LAr-TPC as a direction sensitive WIMP detector.

Chapter 9

Conclusions

This work presents the following new results for argon recoils in liquid argon in the energy range 10.3 to 57.2 keV and the drift field range 0 - 1000 V/cm (16.9 - 57.2 keV and 50 - 500 V/cm for ionization):

- values for the nuclear recoil scintillation yield relative to that of ^{83m}Kr $(\mathcal{L}_{\text{eff}, \, ^{83m}\text{Kr}})$ and the associated uncertainties, showing clear field and energy dependences of the scintillation yield

- detailed information on the distributions of the pulse shape discrimination parameter $\mathtt{f}_{90}$

- values and uncertainties for $\mathcal{Q}_{\text{y}}$, the apparatus-independent absolute yield of extracted ionization electrons per keV kinetic energy for both nuclear recoils and ^{83m}Kr at an extraction field of 3.0 kV/cm

- a method and results of a search for sensitivity of the LAr-TPC response to the initial direction of nuclear recoils with respect to the applied electric field

These data were intended for use in calibration and parameter optimization for the Dark-Side series of LAr-TPC's for dark matter searches. The results show that the real effects of electric field on the responses of LAr-TPC's are substantially more complicated than the small, energy-independent changes that have generally been assumed up to now. The present

results should be valuable in connection with the design and calibration of any detector using scintillation and ionization in liquid argon to detect nuclear recoils. The results also suggest a line of further investigation of a direction-sensitive effect in the response of LAr-TPC's. Direction-sensitivity would be of great interest in unambiguously associating any WIMP-like signal in such a device with the apparent motion of the galactic halo.

Appendix A

A step-by-step guide to generating WIMP-nucleon cross section upper limits for LAr detectors

This guide explains the Poisson method [23] to generate the upper limits for WIMP-nucleon cross section, given the inputs of:

1. the energy spectrum of WIMP-induced nuclear recoils,

2. the S1 and S2 light yield of the LAr detector,

3. the scintillation (S1) and ionization (S2) efficiencies of nuclear recoils,

4. the S1 and S2 signal resolution functions,

5. the trigger efficiency of data acquisition as a function of S1 magnitude,

6. the distributions of discrimination parameters for nuclear recoil events and

7. the WIMP acceptance regions in the discrimination parameter spaces.

The details on how each inputs can be determined are not included here but references are cited in the relevant sections of this chapter. Algorithmic optimization is not discussed here.

A.1 Energy spectrum of WIMP-induced nuclear recoils

This input for the upper limit calculation does not require any specific information from the WIMP detector. The spectrum scales with the number of the target nuclei N_N, the local WIMP density ρ_0, and the inverse of the WIMP mass M_W, as shown in Eq. 3.1. Less straightforward are its dependence on WIMP velocity distribution in the galaxy and the calculation of WIMP-nucleus cross section from WIMP-nucleon cross section. Ref. [22, 23] and Sec. 1.2.2 of Ref. [11] present the derivation of both the velocity distribution and the cross section terms under the conventional assumptions. Fig. A.1 shows an example of the energy spectrum with a WIMP mass of $100\,\text{GeV}$ and a WIMP-nucleon cross section of $10^{-45}\,\text{cm}^2$. A sophisticated implementation for the energy spectrum calculation can also be found in the open source program MicrOMEGAs [121].
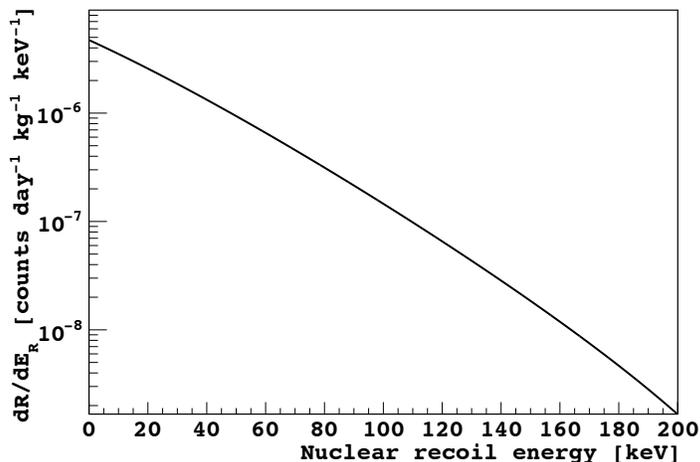
Figure A.1: Predicted WIMP-induced nuclear recoil spectrum for a $100\,\text{GeV}$ WIMP with a WIMP-nucleon scattering cross section of $10^{-45}\,\text{cm}^2$. The standard isothermal-WIMP-halo model is assumed, with $v_{\text{escape}} = 544\,\text{km/s}$, $v_0 = 220\,\text{km/s}$, $v_{\text{Earth}} = 232\,\text{km/s}$, and $\rho_{\text{dm}} = 0.3\,\text{GeV}/(\text{c}^2\text{cm}^3)$.

In order to obtain sufficient statistics in the nuclear recoil acceptance region for the simulations later, one should assume a relatively large WIMP-nucleon cross section in preparing

the energy spectrum, which should be at least a couple orders of magnitude larger than the expected upper limit.

A.2 Distribution of nuclear recoils in the discrimination parameter spaces

The next crucial step is simulating the observable signals for the nuclear recoil events given the energy spectrum. Those signals include magnitudes of S1 (and S2 if it is also measured) and $\mathtt{f}_{90}$ for S1 signals.

To obtain the expected spectrum of S1 signals in the LAr detector, one first needs to multiply the recoil energy of a given energy bin with the measured light yield of the detector, such as one determined with the ^{83m}Kr calibration source, and the S1 efficiency of nuclear recoils relative to the calibration source (*i.e.*, $\mathcal{L}_{\text{eff, }^{83\text{m}}\text{Kr}}$, see Sec. 8.3). One should note that these efficiencies depend both on the recoil energy and on the selected drift electric field. One can also choose to perform the calculation event by event. The expected spectrum of S2 signals can be obtained in an analogous manner.

These mappings from nuclear recoil energy to S1 and S2 signals produce spectra of perfect resolution. One can convolve these spectra with the corresponding resolution functions of S1 and S2 and multiply the results of the convolution with the trigger efficiency functions to obtain the expected S1 and S2 spectra of the detector given the assumed WIMP-nucleon cross section. An example of the simulated S1 spectrum is shown on the left panel of Fig. A.2.

From those spectra, one can simulate the distribution of the nuclear recoils in the discrimination parameter spaces, such as $\mathtt{f}_{90}$ for S1 pulse shape (see Sec. 8.5) and the ratio of S2/S1 (see Sec. 8.7). An example of the simulated S1 spectra is shown on the right panel of Fig. A.2.
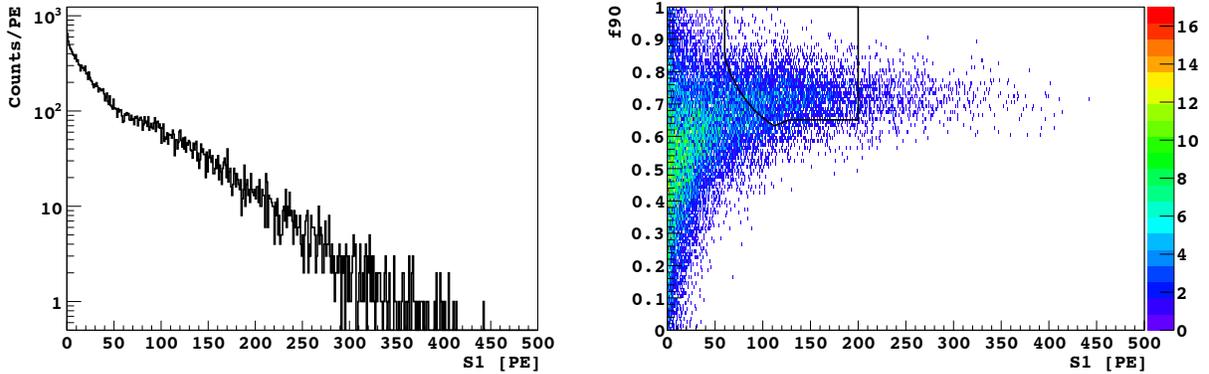
Figure A.2: **Left:** predicted S1 spectrum from a LAr-TPC with a drift electric field of 200 V/cm for a 100 GeV WIMP with a WIMP-nucleon scattering cross section of $10^{-40}\,\mathrm{cm^2}$ over an total exposure of 1438 kg·day. I assume a Poisson resolution function and a 100% trigger efficiency.

Right: predicted 2D distribution of $\mathtt{f}_{90}$ vs. S1 for the same sample of events. The enclosed region in the black contour indicates a possible nuclear recoil acceptance region.

A.3   WIMP-nucleon cross section upper limit

After the operations in the previous section, we have obtained the values of the discrimination parameters for each simulated nuclear recoil. This allows us to apply the selection cuts whose purpose is to reduce the expected number of background events in the acceptance region to near zero. We record the number of simulated nuclear recoil events retained in the acceptance region, N_{sim}.

We suppose the random variable N describes in the actual data of the LAr WIMP search experiment the number of WIMP-induced nuclear recoils populated the acceptance region. We assume N follows a Poisson distribution with parameter λ. (A more rigorous treatment should also assume a Poisson random variable N_{bg} for the number of background events in the acceptance region, with parameter λ_{bg} and use $N + N_{\mathrm{bg}}$ to describe the total number of events in the acceptance region. This is beyond the scope of this guide.)

The confidence limit (CL) for λ can be subsequently evaluated with the observed value of N. For instance, if we observe zero event in the acceptance region, and want to determine the 90% CL for λ, we should solve for the condition on λ that satisfies Prob($N=0$) < 1-90%.

This gives $\lambda > 2.3$. Finally, the 90% CL for the WIMP-nucleon cross section upper limit for the assumed WIMP mass can be obtained with the WIMP-nucleon cross section first assumed in the simulation multiplied by $(2.3/N_{\mathrm{sim}})$.

The same procedure can be repeated for other WIMP masses over the entire WIMP-nucleon cross section upper limit curve. Fig. A.3 shows an example of this curve given the conventional assumptions and background rejection cuts applied only to S1 pulse shape.
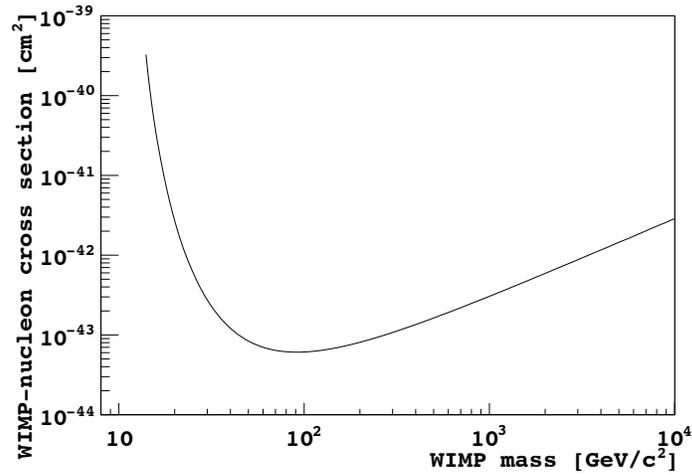
Figure A.3: An example of WIMP-nucleon cross section upper limit curve (90% CL) given the conventional galactic halo and nuclear physics assumptions. The background rejection cuts are applied only to S1 pulse shape.

Appendix B

Fits to S1 spectra
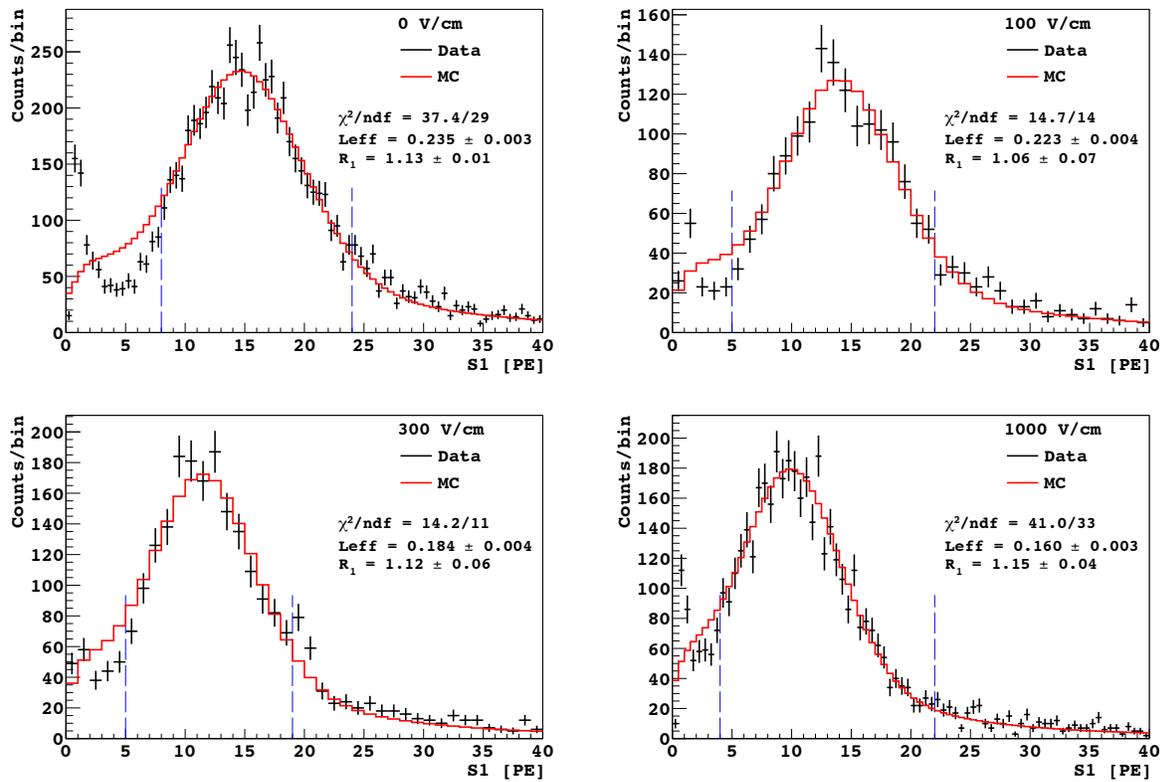
Figure B.1: All Panels. **Black:** experimental data collected for 10.3 keV nuclear recoils. **Red:** Monte Carlo fit of the experimental data. The range used for each fit is indicated by the vertical **blue** dashed lines.
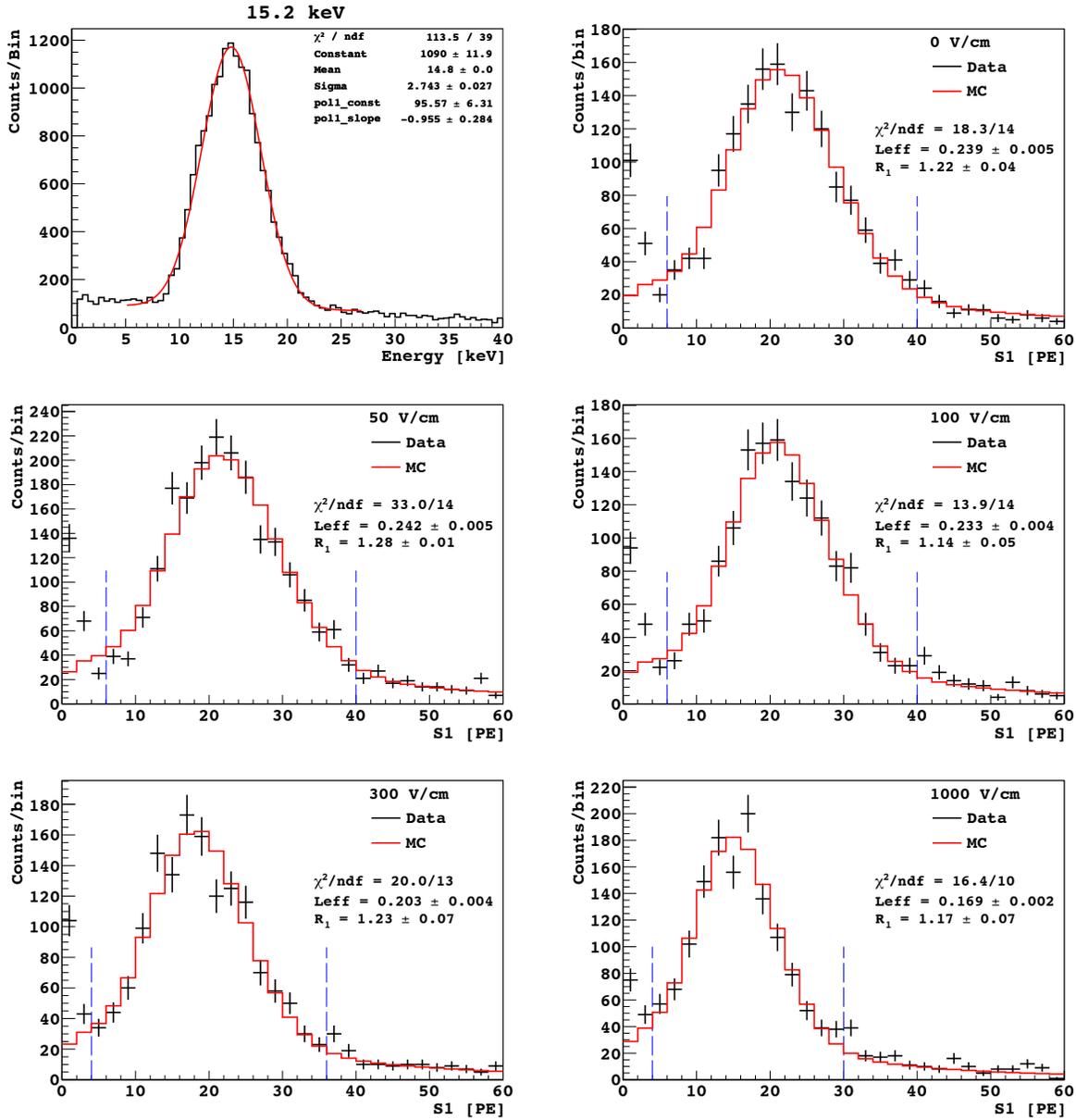
Figure B.2: Top Left Panel. **Black:** GEANT4-based simulation of the energy deposition in the SCENE detector at the setting devised to produce 14.8 keV nuclear recoils. **Red:** Gaussian plus first order polynomial fit to the black histogram.

All Other Panels. **Black:** experimental data collected for 14.8 keV nuclear recoils. **Red:** Monte Carlo fit of the experimental data. The range used for each fit is indicated by the vertical **blue** dashed lines.
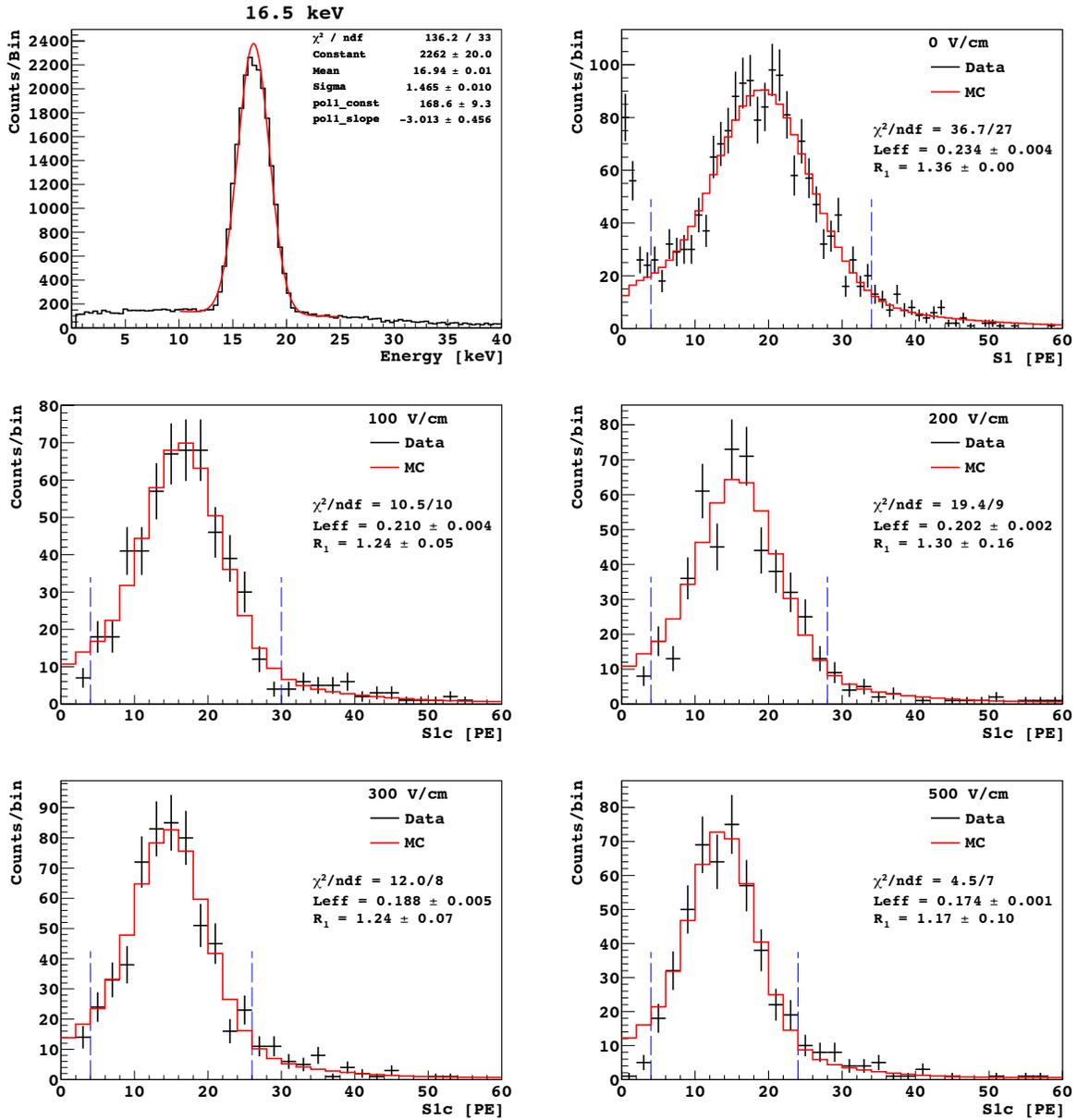
Figure B.3: 16.9 keV nuclear recoils. Details see Fig. B.2.
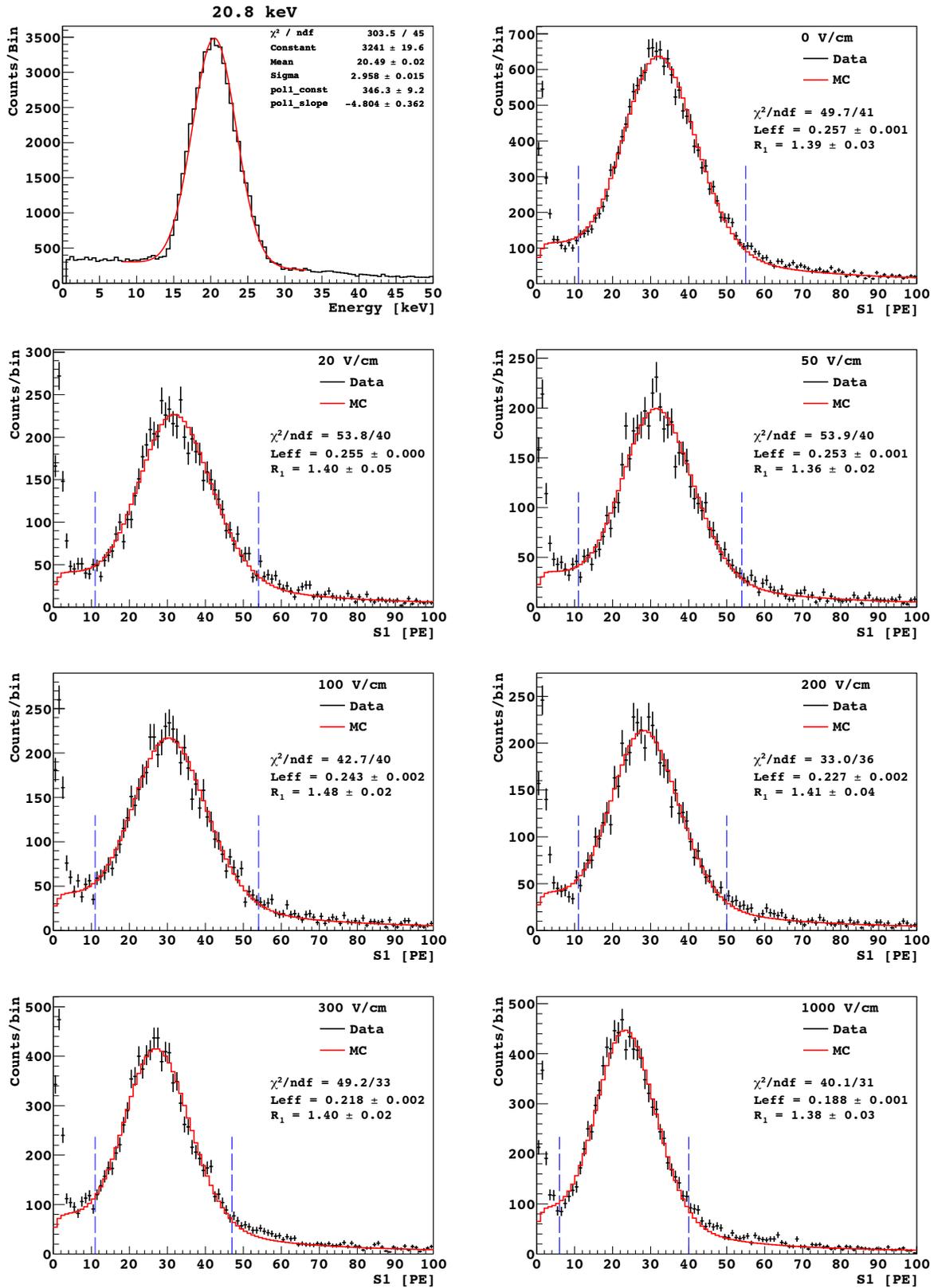
Figure B.4: 20.5 keV nuclear recoils. Details see Fig. B.2.
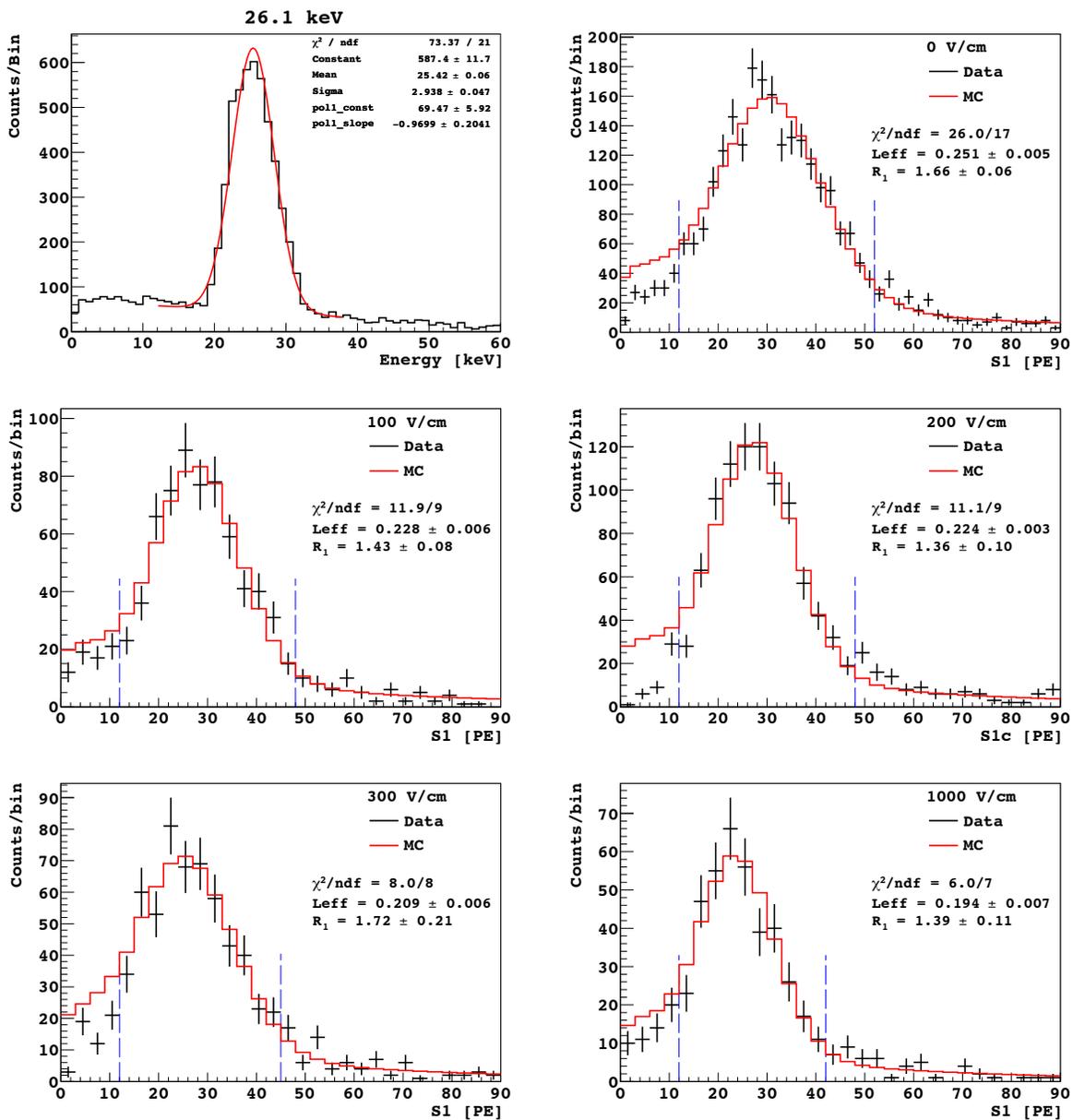
Figure B.5: 25.4 keV nuclear recoils. Details see Fig. B.2.
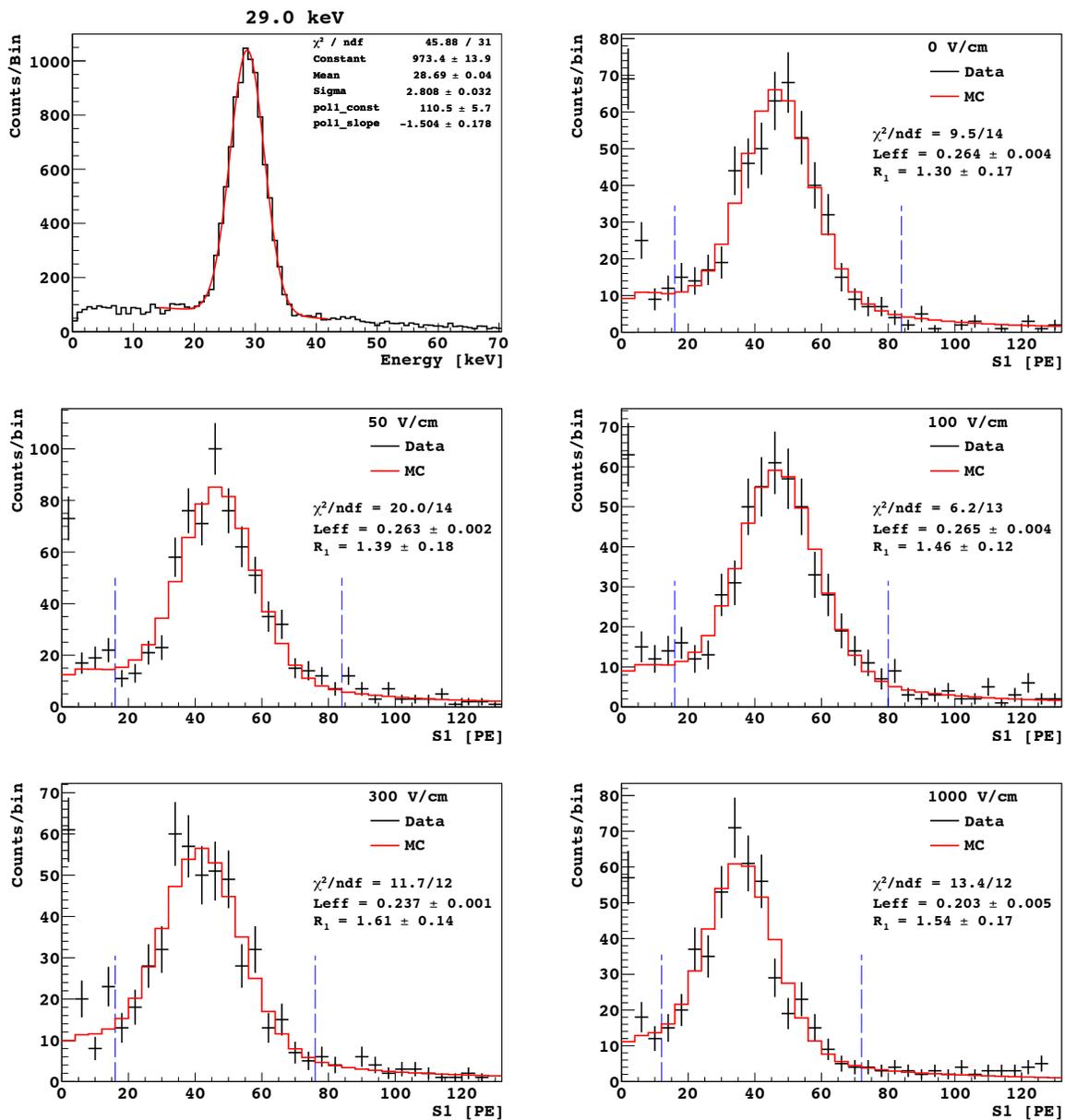
Figure B.6: 28.7 keV nuclear recoils. Details see Fig. B.2.
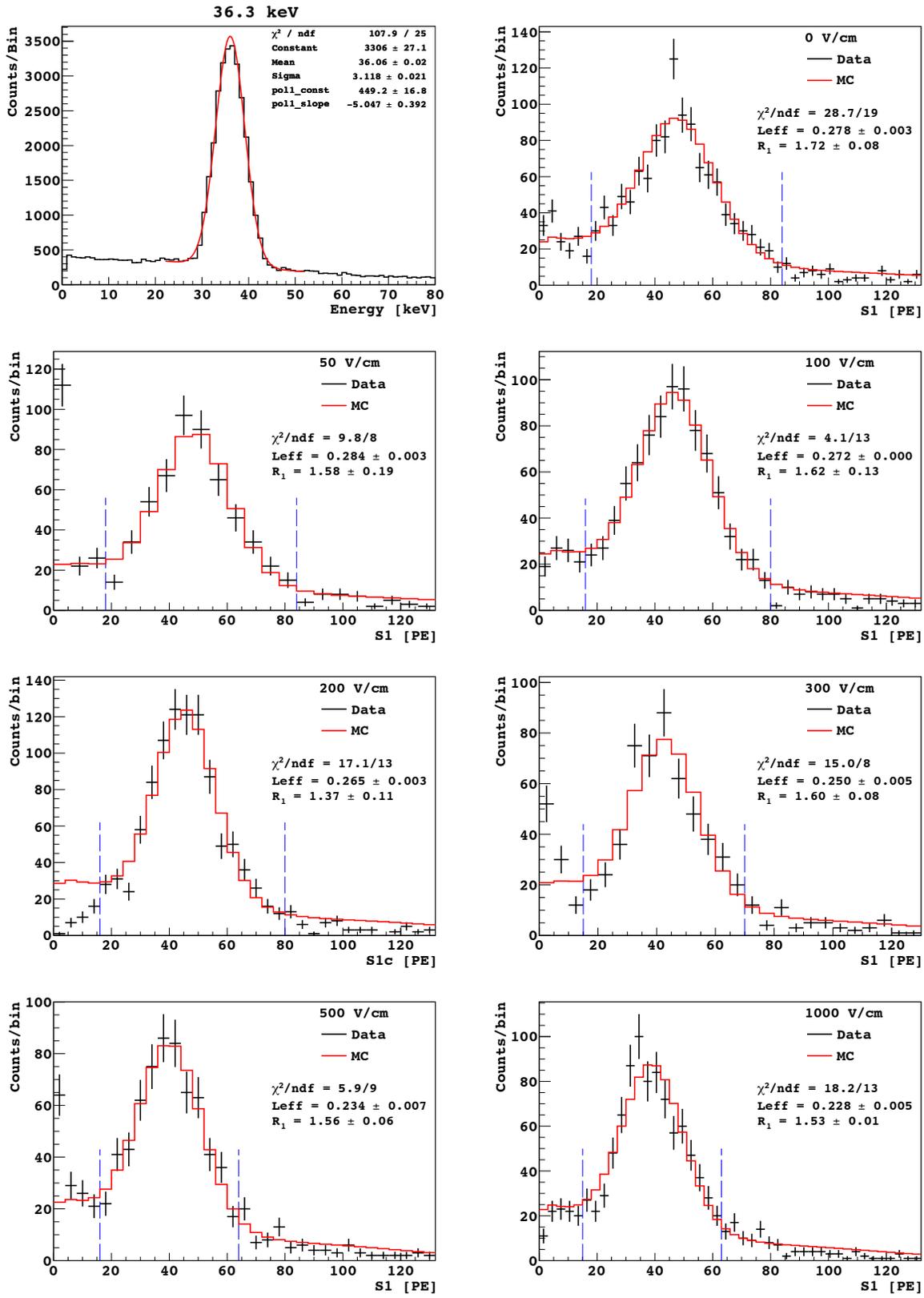
Figure B.7: 36.1 keV nuclear recoils. Details see Fig. B.2.
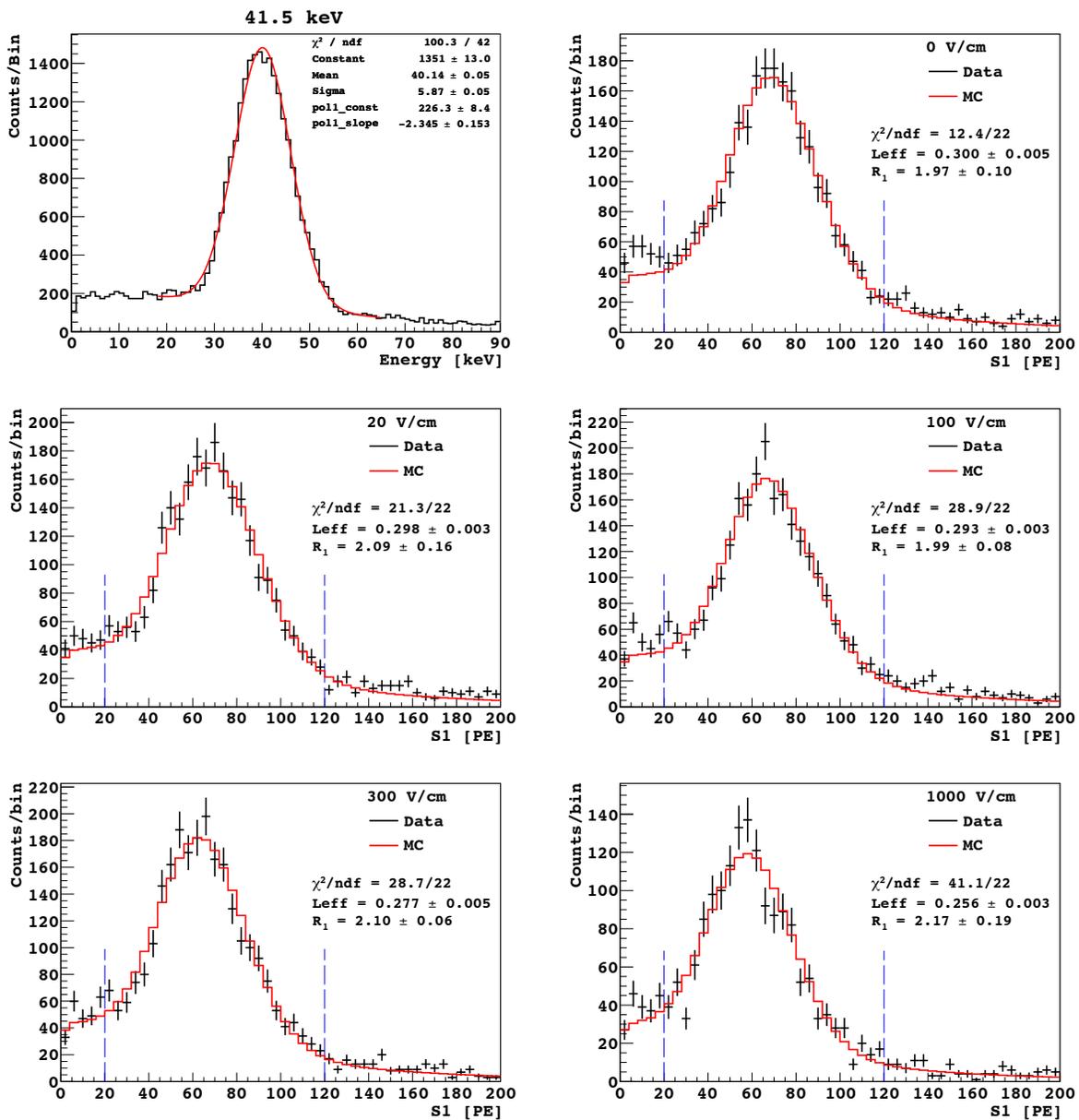
Figure B.8: 40.1 keV nuclear recoils. Details see Fig. B.2.
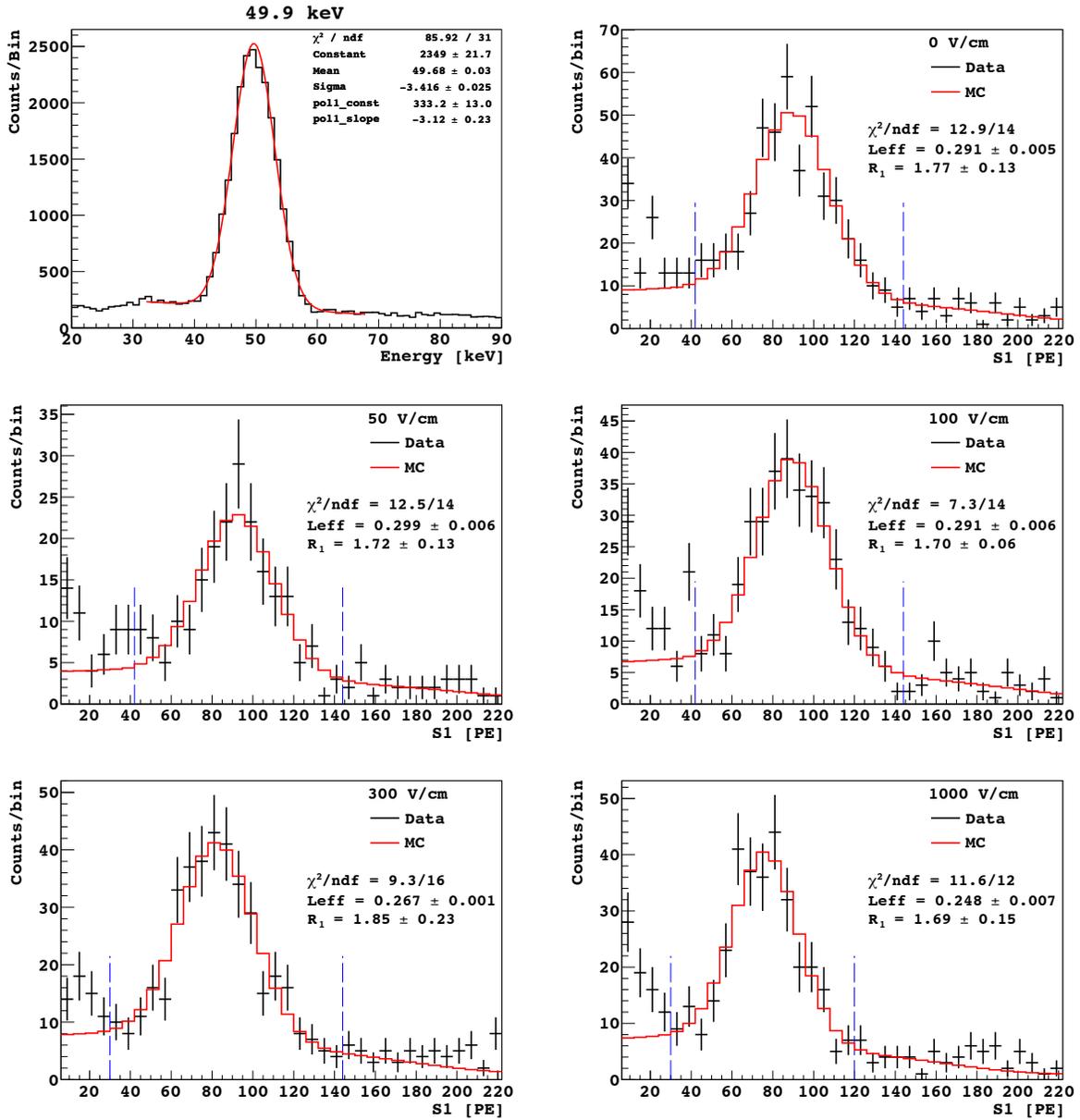
Figure B.9: 49.7 keV nuclear recoils. Details see Fig. B.2.
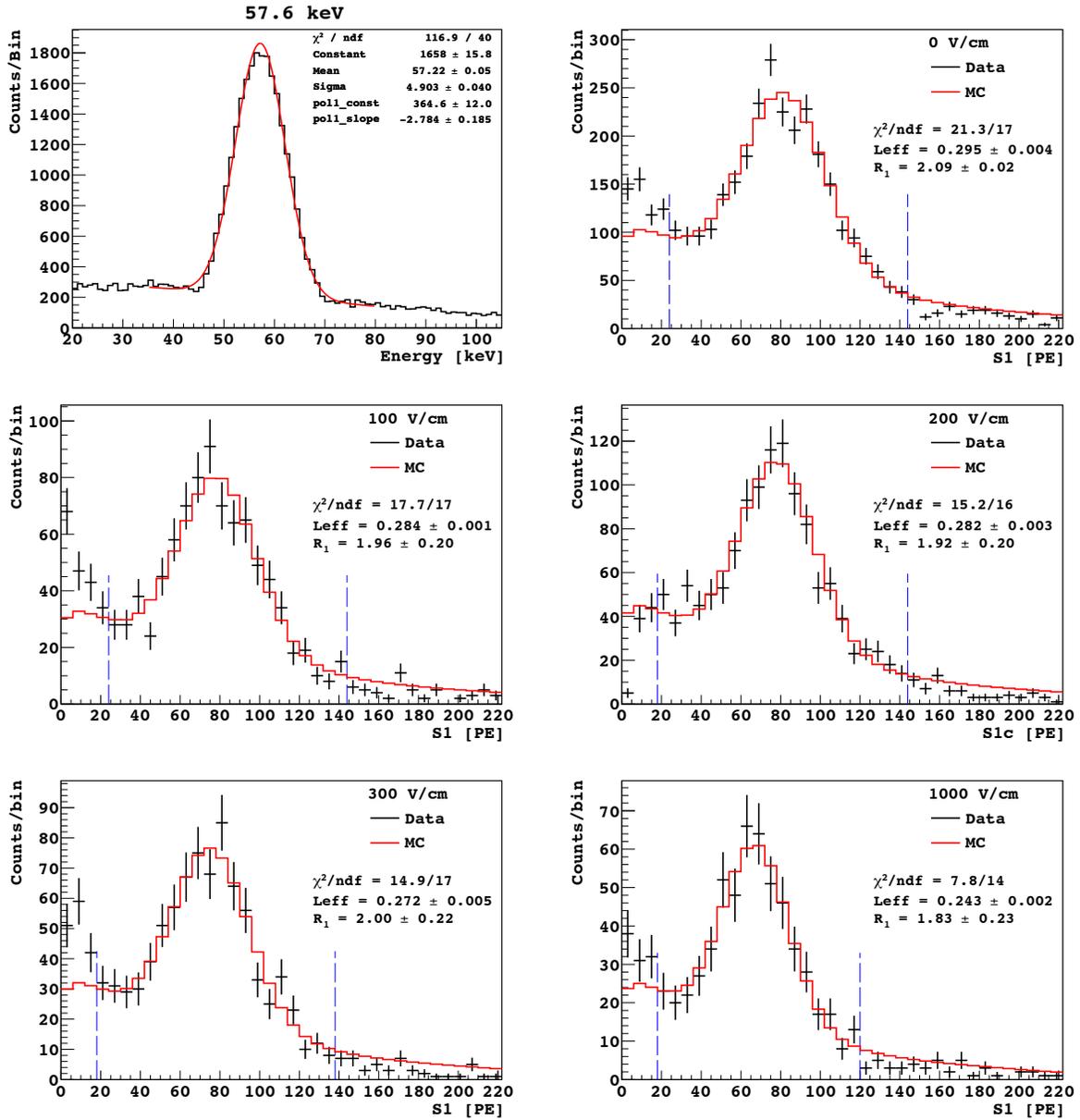
Figure B.10: 57.2 keV nuclear recoils. Details see Fig. B.2.

Appendix C

Tables of $\mathcal{L}_{\mathrm{eff},\,^{83m}\mathrm{Kr}}$ at non-zero drift fields

| Recoil Energy [keV]	10.3	14.8	16.9	20.5	25.4	28.7	36.1	40.1	49.7	57.2
$\mathcal{L}_{\mathrm{eff},\,^{83m}\mathrm{Kr}}$		0.242		0.253	0.249	0.263	0.284		0.299	0.303
Statistical error		0.005		0.001	0.003	0.002	0.003		0.006	0.006
Systematic error source										
Fit method		0.004		0.002	0.014	0.004	0.004		0.001	0.021
Fit range		0.006		0.001	0.011	0.000	0.000		0.002	0.000
TPC tof		0.002		0.001	0.001	0.003	0.003		0.005	0.002
N tof		0.004		0.001	0.003	0.002	0.004		0.002	0.003
f90		0.002		0.000	0.000	0.002	0.002		0.002	0.000
Kr LY		0.005		0.005	0.005	0.005	0.006		0.006	0.006
Recoil energy										
TPC pos		0.001		0.001	0.001	0.001	0.001		0.001	0.001
EJ pos		0.010		0.008	0.007	0.005	0.006		0.003	0.006
Combined error total		0.015		0.010	0.020	0.009	0.011		0.011	0.023

Table C.1: Summary of error contributions to individual $\mathcal{L}_{\mathrm{eff},\,^{83m}\mathrm{Kr}}$ measurements at $\mathcal{E}_{\mathrm{d}} = 50\,\mathrm{V/cm}$.

Recoil Energy [keV]	10.3	14.8	16.9	20.5	25.4	28.7	36.1	40.1	49.7	57.2
$\mathcal{L}_{\mathrm{eff},\,^{83m}\mathrm{Kr}}$	0.223	0.233	0.210	0.243	0.228	0.265	0.272	0.293	0.291	0.284
Statistical error	0.004	0.004	0.004	0.002	0.006	0.004	0.000	0.003	0.006	0.001
Systematic error source										
Fit method	0.003	0.000	0.002	0.004	0.002	0.000	0.004	0.004	0.002	0.003
Fit range	0.001	0.000	0.004	0.000	0.003	0.001	0.001	0.002	0.002	0.002
TPC tof	0.002	0.000	0.001	0.001	0.002	0.001	0.002	0.003	0.000	0.001
N tof	0.003	0.002	0.001	0.001	0.002	0.002	0.004	0.003	0.003	0.001
f90	0.003	0.000	0.004	0.001	0.000	0.000	0.001	0.001	0.000	0.000
Kr LY	0.004	0.005	0.004	0.005	0.005	0.005	0.005	0.006	0.006	0.006
Recoil energy										
TPC pos	0.001	0.001	0.001	0.001	0.001	0.001	0.001	0.001	0.001	0.001
EJ pos	0.007	0.009	0.004	0.007	0.007	0.005	0.005	0.009	0.003	0.006
Combined error total	0.011	0.011	0.009	0.010	0.012	0.009	0.010	0.013	0.010	0.009

Table C.2: Summary of error contributions to individual $\mathcal{L}_{\mathrm{eff},\,^{83m}\mathrm{Kr}}$ measurements at $\mathcal{E}_{\mathrm{d}} = 100\,\mathrm{V/cm}$. The combined error for each measurement is shown Fig. 8.4.

Recoil Energy [keV]	10.3	14.8	16.9	20.5	25.4	28.7	36.1	40.1	49.7	57.2
$\mathcal{L}_{\mathrm{eff},\,^{83m}\mathrm{Kr}}$			0.202	0.227	0.224		0.265			0.282
Statistical error			0.002	0.002	0.003		0.003			0.003
Systematic error source										
Fit method			0.002	0.002	0.002		0.005			0.009
Fit range			0.000	0.001	0.004		0.000			0.002
TPC tof			0.001	0.002	0.002		0.002			0.000
N tof			0.003	0.003	0.001		0.004			0.002
f90			0.004	0.002	0.000		0.001			0.000
Kr LY			0.004	0.005	0.004		0.005			0.006
Recoil energy										
TPC pos			0.001	0.001	0.001		0.001			0.001
EJ pos			0.004	0.007	0.007		0.005			0.006
Combined error total			0.008	0.010	0.010		0.010			0.013

Table C.3: Summary of error contributions to individual $\mathcal{L}_{\mathrm{eff},\,^{83m}\mathrm{Kr}}$ measurements at $\mathcal{E}_{\mathrm{d}} = 200\,\mathrm{V/cm}$. The combined error for each measurement is shown Fig. 8.4.

Recoil Energy [keV]	10.3	14.8	16.9	20.5	25.4	28.7	36.1	40.1	49.7	57.2
$\mathcal{L}_{\text{eff},\,^{83m}\text{Kr}}$	0.184	0.203	0.188	0.218	0.209	0.237	0.250	0.277	0.267	0.272
Statistical error	0.004	0.004	0.005	0.002	0.006	0.001	0.005	0.005	0.001	0.005
Systematic error source										
Fit method	0.000	0.002	0.002	0.003	0.000	0.005	0.008	0.005	0.003	0.003
Fit range	0.009	0.002	0.002	0.001	0.005	0.001	0.009	0.000	0.000	0.001
TPC tof	0.002	0.002	0.005	0.001	0.003	0.002	0.001	0.004	0.002	0.001
N tof	0.003	0.002	0.003	0.002	0.001	0.002	0.003	0.002	0.002	0.001
f90	0.003	0.002	0.001	0.001	0.000	0.000	0.000	0.000	0.000	0.000
Kr LY	0.004	0.004	0.004	0.004	0.004	0.005	0.005	0.006	0.005	0.005
Recoil energy										
TPC pos	0.001	0.001	0.001	0.001	0.001	0.001	0.001	0.001	0.001	0.001
EJ pos	0.006	0.008	0.004	0.007	0.006	0.005	0.005	0.008	0.003	0.005
Combined error total	0.013	0.011	0.010	0.009	0.011	0.009	0.016	0.013	0.007	0.010

Table C.4: Summary of error contributions to individual $\mathcal{L}_{\text{eff},\,^{83m}\text{Kr}}$ measurements at $\mathcal{E}_{\text{d}} = 300\,\text{V/cm}$. The combined error for each measurement is shown Fig. 8.4.

| Recoil Energy [keV]	10.3	14.8	16.9	20.5	25.4	28.7	36.1	40.1	49.7	57.2
$\mathcal{L}_{\text{eff},\,^{83m}\text{Kr}}$			0.174		0.209		0.234			0.267
Statistical error			0.001		0.008		0.007			0.006
Systematic error source										
Fit method			0.004		0.000		0.001			0.005
Fit range			0.003		0.004		0.002			0.000
TPC tof			0.001		0.001		0.002			0.002
N tof			0.001		0.001		0.001			0.005
f90			0.002		0.000		0.000			0.001
Kr LY			0.003		0.004		0.005			0.005
Recoil energy										
TPC pos			0.001		0.001		0.001			0.001
EJ pos			0.003		0.006		0.005			0.005
Combined error total			0.008		0.012		0.010			0.012

Table C.5: Summary of error contributions to individual $\mathcal{L}_{\text{eff},\,^{83m}\text{Kr}}$ measurements at $\mathcal{E}_{\text{d}} = 500\,\text{V/cm}$.

Recoil Energy [keV]	10.3	14.8	16.9	20.5	25.4	28.7	36.1	40.1	49.7	57.2
$\mathcal{L}_{\mathrm{eff},\,^{83\mathrm{m}}\mathrm{Kr}}$	0.160	0.169		0.188	0.194	0.203	0.228	0.256	0.248	0.243
Statistical error	0.003	0.002		0.001	0.007	0.005	0.005	0.003	0.007	0.002
Systematic error source										
Fit method	0.004	0.002		0.002	0.000	0.003	0.002	0.010	0.002	0.001
Fit range	0.004	0.003		0.001	0.009	0.001	0.002	0.000	0.001	0.001
TPC tof	0.004	0.003		0.001	0.001	0.002	0.003	0.002	0.002	0.004
N tof	0.002	0.002		0.001	0.002	0.001	0.006	0.002	0.002	0.002
f90	0.004	0.003		0.001	0.000	0.001	0.001	0.001	0.002	0.002
Kr LY	0.003	0.003		0.004	0.004	0.004	0.005	0.005	0.005	0.005
Recoil energy										
TPC pos	0.001	0.001		0.001	0.001	0.001	0.001	0.001	0.001	0.001
EJ pos	0.005	0.007		0.006	0.006	0.004	0.005	0.008	0.002	0.005
Combined error total	0.011	0.010		0.008	0.013	0.009	0.011	0.014	0.010	0.009

Table C.6: Summary of error contributions to individual $\mathcal{L}_{\mathrm{eff},\,^{83\mathrm{m}}\mathrm{Kr}}$ measurements at $\mathcal{E}_{\mathrm{d}} = 1000\,\mathrm{V/cm}$. The combined error for each measurement is shown Fig. 8.4.

Appendix D

Comparison between f_{90} distribution with "ratio-of-Gaussians" model

D.1 Comparison of nuclear recoil (NR) f_{90} distribution with "ratio-of-Gaussians" model

The NR f_{90} distribution for each configuration is extracted from SCENE data with the steps described in Sec. 8.5. All the parameters in the "ratio-of-Gaussians" model are also fixed according to the procedure described in that section. The poisson statistics, the SER width and the TPB wavelength shifting statistics are included in the variances σ_p^2 and σ_l^2. The χ^2 is computed with the standard fit routine of ROOT to show the goodness of the agreement between the data and the model, despite none of the fit parameter is free.
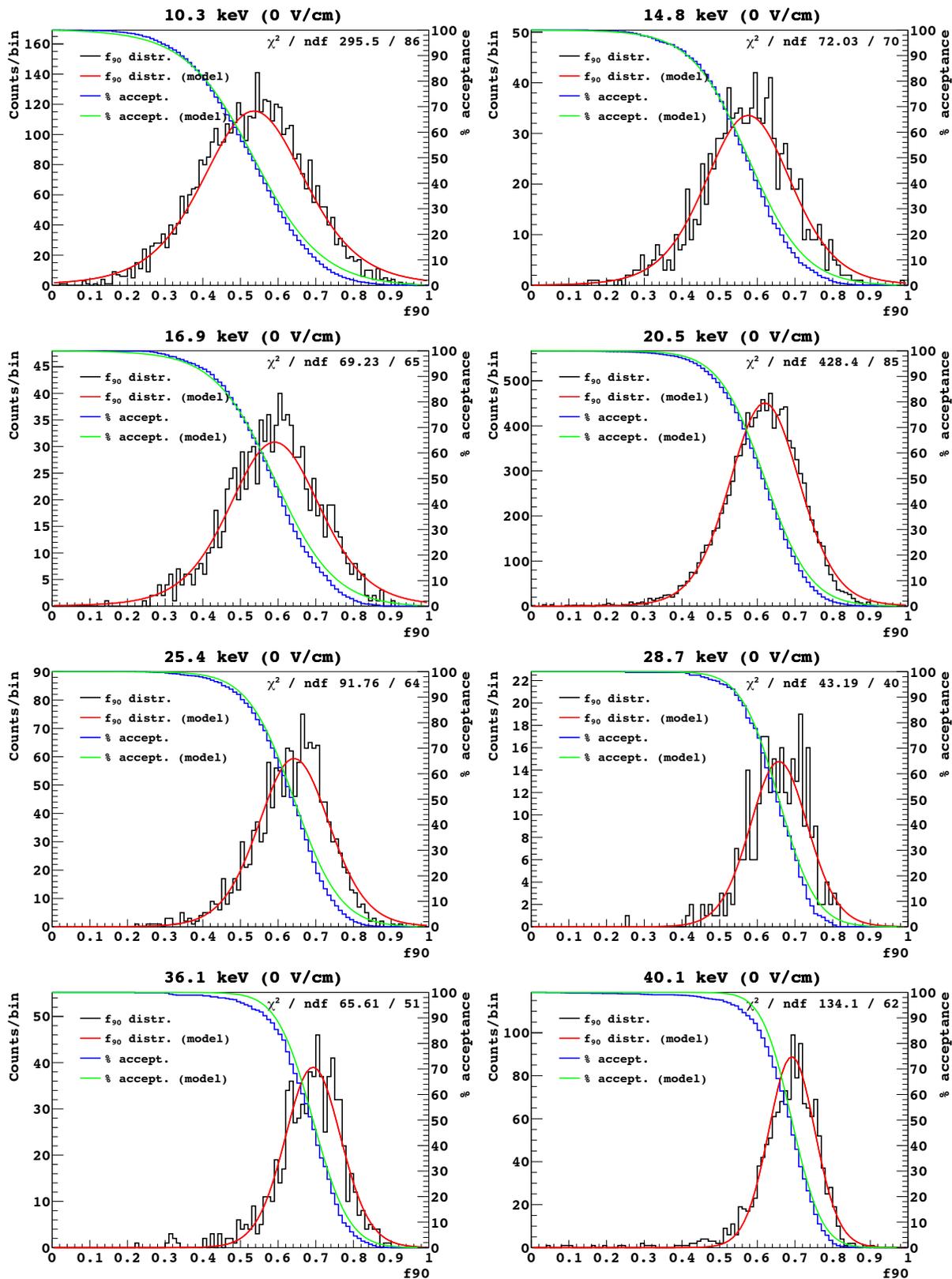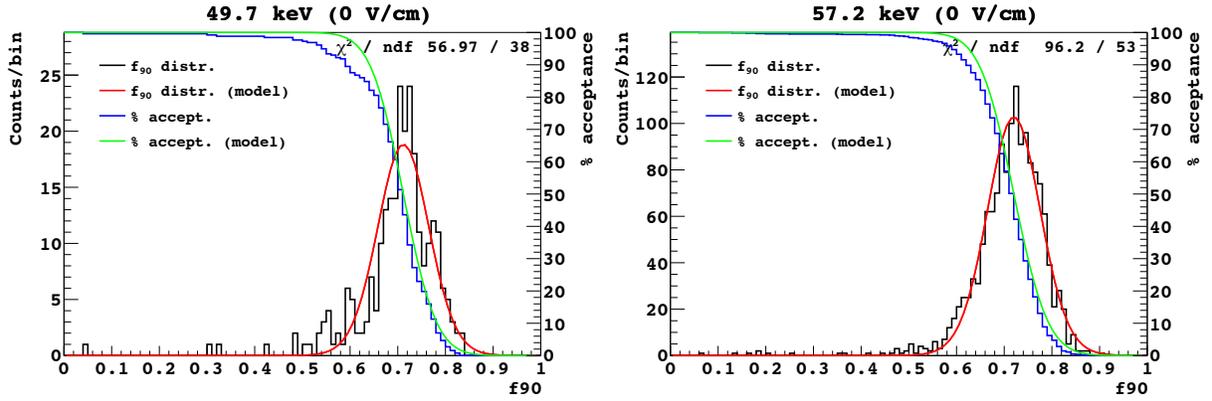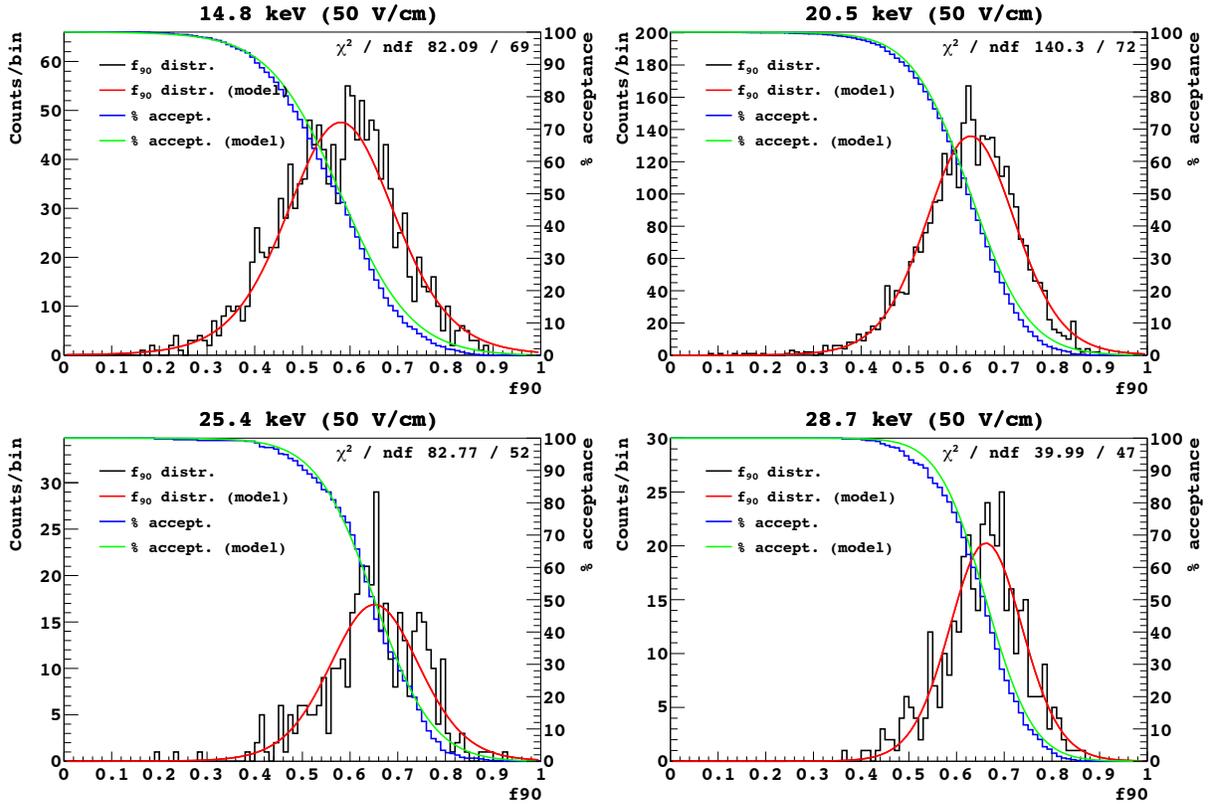
Figure D.1: NR f_{90} distribution at $\mathcal{E}_d = 0\,\mathrm{V/cm}$ compared with the model.
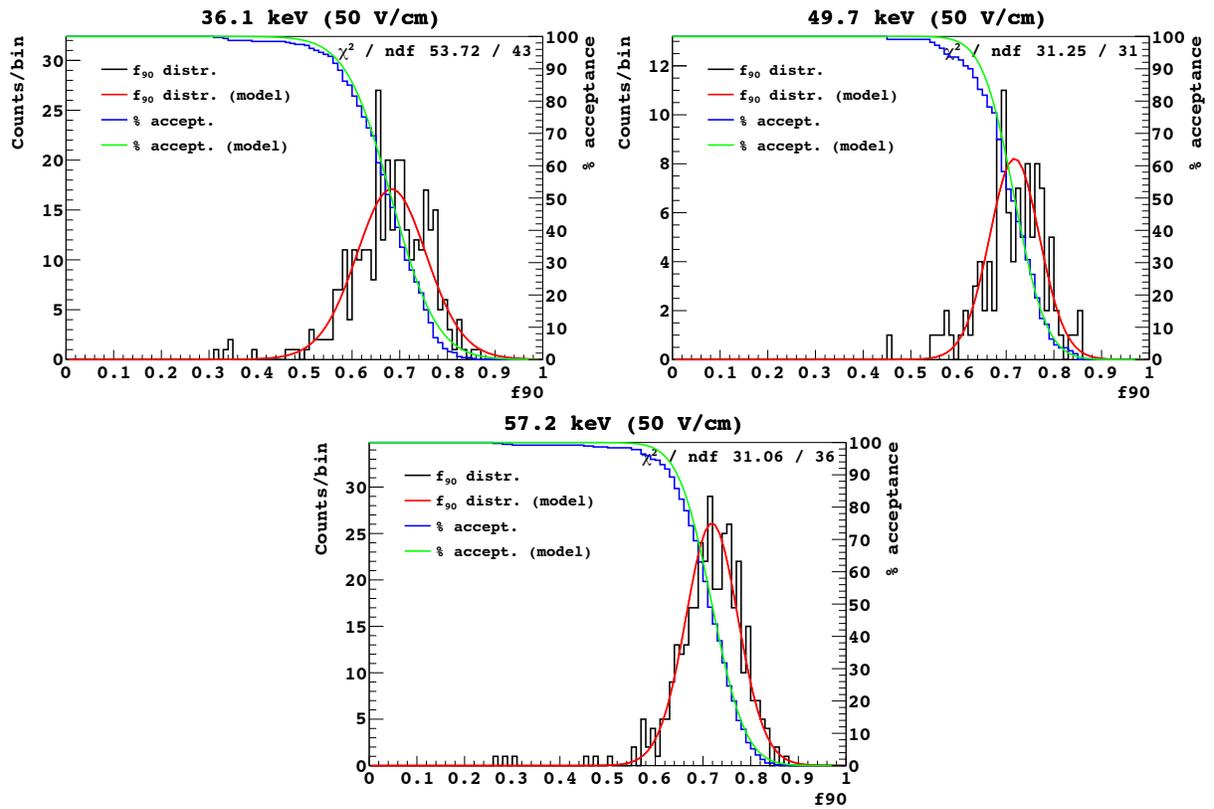
Figure D.2: NR f_{90} distribution at $\mathcal{E}_d = 50\,\text{V/cm}$ compared with the model.

Figure D.3: NR f_{90} distribution at $\mathcal{E}_d = 100\,\mathrm{V/cm}$ compared with the model.
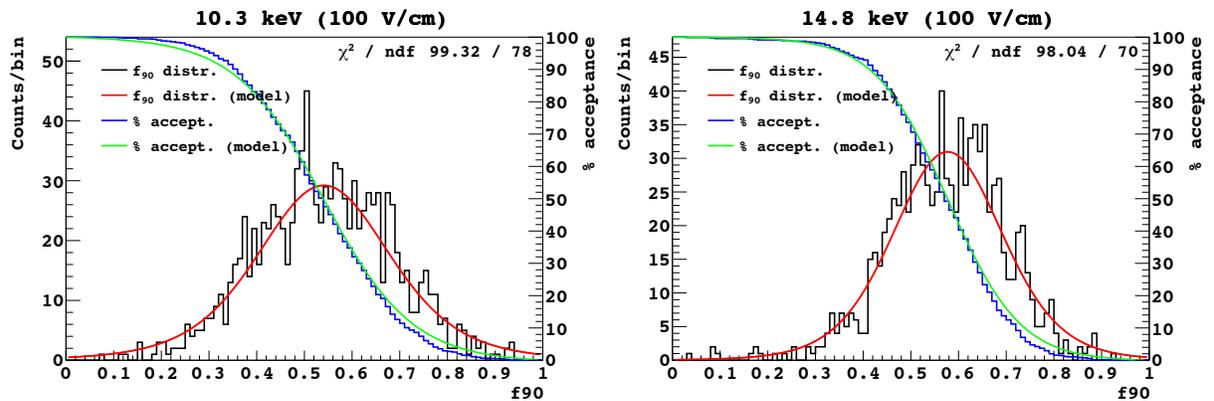
Figure D.4: NR f_{90} distribution at $\mathcal{E}_d = 200\,\text{V/cm}$ compared with the model.
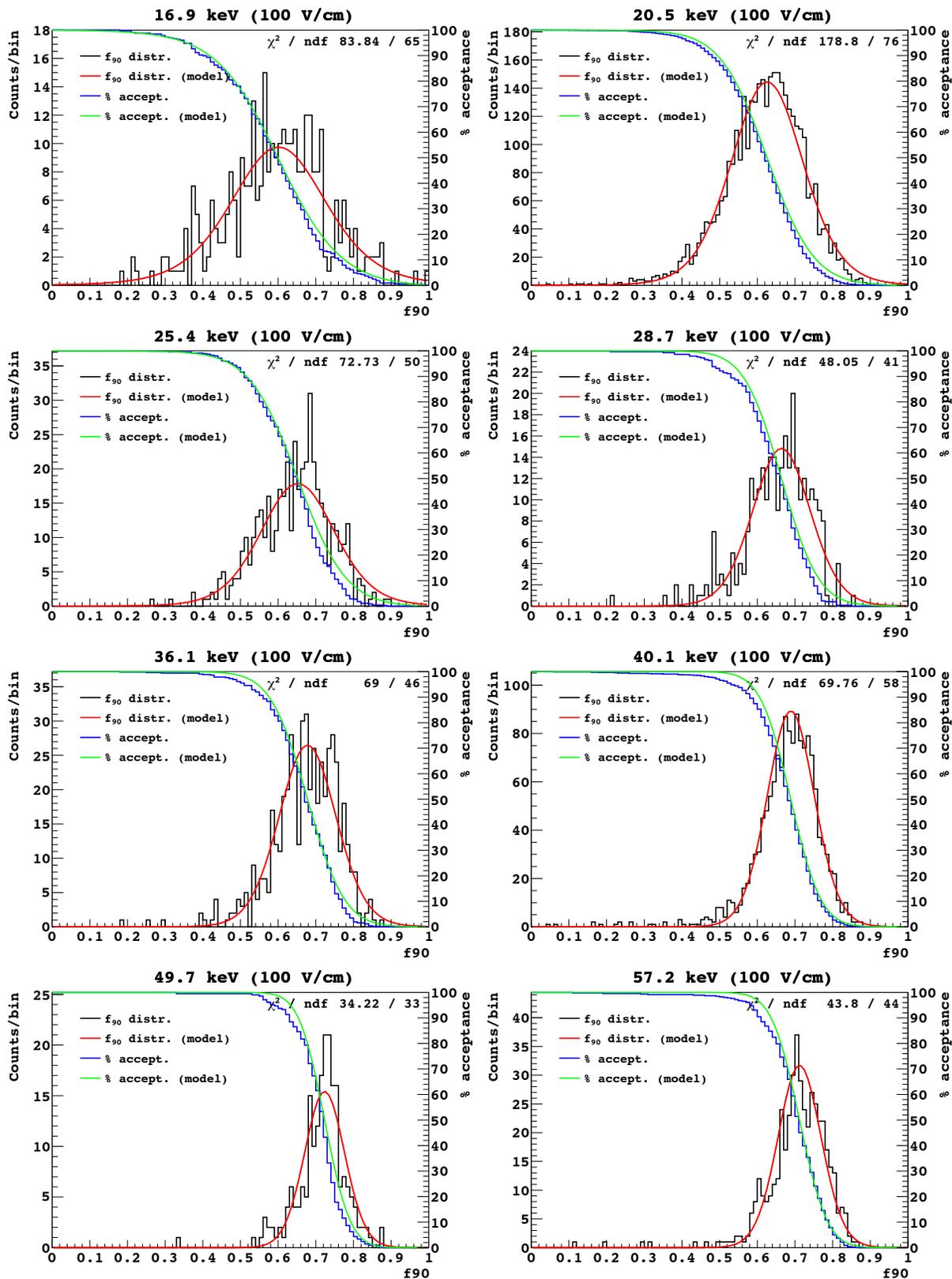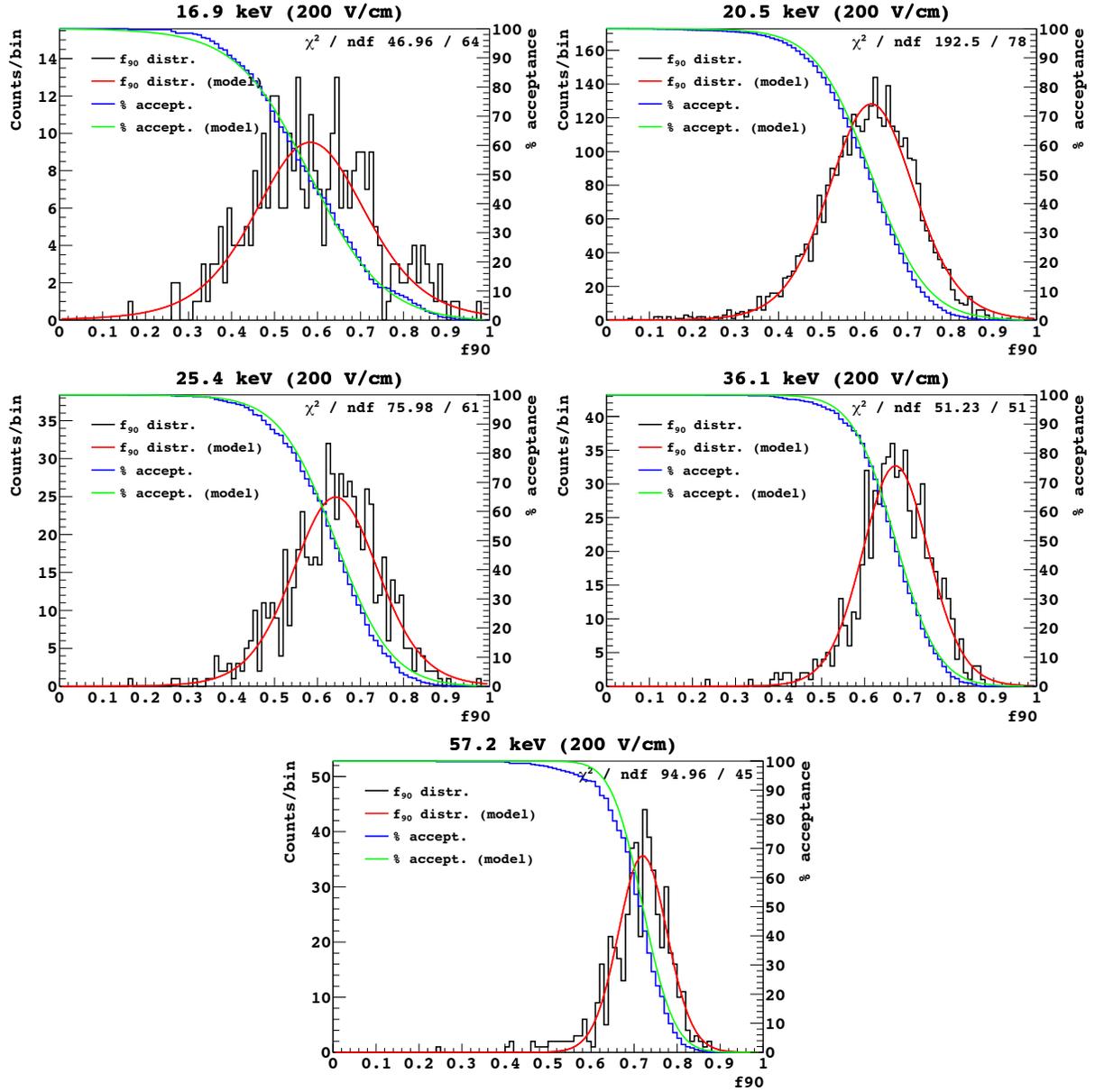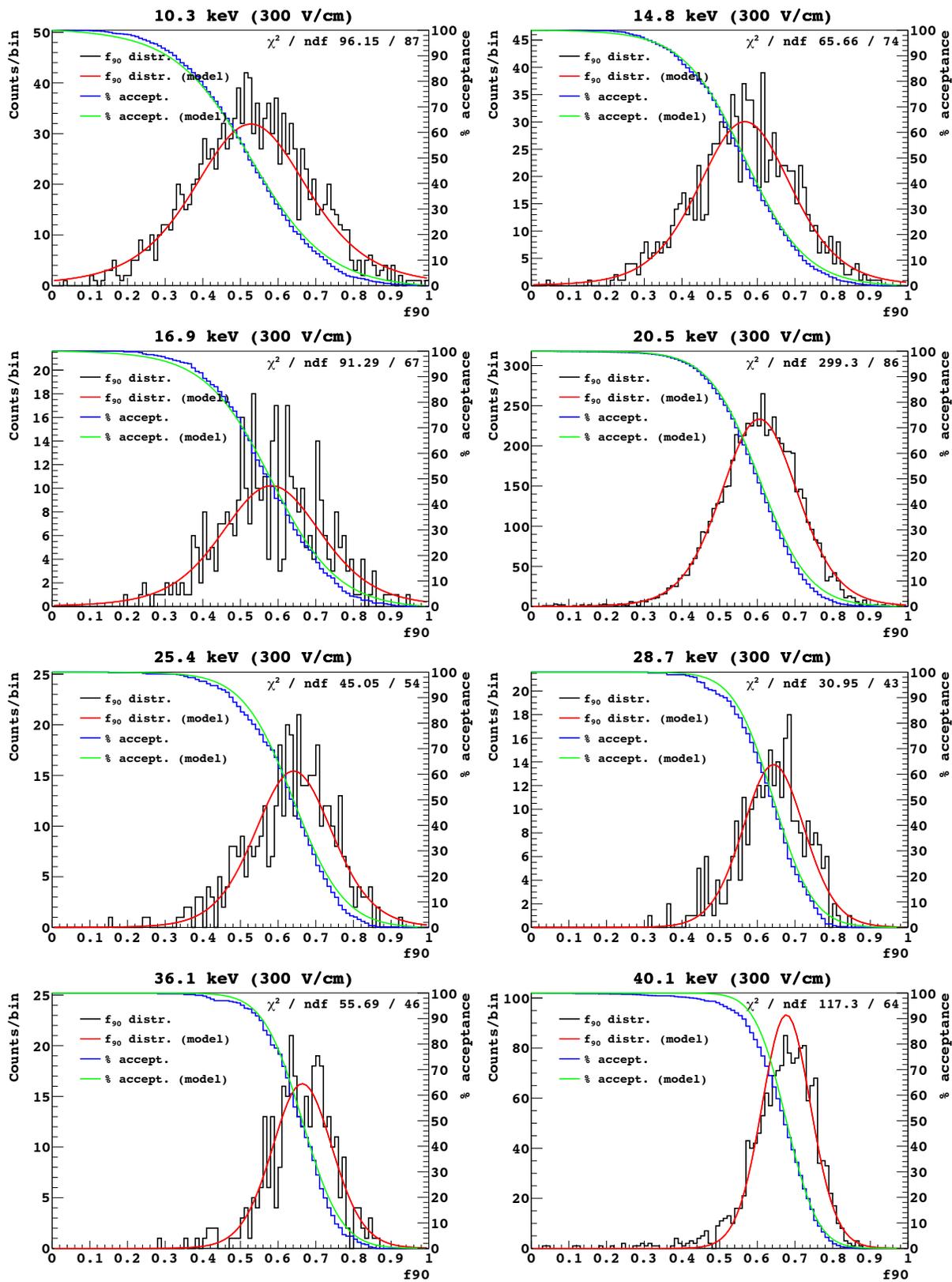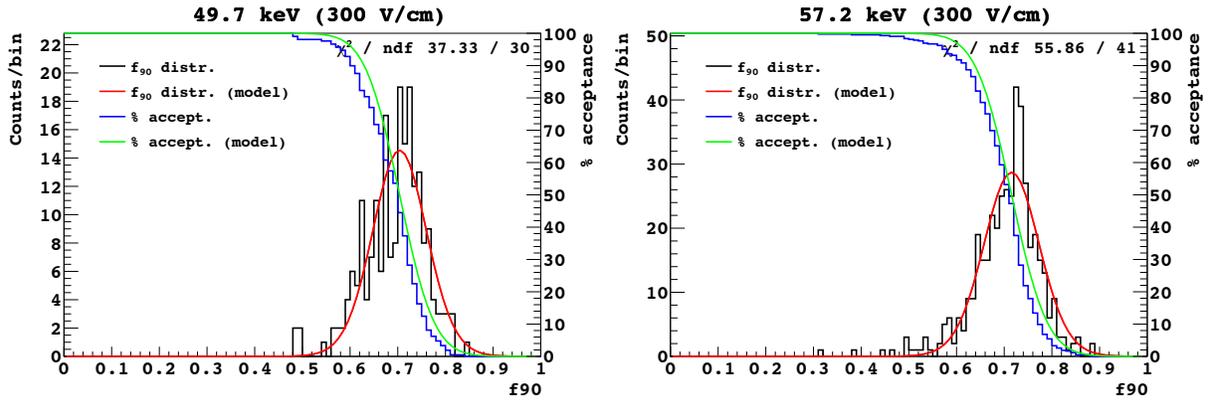
Figure D.5: NR f_{90} distribution at $\mathcal{E}_d = 300\,\text{V/cm}$ compared with the model.
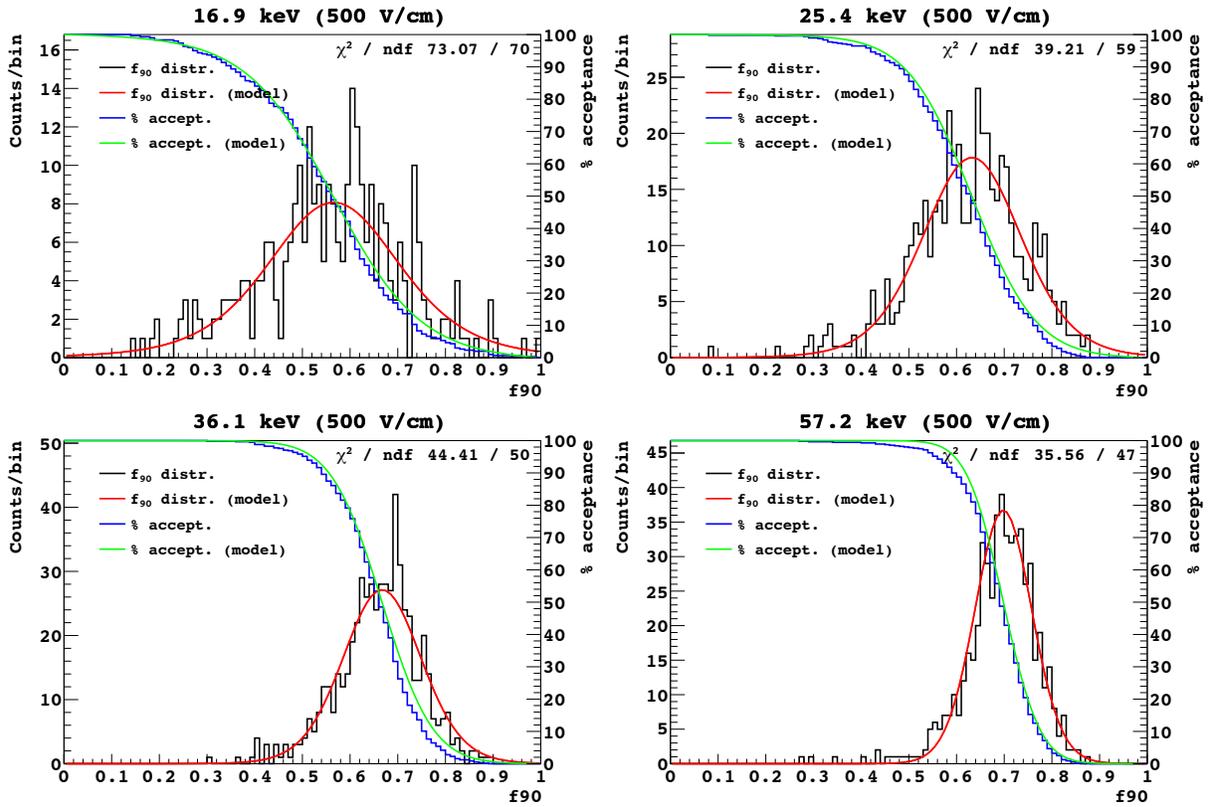
Figure D.6: NR f_{90} distribution at $\mathcal{E}_d = 500\,\text{V/cm}$ compared with the model.

124

The figures show f_{90} distribution plots at eight energies (10.3 keV, 14.8 keV, 20.5 keV, 25.4 keV, 28.7 keV, 36.1 keV, 40.1 keV, 49.7 keV), all at 1000 V/cm.
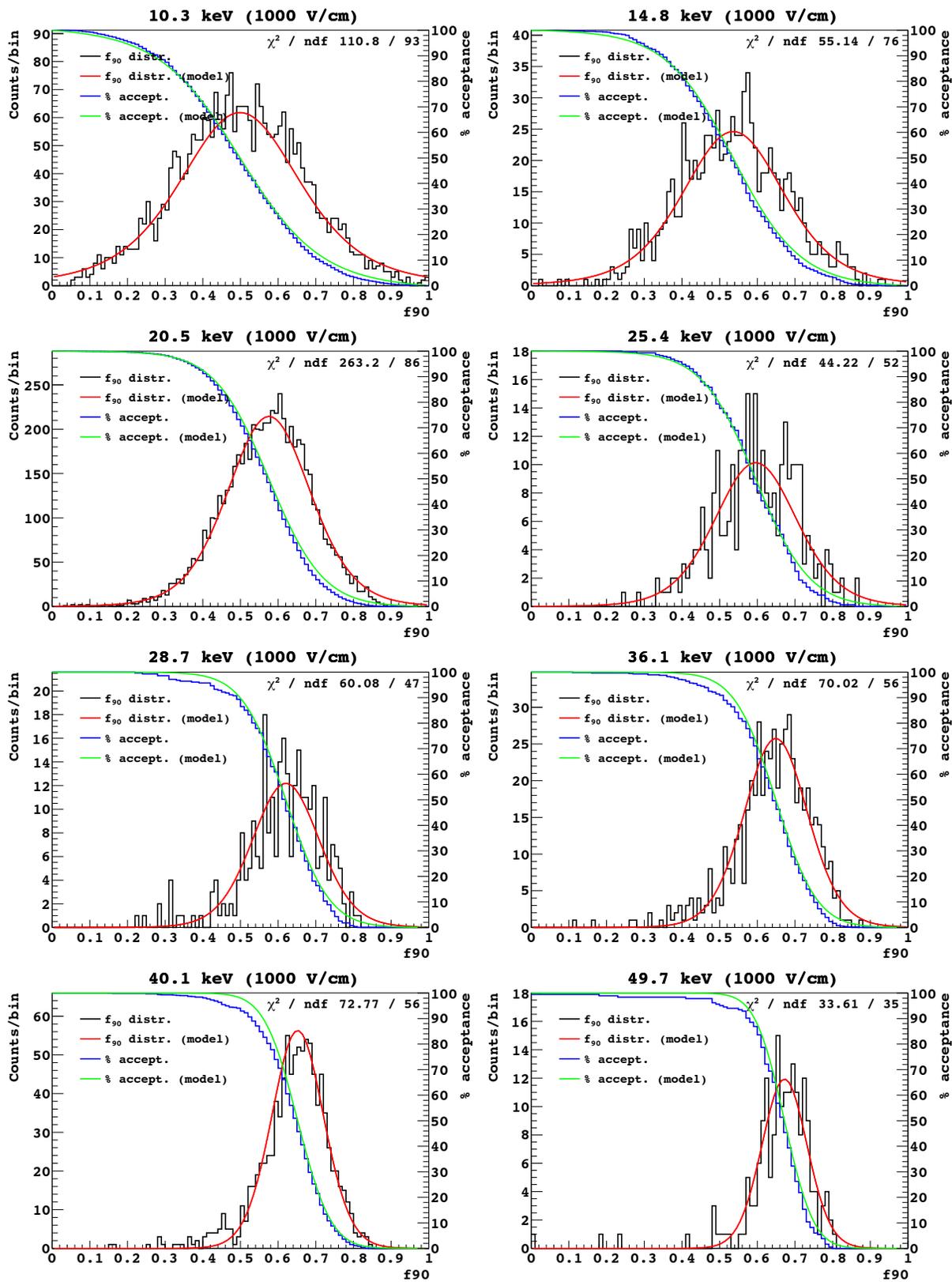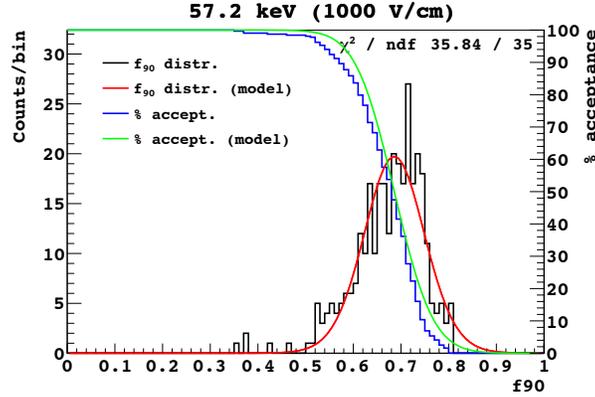
Figure D.7: NR f_{90} distribution at $\mathcal{E}_d = 1000\,\text{V/cm}$ compared with the model.

D.2 Comparison of γ-ray induced electron recoils (ER) f_{90} distribution with "ratio-of-Gaussians" model

For the purpose of comparing with data acquired in DarkSide-50 experiment, I show the ER f_{90} distributions acquired in the SCENE LAr detector at $\mathcal{E}_d = 200\,\text{V/cm}$. The ER events are selected with a time-of-flight cut that corresponds to the γ-rays. The ER data are divided into bins with fixed width in NPE. The corresponding NPE bins in DarkSide-50 (where the null field light yield of ^{83m}Kr is $(7.91 \pm 0.24\,\text{PE/keV})$ are also listed on the title of each plot.

We compare the SCENE ER f_{90} distributions with the "ratio-of-Gaussians" model. The parameters in the "ratio-of-Gaussians" model, like the NR case in the previous section, are fixed according to the procedure described in Sec. 8.5. $\sigma_{n,l}^2$ and $\sigma_{n,p}^2$ are negligible compared to the other variance terms. The χ^2 is computed with the standard fit routine of ROOT to show the goodness of the agreement between the data and the model. All parameters in the model are fixed.

A comparison of the f_{90} means and medians for ERs at $200\,\text{V/cm}$ drift field extracted from SCENE, DarkSide-50, and Ref. [98] is shown in Fig. D.9. f_{90} medians for NRs extracted from SCENE are also shown.

Bin: 49-57 PE (60-70 PE_DS)
χ^2 / ndf 48.36 / 48

Bin: 57-65 PE (70-80 PE_DS)
χ^2 / ndf 40.92 / 46

Bin: 65-73 PE (80-90 PE_DS)
χ^2 / ndf 42.14 / 43

Bin: 73-81 PE (90-100 PE_DS)
χ^2 / ndf 32.68 / 40

Bin: 81-89 PE (100-110 PE_DS)
χ^2 / ndf 42.93 / 40

Bin: 89-97 PE (110-120 PE_DS)
χ^2 / ndf 28.72 / 35

Bin: 97-105 PE (120-130 PE_DS)
χ^2 / ndf 43.82 / 37

Bin: 105-113 PE (130-140 PE_DS)
χ^2 / ndf 32.27 / 34

Bin: 113-121 PE (140-150 PE_DS)
χ^2 / ndf 26.34 / 32

Bin: 121-129 PE (150-160 PE_DS)
χ^2 / ndf 26.9 / 34
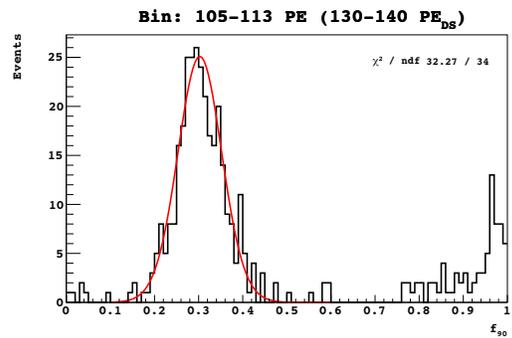
127

Figure D.8: ER f_{90} distribution at $\mathcal{E}_d = 200\,\mathrm{V/cm}$ compared with the model.
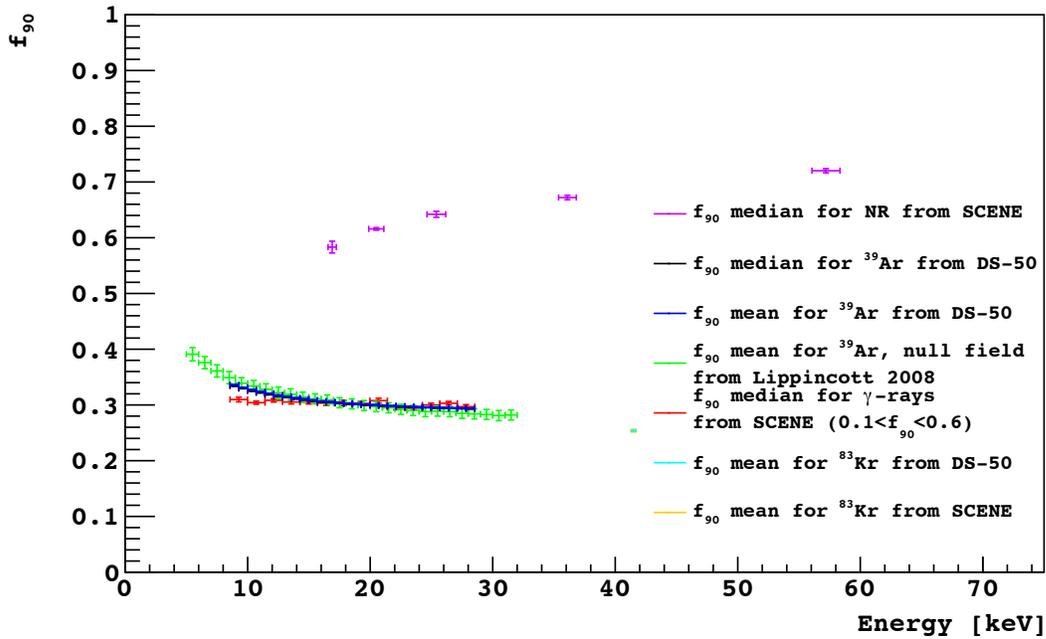
Figure D.9: Comparison of f_{90} medians and means at $\mathcal{E}_d = 200\,\mathrm{V/cm}$ in SCENE, DarkSide-50, and MicroCLEAN.

D.3 Comparison between DarkSide-50 ER $\mathtt{f}_{90}$ distribution and the "ratio-of-Gaussians" model with input from SCENE
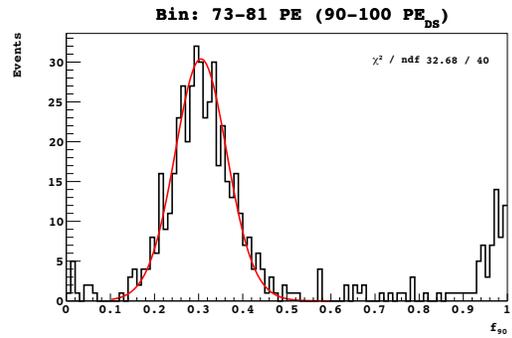
To justify the use of SCENE NR $\mathtt{f}_{90}$ median and the "ratio-of-Gaussians" model in drawing the acceptance curves in a LAr WIMP detector such as DarkSide-50, we test the procedure with ER. We take the ER $\mathtt{f}_{90}$ median of each S1 bin from SCENE as f_p and the center of the corresponding S1 bin in DarkSide-50 as μ. We fix the SER width σ_{SPE} to the observed value of 0.4, σ^2_{TPB} to 0.22, and noise terms $\sigma^2_{n,l}$ and $\sigma^2_{n,p}$ to models derived from DarkSide-50. The results are shown in Fig. D.10.
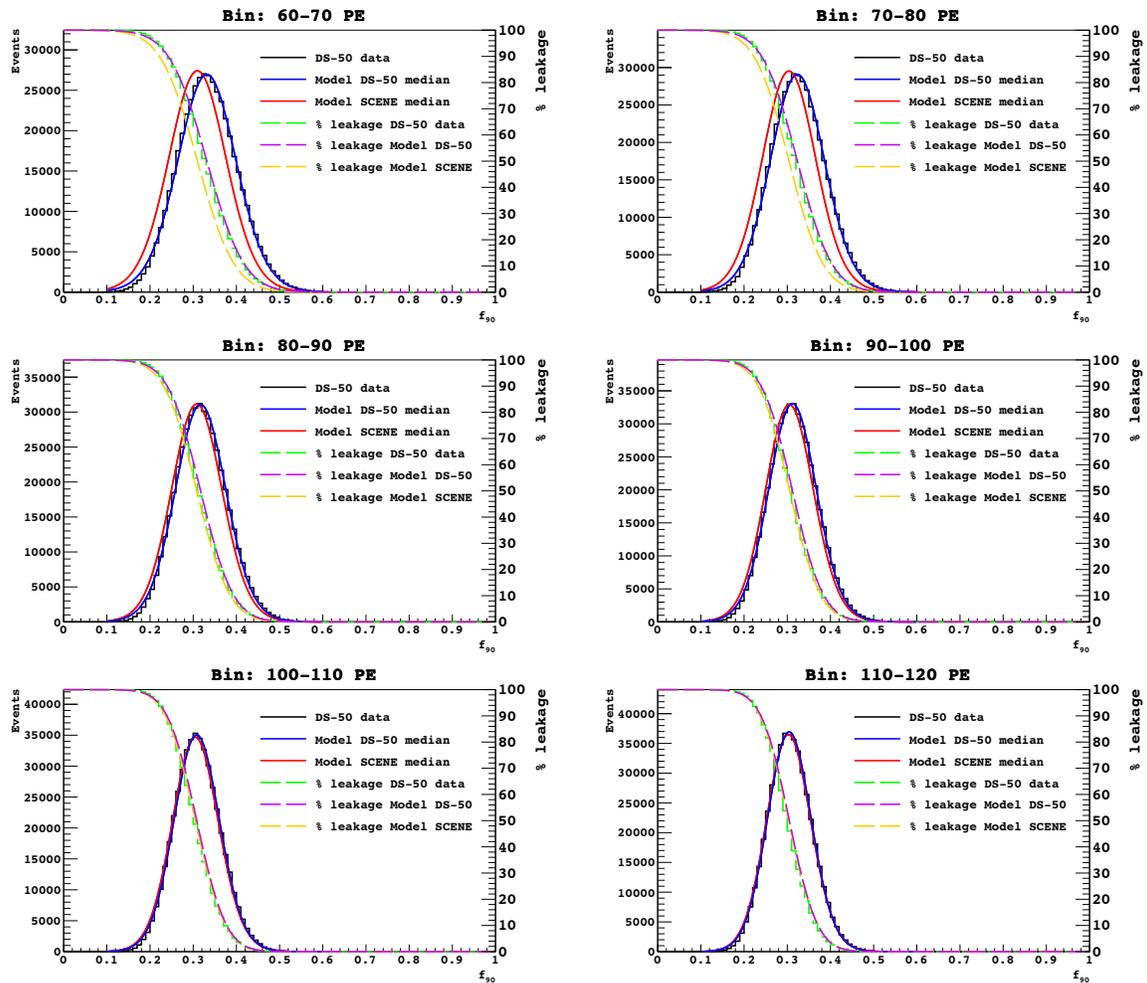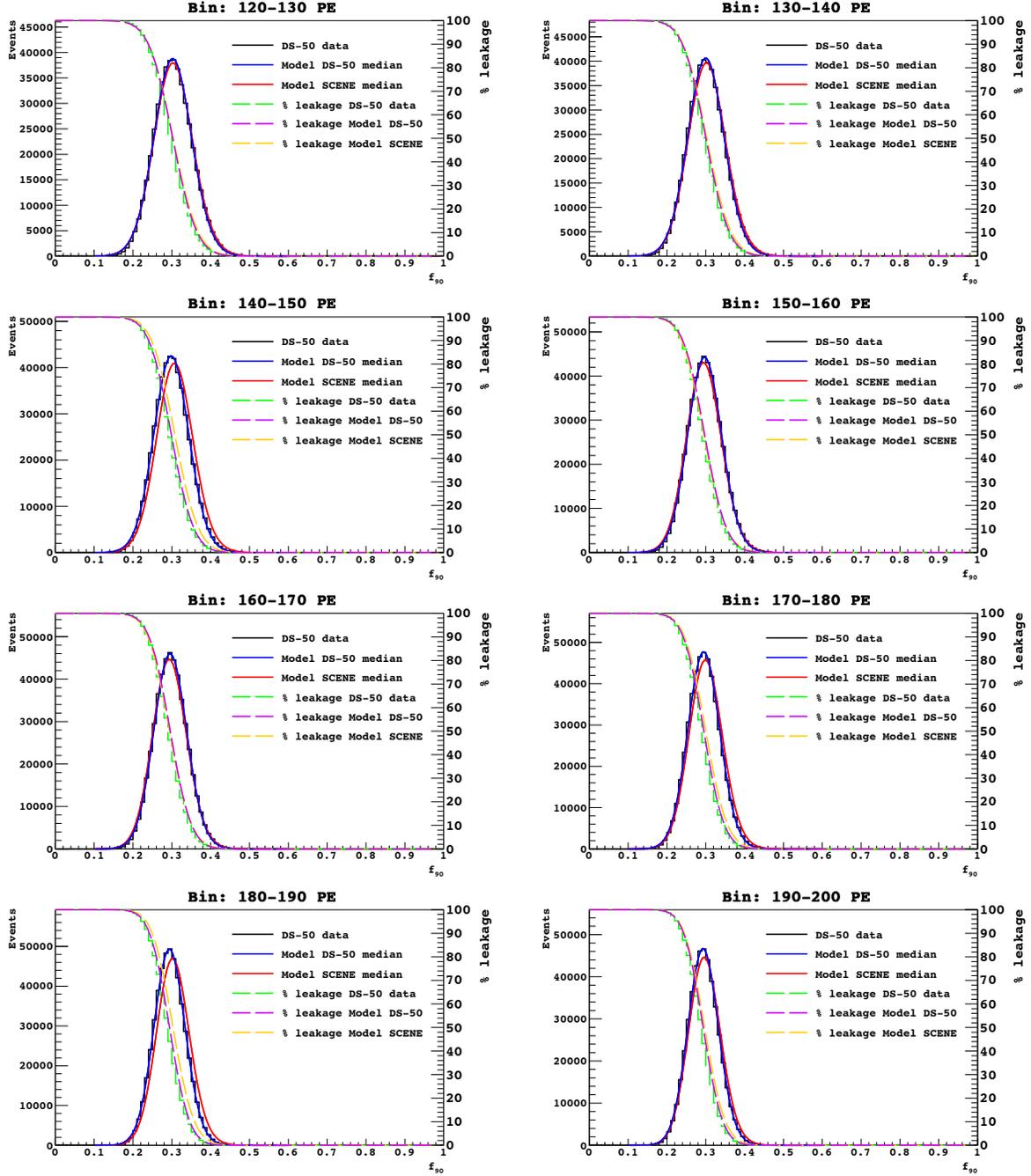
Figure D.10: DarkSide-50 ER f_{90} distribution at $\mathcal{E}_d = 200\,\mathrm{V/cm}$ compared with the model. **Blue curve:** f_p is fixed to DarkSide-50 f_{90} median. **Red curve:** f_p is fixed to SCENE f_{90} median.

Appendix E

Fits to S2 spectra
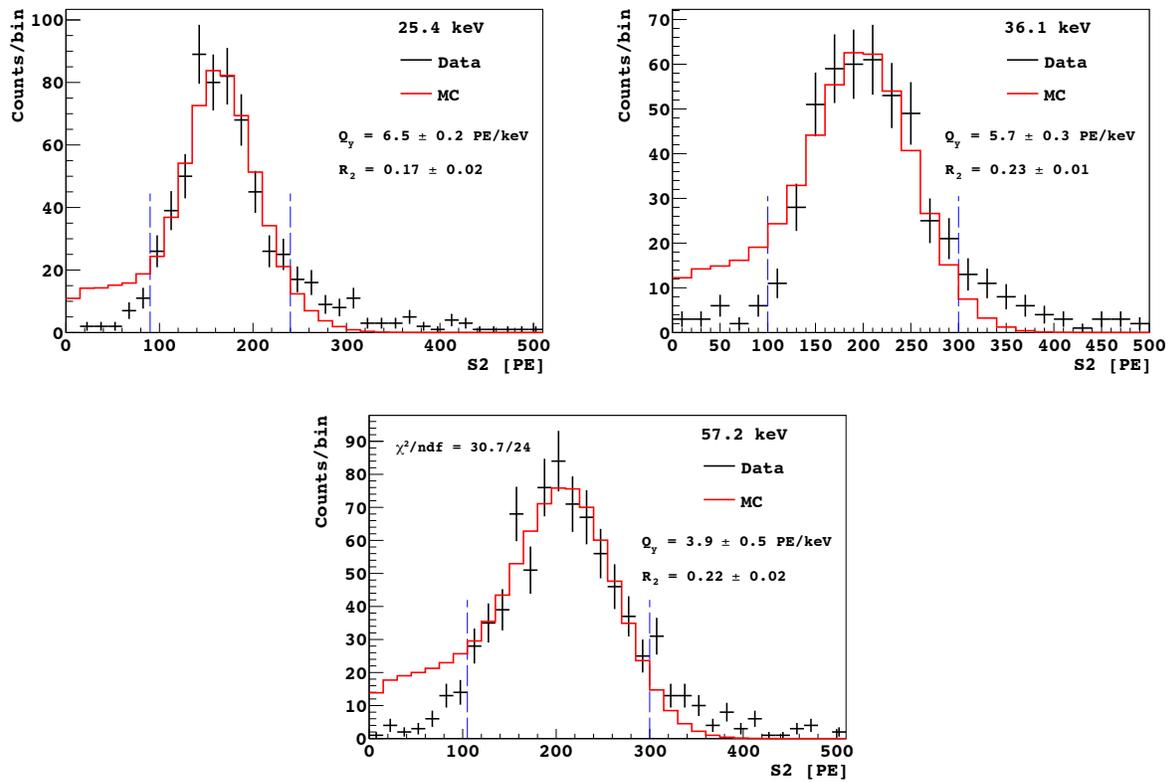
Figure E.1: **Black:** experimental data collected with $\mathcal{E}_{\mathrm{d}} = 50\,\mathrm{V/cm}$. **Red:** Monte Carlo fit of the experimental data. The range used for each fit is indicated by the vertical **blue** dashed lines. The χ^2 (sum across all spectra as defined in text) and total number of degrees of freedom are shown in the last panel.
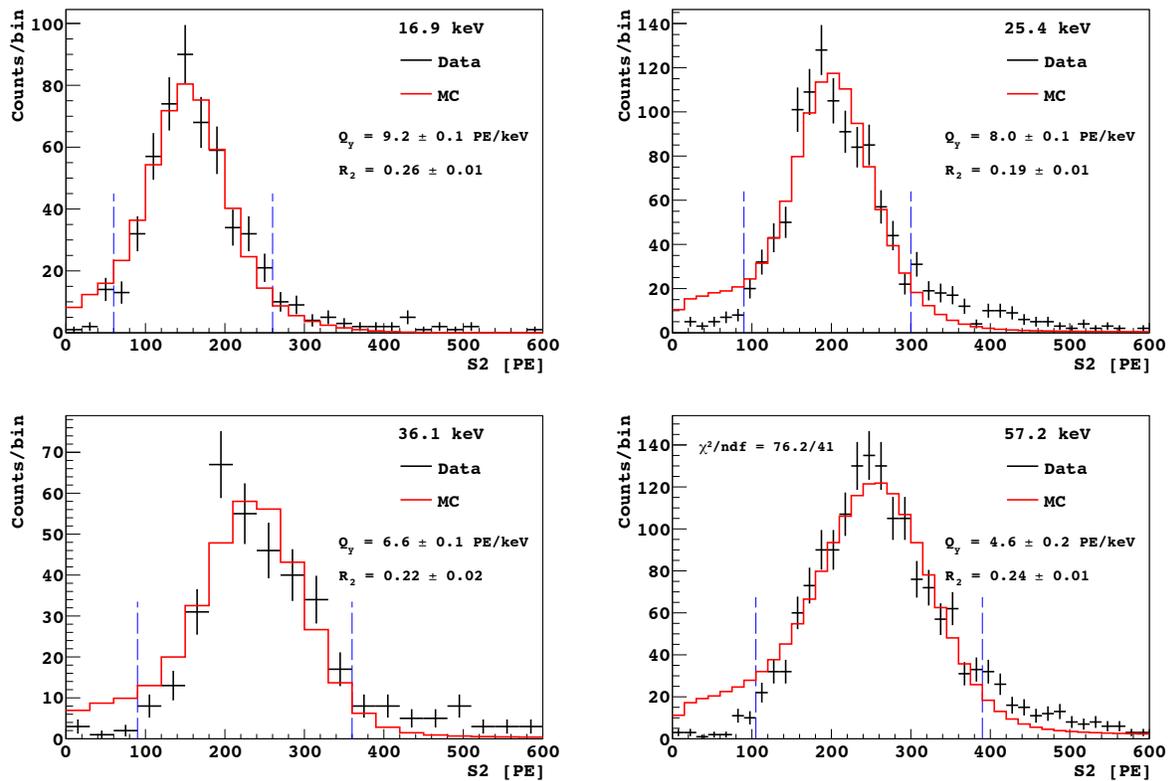
Figure E.2: **Black:** experimental data collected with $\mathcal{E}_d = 100\,\mathrm{V/cm}$. **Red:** Monte Carlo fit of the experimental data. The range used for each fit is indicated by the vertical **blue** dashed lines. The χ^2 (sum across all spectra as defined in the text) and the total number of degrees of freedom are shown in the last panel.
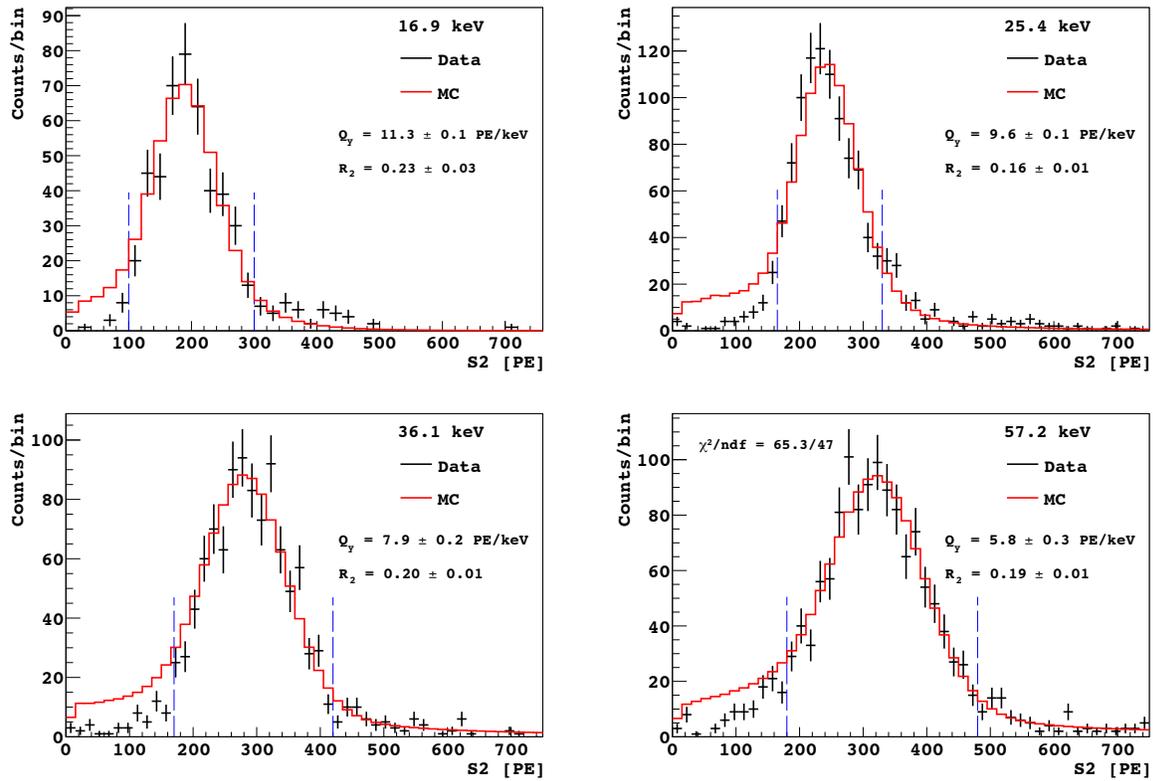
Figure E.3: **Black:** experimental data collected with $\mathcal{E}_\mathrm{d} = 200\,\mathrm{V/cm}$. **Red:** Monte Carlo fit of the experimental data. The range used for each fit is indicated by the vertical **blue** dashed lines. The χ^2 (sum across all spectra as defined in the text) and the total number of degrees of freedom are shown in the last panel.
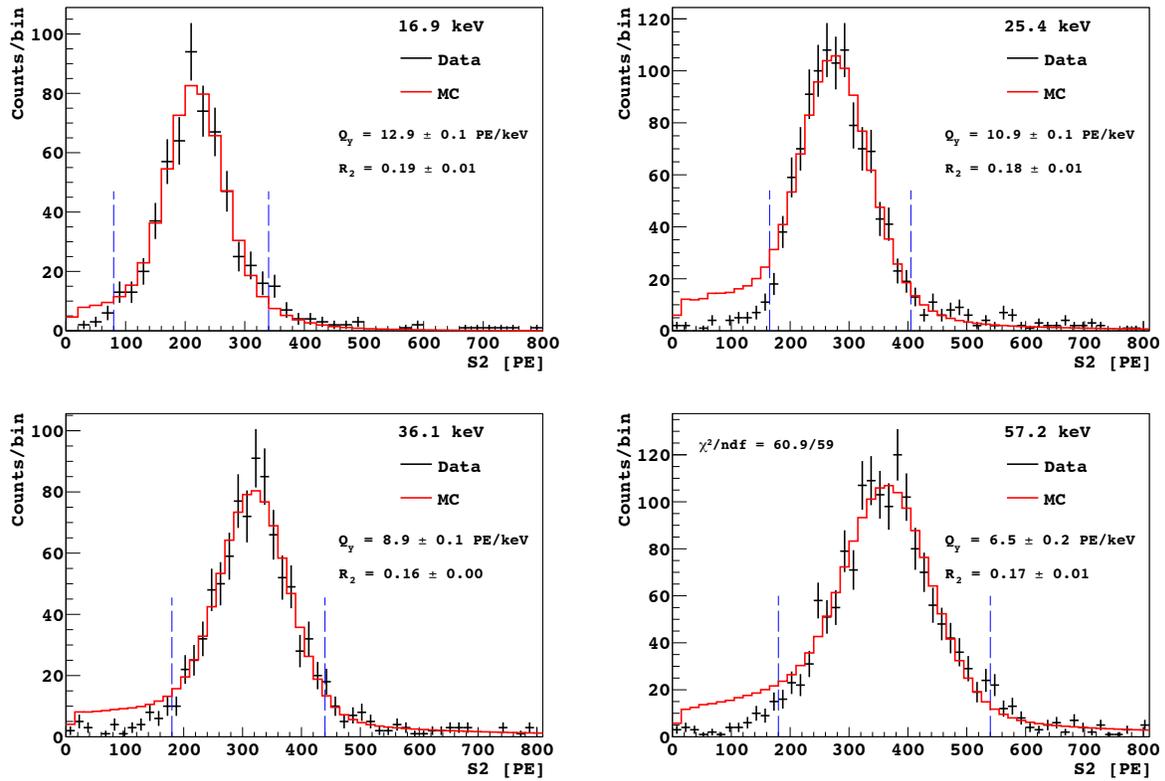
Figure E.4: **Black:** experimental data collected with $\mathcal{E}_\mathrm{d} = 300\,\mathrm{V/cm}$. **Red:** Monte Carlo fit of the experimental data. The range used for each fit is indicated by the vertical **blue** dashed lines. The χ^2 (sum across all spectra as defined in the text) and the total number of degrees of freedom are shown in the last panel.
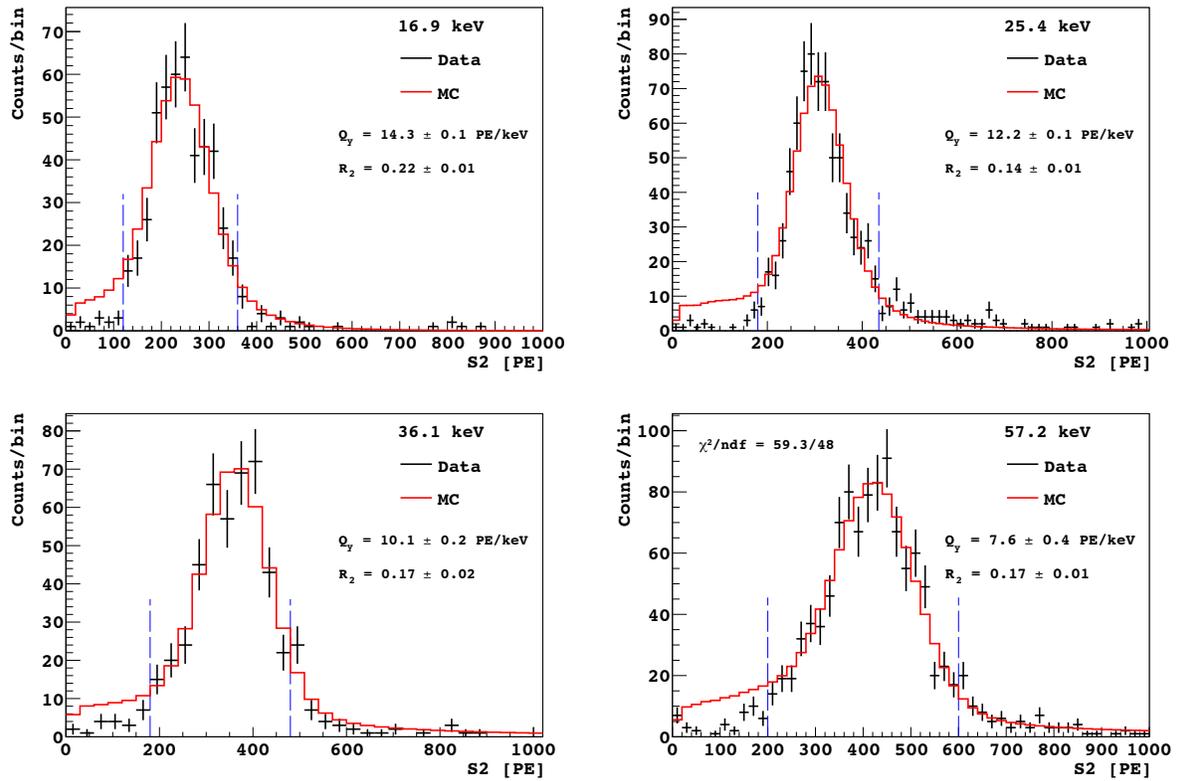
Figure E.5: **Black:** experimental data collected with $\mathcal{E}_\mathrm{d} = 500\,\mathrm{V/cm}$. **Red:** Monte Carlo fit of the experimental data. The range used for each fit is indicated by the vertical **blue** dashed lines. The χ^2 (sum across all spectra as defined in the text) and the total number of degrees of freedom are shown in the last panel.

Appendix F

Tables of $\mathcal{Q}_\mathrm{y}$ at drift fields other than 200 V/cm

Recoil Energy [keV]	16.9	25.4	36.1	57.2
$\mathcal{Q}_\mathrm{y}$ [PE/keV]		6.5	5.7	3.9
Statistical error		0.2	0.3	0.5
Systematic errors				
Fit method		0.2	0.0	0.3
Fit range		0.0	0.1	0.1
TPC tof		0.1	0.3	0.1
N tof		0.1	0.1	0.1
f90		0.2	0.3	0.1
Kr LY		0.1	0.1	0.1
Recoil energy				
TPC pos		0.0	0.0	0.0
EJ pos		0.2	0.1	0.1
Combined error total		0.5	0.5	0.6

Table F.1: Summary of error contributions to individual $\mathcal{Q}_\mathrm{y}$ measurements at $\mathcal{E}_\mathrm{d} = 50\,\mathrm{V/cm}$. The combined error for each measurement is shown Fig. 8.10.

Recoil Energy [keV]	16.9	25.4	36.1	57.2
$\mathcal{Q}_y$ [PE/keV]	9.2	8.0	6.6	4.6
Statistical error	0.1	0.1	0.1	0.2
Systematic errors				
Fit method	0.0	0.1	0.3	0.3
Fit range	0.0	0.0	0.0	0.0
TPC tof	0.1	0.1	0.1	0.1
N tof	0.1	0.1	0.1	0.2
f90	0.2	0.2	0.1	0.2
Kr LY	0.2	0.2	0.1	0.1
Recoil energy				
TPC pos	0.1	0.0	0.0	0.0
EJ pos	0.2	0.2	0.1	0.1
Combined error total	0.4	0.4	0.4	0.4

Table F.2: Summary of error contributions to individual $\mathcal{Q}_y$ measurements at $\mathcal{E}_d = 100\,\mathrm{V/cm}$. The combined error for each measurement is shown Fig. 8.10.

Recoil Energy [keV]	16.9	25.4	36.1	57.2
$\mathcal{Q}_y$ [PE/keV]	12.9	10.9	8.9	6.5
Statistical error	0.1	0.1	0.1	0.2
Systematic errors				
Fit method	0.1	0.1	0.1	0.3
Fit range	0.3	0.0	0.2	0.0
TPC tof	0.2	0.1	0.1	0.0
N tof	0.2	0.2	0.1	0.0
f90	0.1	0.1	0.1	0.0
Kr LY	0.3	0.2	0.2	0.1
Recoil energy				
TPC pos	0.1	0.0	0.0	0.0
EJ pos	0.3	0.3	0.2	0.1
Combined error total	0.6	0.5	0.4	0.4

Table F.3: Summary of error contributions to individual $\mathcal{Q}_y$ measurements at $\mathcal{E}_d = 300\,\mathrm{V/cm}$. The combined error for each measurement is shown Fig. 8.10.

Recoil Energy [keV]	16.9	25.4	36.1	57.2
$\mathcal{Q}_y$ [PE/keV]	14.3	12.2	10.1	7.6
Statistical error	0.1	0.1	0.2	0.4
Systematic errors				
Fit method	0.0	0.3	0.0	0.3
Fit range	0.3	0.1	0.0	0.0
TPC tof	0.1	0.1	0.1	0.1
N tof	0.0	0.0	0.0	0.2
f90	0.1	0.0	0.0	0.0
Kr LY	0.3	0.2	0.2	0.2
Recoil energy				
TPC pos	0.1	0.0	0.0	0.0
EJ pos	0.3	0.4	0.2	0.2
Combined error total	0.5	0.6	0.4	0.6

Table F.4: Summary of error contributions to individual $\mathcal{Q}_y$ measurements at $\mathcal{E}_d = 500\,\mathrm{V/cm}$. The combined error for each measurement is shown Fig. 8.10.

Appendix G

Wavelength shifter coating on ITO

This chapter describes the procedure I have tested for preparing the indium tin oxide (ITO) coated windows before the wavelength shifter coating.

A common procedure to coat the surfaces of the sensitive volume in a LAr scintillation detector with wavelength shifter such as TetraPhenylButadiene (TPB) is vacuum evaporation. The resultant surfaces produce the best light yield for LAr detectors. Sec. 3.1.1 and Appendix B of Ref. [12] carefully documented the equipment and technique of evaporation coating of wavelength shifter of the Princeton Nuclear and Particle Astrophysics Group. After the first SCENE data-taking campaign at Notre Dame (see Fig. G.1), the deployments of DarkSide-10 detector and the first deployment of DarkSide-50 detector [122], we observed damage to the TPB coating on the ITO electrodes due to the cool-down and warm-up cycle. These observations demonstrate that the adherence between TPB and a smooth ITO surface can only marginally withstand the thermal expansion and contraction experienced during detector commission or decomission.

The tight schedule in the detector development and data taking for the SCENE experiment required that the SCENE LAr detector must maintain a good light yield without replacing the TPB coating on ITO after several LAr fills. For achieving this goal, with the assistance of William McClain from the Chemistry Department of Princeton University,

Figure G.1: Photos of TPB coating on ITO electrodes without phenylphosphonic acid treatment before and after two LAr fills.

I modified the ITO electrode surfaces with phenylphosphonic acid. The molecule of this modifier has a polar functional group on one end and a non-polar functional group on the opposite end, so a mono layer of this modifier deposited on the ITO surface can change the wetting properties toward non-polar molecular solids [123]. We therefore expected an improvement in the robustness of the non-polar TPB coating. I tested a batch of ITO-coated quartz test samples with this procedure. After the TPB evaporation, the test samples were

repeatedly immersed in liquid nitrogen. The TPB coating showed little visual damage after those cycles.

The success of the test convinced our collaboration to experiment with the modification of the ITO electrodes of the SCENE detector. Before TPB coating, the ITO-coated fused silica windows were treated with the following steps:

1. Clean the ITO surface with ultrasonic cleaner for 20 minutes in a 1% detergent in milliQ water bath.

2. Rinse the ITO surface with milliQ water; 20 minutes ultrasonic cleaning in isopropyl alcohol bath.

3. Attach phenylphosphonic acid to ITO surface by immersing the window in a dilute (0.5 micromoles/L) solution of phenylphosphonic acid in ethanol.

4. Rinse the ITO surface with ethanol to remove multilayer.

5. Bake the ITO-coated quartz window at 120 °C for 30 minutes to achieve completion of chemical bonding.

Ref. [123] described a more rigorous, but also more time consuming ITO surface modification procedure.

The SCENE LAr-TPC with the surface-modified ITO windows achieved good light yield even on the third and fourth LAr fills, showing no sign of significant degradation. The photos in Fig. G.2 showed the TPB coatings after the fourth LAr fill. No serious degradation was observed on the cathode TPB coating, but some damage was still observed on the anode TPB coating. A possible cause for the damage could be the flow of electrons through the TPB on the anode when the extraction field was on, but the mechanism is not clear. The phenylphosphonic acid treatment seems a promising technique to improve the TPB coating on ITO electrodes in cryogenic applications, but more controlled studies should be performed

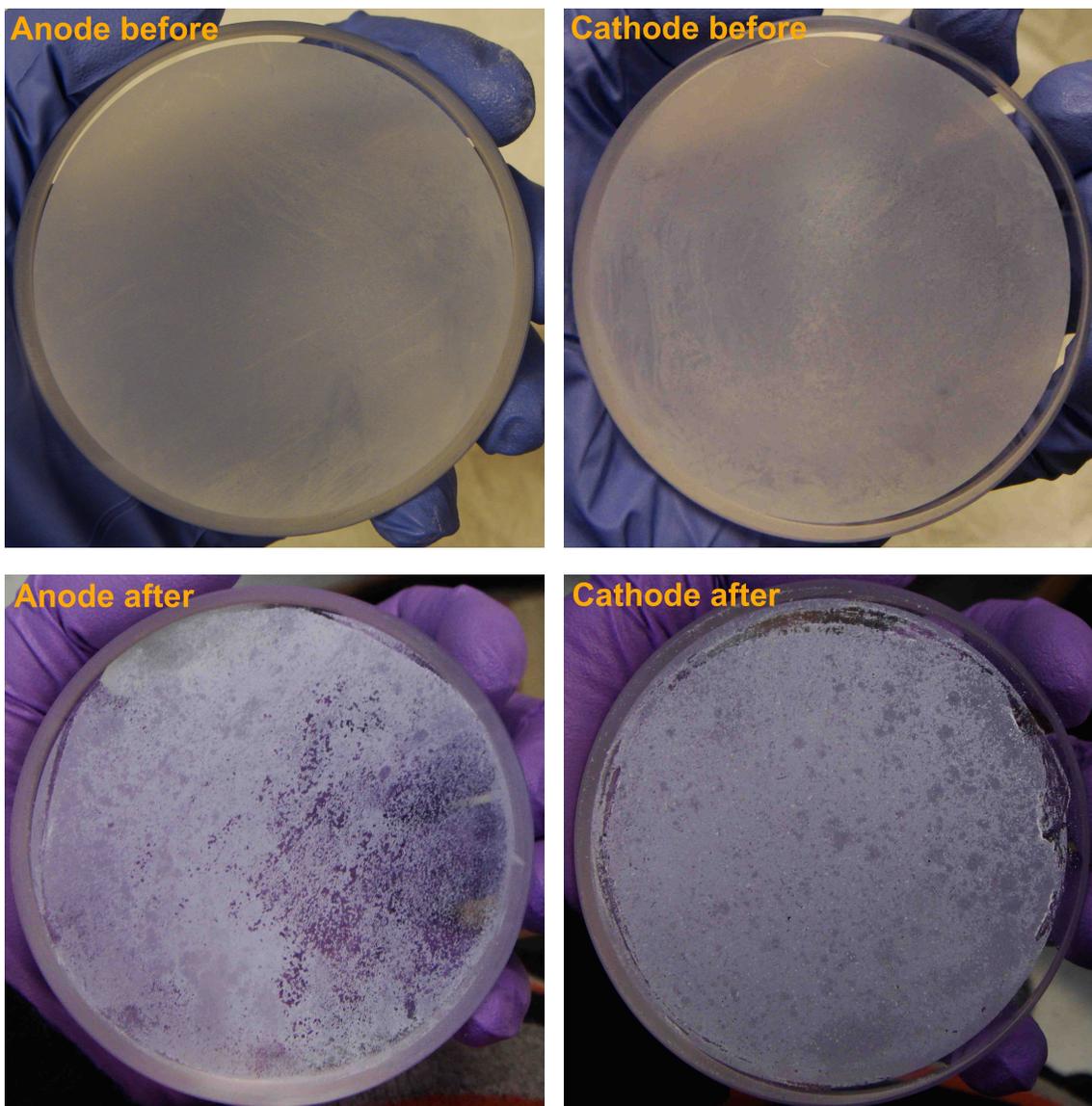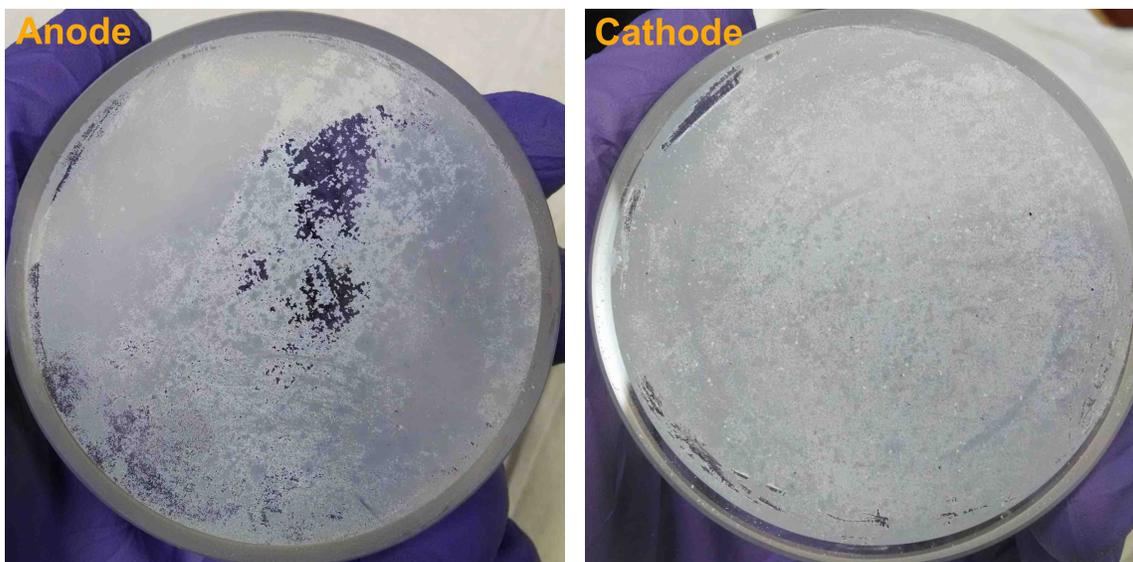Figure G.2: Photos of TPB coating on ITO electrodes with phenylphosphonic acid treatment after four LAr fills.

to improve the effectiveness of the technique. This technique may be applicable to other organic non-polar wavelength shifters.

Bibliography

[1] SCENE Collaboration, `http : / / lartpc – docdb . fnal . gov : 8080 / cgi – bin / ShowDocument?docid=692`, SCENE Project: Measurement of scintillation efficiency of nuclear recoils in noble elements.

[2] P. Ade et al., "Planck 2013 results. I. Overview of products and scientific results", (2013) `10.1051/0004-6361/201321529`.

[3] J. L. Feng, "Dark matter candidates from particle physics and methods of detection", Annual Review of Astronomy and Astrophysics **48**, 495–545 (2010).

[4] S. Arrenberg, H. Baer, V. Barger, L. Baudis, D. Bauer, et al., *Working Group Report: Dark Matter Complementarity*, (2013) `http://arxiv.org/abs/1310.8621`.

[5] G. Bertone, *Particle dark matter: observations, models and searches* (Cambridge Univ. Press, Cambridge, 2010).

[6] `http://hipacc.ucsc.edu/Bolshoi/index.html`, The Bolshoi Cosmological Simulations.

[7] L. Bergström, "Dark matter evidence, particle physics candidates and detection methods", Annalen der Physik **524**, 479–496 (2012).

[8] G. Bertone, "The moment of truth for wimp dark matter", Nature **468**, 389–393 (2010).

[9] C. E. Dahl, "The physics of background discrimination in liquid xenon, and first results from Xenon10 in the hunt for WIMP dark matter", ProQuest Dissertations and Theses No. 3364532, PhD thesis (Princeton University, 2009).

[10] W. H. Lippincott, "Direct detection of dark matter with liquid argon and neon", ProQuest Dissertations and Theses No. 3481704, PhD thesis (Yale University, 2010).

[11] B. M. Loer, "Towards a depleted argon time projection chamber WIMP search: Darkside prototype analysis and predicted sensitivity", ProQuest Dissertations and Theses No. 3440572, PhD thesis (Princeton University, 2011).

[12] J. Xu, "Study of Argon from underground sources for dark matter detection", ProQuest Dissertations and Theses No. 3597585, PhD thesis (Princeton University, 2013).

[13] P. Cushman, C. Galbiati, D. McKinsey, H. Robertson, T. Tait, et al., *Working Group Report: WIMP Dark Matter Direct Detection*, (2013) `http://arxiv.org/abs/1310.8327`.

[14] J. Buckley, D. Cowen, S. Profumo, A. Archer, M. Cahill-Rowley, et al., *Working Group Report: WIMP Dark Matter Indirect Detection*, (2013) `http://arxiv.org/abs/1310.7040`.

[15] L. Baudis, "Direct dark matter detection: the next decade", Physics of the Dark Universe **1**, Next Decade in Dark Matter and Dark Energy Next Decade in Dark Matter and Dark Energy, 94 –108 (2012).

[16] A. Schneider, L. Krauss, and B. Moore, "Impact of dark matter microhalos on signatures for direct and indirect detection", Phys. Rev. D **82**, 063525 (2010).

[17] A. K. Drukier, K. Freese, and D. N. Spergel, "Detecting cold dark-matter candidates", Phys. Rev. D **33**, 3495–3508 (1986).

[18] S. Ahlen, N. Afshordi, J. B. R. Battat, J. Billard, et al., "The case for a directional dark matter detector and the status of current experimental efforts", International Journal of Modern Physics A **25**, 1–51 (2010).

[19] P. Smith and J. Lewin, "Dark matter detection", Physics Reports **187**, 203 –280 (1990).

[20] B. Morgan, A. M. Green, and N. J. C. Spooner, "Directional statistics for realistic weakly interacting massive particle direct detection experiments", Phys. Rev. D **71**, 103507 (2005).

[21] L. Baudis, "{wimp} dark matter direct-detection searches in noble gases", Physics of the Dark Universe **4**, 50 –59 (2014).

[22] J. Lewin and P. Smith, "Review of mathematics, numerical factors, and corrections for dark matter experiments based on elastic nuclear recoil", Astroparticle Physics **6**, 87 –112 (1996).

[23] C. Savage, G. Gelmini, P. Gondolo, and K. Freese, "Compatibility of dama/libra dark matter detection with other searches", Journal of Cosmology and Astroparticle Physics **2009**, 010 (2009).

[24] A. Askew, S. Chauhan, B. Penning, W. Shepherd, and M. Tripathi, "Searching for Dark Matter at Hadron Colliders", Int.J.Mod.Phys. **A29**, 1430041 (2014).

[25] E. Aprile and T. Doke, "Liquid xenon detectors for particle physics and astrophysics", Rev. Mod. Phys. **82**, 2053–2097 (2010).

[26] P. Benetti, F. Calaprice, E. Calligarich, M. Cambiaghi, et al., "Measurement of the specific activity of 39ar in natural argon", Nuclear Instruments and Methods in Physics Research Section A: Accelerators, Spectrometers, Detectors and Associated Equipment **574**, 83 –88 (2007).

[27] J. Xu, F. Calaprice, C. Galbiati, A. Goretti, et al., *A Study of the Residual 39Ar Content in Argon from Underground Sources*, (Apr. 2012) `http://arxiv.org/abs/1204.6024`.

[28] H. O. Back, F. Calaprice, C. Condon, E. de Haas, et al., *First Large Scale Production of Low Radioactivity Argon From Underground Sources*, (Apr. 2012) `http://arxiv.org/abs/1204.6024`.

[29] T. Alexander, H. O. Back, H. Cao, A. G. Cocco, et al., "Observation of the dependence on drift field of scintillation from nuclear recoils in liquid argon", Phys. Rev. D **88**, 092006 (2013).

[30] H. Cao et al., *Measurement of Scintillation and Ionization Yield and Scintillation Pulse Shape from Nuclear Recoils in Liquid Argon*, (2014) http://arxiv.org/abs/1406.4825.

[31] D. Gastler, E. Kearns, A. Hime, L. C. Stonehill, S. Seibert, J. Klein, W. H. Lippincott, D. N. McKinsey, and J. A. Nikkel, "Measurement of scintillation efficiency for nuclear recoils in liquid argon", Phys. Rev. C **85**, 065811 (2012).

[32] C Regenfus, Y Allkofer, C Amsler, W Creus, A Ferella, J Rochet, and M Walter, "Study of nuclear recoils in liquid argon with monoenergetic neutrons", Journal of Physics: Conference Series **375**, 012019 (2012).

[33] E. Aprile, L. Baudis, B. Choi, K. L. Giboni, et al., "New measurement of the relative scintillation efficiency of xenon nuclear recoils below 10 keV", Phys. Rev. C **79**, 045807 (2009).

[34] G. Plante, E. Aprile, R. Budnik, B. Choi, K.-L. Giboni, L. W. Goetzke, R. F. Lang, K. E. Lim, and A. J. Melgarejo Fernandez, "New measurement of the scintillation efficiency of low-energy nuclear recoils in liquid xenon", Phys. Rev. C **84**, 045805 (2011).

[35] A. Manzur, A. Curioni, L. Kastens, D. N. McKinsey, K. Ni, and T. Wongjirad, "Scintillation efficiency and ionization yield of liquid xenon for monoenergetic nuclear recoils down to 4 kev", Phys. Rev. C **81**, 025808 (2010).

[36] L Baudis, J Hellmig, H. Klapdor-Kleingrothaus, Y Ramachers, J. Hammer, and A Mayer, "High-purity germanium detector ionization pulse shapes of nuclear recoils, -interactions and microphonism", Nuclear Instruments and Methods in Physics Research Section A: Accelerators, Spectrometers, Detectors and Associated Equipment **418**, 348 –354 (1998).

[37] E. Simon, L. Berg, A. Broniatowski, R. Bouvier, et al., "Sicane: a detector array for the measurement of nuclear recoil quenching factors using a monoenergetic neutron beam", Nuclear Instruments and Methods in Physics Research Section A: Accelerators, Spectrometers, Detectors and Associated Equipment **507**, 643 –656 (2003).

[38] P. Zecher, D. Wang, J. Rapaport, C. J. Martoff, and B. A. Young, "Energy deposition of energetic silicon atoms within a silicon lattice", Phys. Rev. A **41**, 4058–4061 (1990).

[39] G. Gerbier, E. Lesquoy, J. Rich, M. Spiro, et al., "Measurement of the ionization of slow silicon nuclei in silicon for the calibration of a silicon dark-matter detector", Phys. Rev. D **42**, 3211–3214 (1990).

[40] B. L. Dougherty, "Measurements of ionization produced in silicon crystals by low-energy silicon atoms", Phys. Rev. A **45**, 2104–2107 (1992).

[41] A. T. Lee, B. Cabrera, B. L. Dougherty, M. J. Penn, J. G. Pronko, and S. Tamura, "Measurements of the ballistic-phonon component resulting from nuclear and electron recoils in crystalline silicon", Phys. Rev. B **54**, 3244–3256 (1996).

[42] N. Spooner, G. Davies, J. Davies, G. Pyle, T. Bucknell, G. Squier, J. Lewin, and P. Smith, "The scintillation efficiency of sodium and iodine recoils in a NaI(Tl) detector for dark matter searches", Physics Letters B **321**, 156 –160 (1994).

[43] D. Tovey, V. Kudryavtsev, M. Lehner, J. McMillan, C. Peak, J. Roberts, N. Spooner, and J. Lewin, "Measurement of scintillation efficiencies and pulse-shapes for nuclear recoils in NaI(Tl) and CaF2(Eu) at low energies for dark matter experiments", Physics Letters B **433**, 150 –155 (1998).

[44] G. Gerbier, J. Mallet, L. Mosca, C. Tao, et al., "Pulse shape discrimination and dark matter search with NaI(Tl) scintillator", Astroparticle Physics **11**, 287 –302 (1999).

[45] T. Jagemann, F. Feilitzsch, and J. Jochum, "Measurement of the scintillation light quenching at room temperature of sodium recoils in NaI(Tl) and hydrogen recoils in NE 213 by the scattering of neutrons", Nuclear Instruments and Methods in Physics Research Section A: Accelerators, Spectrometers, Detectors and Associated Equipment **564**, 549 –558 (2006).

[46] H Chagani, P Majewski, E. J. Daw, V. A. Kudryavtsev, and N. J. C. Spooner, "Measurement of the quenching factor of Na recoils in NaI(Tl)", Journal of Instrumentation **3**, P06003 (2008).

[47] J. I. Collar, "Quenching and channeling of nuclear recoils in NaI(Tl): Implications for dark-matter searches", Phys. Rev. C **88**, 035806 (2013).

[48] C. Bacci, P. Belli, R. Bernabei, C. Dai, et al., "Dark matter search with calcium fluoride crystals", Astroparticle Physics **2**, 117 –125 (1994).

[49] H. Sekiya, M. Minowa, Y. Shimizu, Y. Inoue, and W. Suganuma, "Measurements of anisotropic scintillation efficiency for carbon recoils in a stilbene crystal for dark matter detection", Physics Letters B **571**, 132 –138 (2003).

[50] S. Yoshida, T. Ebihara, T. Yano, A. Kozlov, et al., "Light output response of kamland liquid scintillator for protons and 12c nuclei", Nuclear Instruments and Methods in Physics Research Section A: Accelerators, Spectrometers, Detectors and Associated Equipment **622**, 574 –582 (2010).

[51] C. A. Burke, M. T. Lunnon, and H. W. Lefevre, "^{7}Li$(p, n_0)^7$Be angular distribution to $E_p = 3.8$ MeV", Phys. Rev. C **10**, 1299–1308 (1974).

[52] T. H. Joshi, S. Sangiorgio, A. Bernstein, M. Foxe, et al., "First measurement of the ionization yield of nuclear recoils in liquid argon", Phys. Rev. Lett. **112**, 171303 (2014).

[53] S. Agostinelli, J. Allison, K. Amako, J. Apostolakis, et al., "Geant4 – a simulation toolkit", Nuclear Instruments and Methods in Physics Research Section A: Accelerators, Spectrometers, Detectors and Associated Equipment **506**, 250 –303 (2003).

[54] `http://mcnp.lanl.gov/`, General Monte Carlo N-Particle (MCNP) Transport Code, Los Alamos National Laboratory.

[55] J. I. Collar, "Applications of an ^{88}Y/Be Photoneutron Calibration Source to Dark Matter and Neutrino Experiments", Phys. Rev. Lett. **110**, 211101 (2013).

[56] E. Aprile, M. Alfonsi, K. Arisaka, F. Arneodo, et al., "Response of the XENON100 dark matter detector to nuclear recoils", Phys. Rev. D **88**, 012006 (2013).

[57] J Verbus, `http://lux.brown.edu/talks/20140228_jverbus_ucla2014.pdf`, "Calibration of the LUX Dark Matter Detector" (UCLA Dark Matter 2014).

[58] C. Chasman, K. W. Jones, H. W. Kraner, and W. Brandt, "Band-Gap Effects in the Stopping of Ge^{72*} Atoms in Germanium", Phys. Rev. Lett. **21**, 1430–1433 (1968).

[59] Y. Messous, B. Chambon, V. Chazal, M. D. Jsus, et al., "Calibration of a ge crystal with nuclear recoils for the development of a dark matter detector", Astroparticle Physics **3**, 361 –366 (1995).

[60] K. W. Jones and H. W. Kraner, "Energy lost to ionization by 254-eV ^{73}Ge atoms stopping in Ge", Phys. Rev. A **11**, 1347–1353 (1975).

[61] E. Behnke, T. Benjamin, S. J. Brice, D. Broemmelsiek, et al., "Direct measurement of the bubble-nucleation energy threshold in a CF_3I bubble chamber", Phys. Rev. D **88**, 021101 (2013).

[62] E. Aprile, C. E. Dahl, L. de Viveiros, R. J. Gaitskell, et al., "Simultaneous measurement of ionization and scintillation from nuclear recoils in liquid xenon for a dark matter experiment", Phys. Rev. Lett. **97**, 081302 (2006).

[63] T. Doke, A. Hitachi, J. Kikuchi, K. Masuda, H. Okada, and E. Shibamura, "Absolute scintillation yields in liquid argon and xenon for various particles", Japanese Journal of Applied Physics **41**, 1538 (2002).

[64] E. Aprile, K. L. Giboni, P. Majewski, K. Ni, M. Yamashita, R. Hasty, A. Manzur, and D. N. McKinsey, "Scintillation response of liquid xenon to low energy nuclear recoils", Phys. Rev. D **72**, 072006 (2005).

[65] P. Benetti, R. Acciarri, F. Adamo, B. Baibussinov, et al., "First results from a dark matter search with liquid argon at 87 K in the Gran Sasso underground laboratory", Astroparticle Physics **28**, 495 –507 (2008).

[66] The ArDM Collaboration, C. Amsler, A. Badertscher, V. Boccone, et al., "First results on light readout from the 1-ton ArDM liquid argon detector for dark matter searches", Journal of Instrumentation **5**, P11003 (2010).

[67] T. Alexander, D. Alton, K. Arisaka, H. Back, et al., "Light yield in DarkSide-10: A prototype two-phase argon TPC for dark matter searches", Astroparticle Physics **49**, 44 –51 (2013).

[68] E. Aprile, M. Alfonsi, K. Arisaka, F. Arneodo, et al., "Dark matter results from 225 live days of xenon100 data", Phys. Rev. Lett. **109**, 181301 (2012).

[69] D. Akerib, X. Bai, S. Bedikian, E. Bernard, et al., "The Large Underground Xenon (LUX) experiment", Nuclear Instruments and Methods in Physics Research Section A: Accelerators, Spectrometers, Detectors and Associated Equipment **704**, 111 –126 (2013).

[70] H. Gong, K. L. Giboni, X. Ji, A. Tan, and L. Zhao, "The cryogenic system for the Panda-X dark matter search experiment", Journal of Instrumentation **8**, P01002 (2013).

[71] Model FN from High Voltage Engineering Corporation.

[72] J Xu, `http://www.pa.ucla.edu/sites/default/files/webform/jingke_xu.pdf`, "SABRE - A new NaI dark matter experiment" (UCLA Dark Matter 2014).

[73] `http://www.eljentechnology.com/index.php/products/liquid-scintillators/71-ej-301`, EJ301 liquid scintillator from Eljen Technology, Inc.

[74] `http://www.3m.com`, Vikuiti enhanced specular reflector by 3M, Inc.

[75] `http://www.hamamatsu.com`.

[76] `http://www.cryomech.com/products/cryorefrigerators/pulse-tube/pt60/`.

[77] `http://www.airgassgcatalog.com/catalog/`, Ar BIP300 from Airgas, Inc.

[78] `http://www.saespuregas.com/Products/Gas-Purifier/PS4-MT315.html`, Mono-Torr PS4-MT3-R1 getter from SAES Pure Gas, Inc.

[79] `http://www.caen.it`, V1720B digitizers by CAEN S.p.A.

[80] `http://github.com/bloer/daqman`, daqman software.

[81] `http://www.lakeshore.com/products/cryogenic-temperature-controllers/model-336/`, Model 336 Cryogenic Temperature Controller from Lake Shore Cryotronics, Inc.

[82] `http://www.mksinst.com/`, 750B Pressure Transducer from MKS Instruments, Inc.

[83] `http://www.smartec-sensors.com/en/products/uti-interface-en.html`, Universal Transducer Interface from Smartec BV.

[84] `http://www.mccdaq.com/usb-data-acquisition/USB-1208LS.aspx`, USB-1208LS Multifunction USB Data Acquisition Device from Measurement Computing Corporation.

[85] `http://www.ni.com/labview/`, LabView software from National Instruments Corporation.

[86] `http://www.oceanoptics.com/`, LED-FC-355 from Ocean Optics, Inc.

[87] `http://www.hamamatsu.com/resources/pdf/etd/p-dev_2014_TOTH0022E01.pdf`, Hamamatsu R11065 PMT cathode current linearity.

[88] L. W. Kastens, S. B. Cahn, A. Manzur, and D. N. McKinsey, "Calibration of a liquid xenon detector with ^{83}Kr^m", Phys. Rev. C **80**, 045809 (2009).

[89] W. H. Lippincott, S. B. Cahn, D. Gastler, L. W. Kastens, E. Kearns, D. N. McKinsey, and J. A. Nikkel, "Calibration of liquid argon and neon detectors with ^{83}Kr^m", Phys. Rev. C **81**, 045803 (2010).

[90] A. Manalaysay, T. M. Undagoitia, A. Askin, L. Baudis, et al., "Spatially uniform calibration of a liquid xenon detector at low energies using ^{83m}Kr", Review of Scientific Instruments **81**, 073303, – (2010).

[91] `http://www.nndc.bnl.gov/ensdf`, National Nuclear Data Center, ENSDF.

[92] A. Hitachi, T. Takahashi, N. Funayama, K. Masuda, J. Kikuchi, and T. Doke, "Effect of ionization density on the time dependence of luminescence from liquid argon and xenon", Phys. Rev. B **27**, 5279–5285 (1983).

[93] G. Bakale, U. Sowada, and W. F. Schmidt, "Effect of an electric field on electron attachment to sulfur hexafluoride, nitrous oxide, and molecular oxygen in liquid argon and xenon", The Journal of Physical Chemistry **80**, 2556–2559 (1976).

[94] P. Cennini, S. Cittolin, J.-P. Revol, C. Rubbia, et al., "Performance of a three-ton liquid argon time projection chamber", Nuclear Instruments and Methods in Physics Research Section A: Accelerators, Spectrometers, Detectors and Associated Equipment **345**, 230 –243 (1994).

[95] S. Kubota, A. Nakamoto, T. Takahashi, T. Hamada, E. Shibamura, M. Miyajima, K. Masuda, and T. Doke, "Recombination luminescence in liquid argon and in liquid xenon", Phys. Rev. B **17**, 2762–2765 (1978).

[96] T. Doke, H. J. Crawford, C. R. Gruhn, A. Hitachi, J. Kikuchi, K. Masuda, S. Nagamiya, E. Shibamura, and S. Tamada, "Scintillation yields by relativistic heavy ions and the relation between ionization and scintillation in liquid argon", Nuclear Instruments and Methods in Physics Research Section A: Accelerators, Spectrometers, Detectors and Associated Equipment **235**, 136 –141 (1985).

[97] A. Hitachi, A. Yunoki, T. Doke, and T. Takahashi, "Scintillation and ionization yield for α particles and fission fragments in liquid argon", Phys. Rev. A **35**, 3956–3958 (1987).

[98] W. H. Lippincott, K. J. Coakley, D. Gastler, A. Hime, E. Kearns, D. N. McKinsey, J. A. Nikkel, and L. C. Stonehill, "Scintillation time dependence and pulse shape discrimination in liquid argon", Phys. Rev. C **78**, 035801 (2008).

[99] R. Acciarri, M. Antonello, B. Baibussinov, M. Baldo-Ceolin, et al., "Oxygen contamination in liquid argon: combined effects on ionization electron charge and scintillation light", Journal of Instrumentation **5**, P05003 (2010).

[100] R. Acciarri, M. Antonello, B. Baibussinov, M. Baldo-Ceolin, et al., "Effects of nitrogen contamination in liquid argon", Journal of Instrumentation **5**, P06003 (2010).

[101] B. J. P. Jones, T. Alexander, H. O. Back, G. Collin, J. M. Conrad, A. Greene, T. Katori, S. Pordes, and M. Toups, "The effects of dissolved methane upon liquid argon scintillation light", Journal of Instrumentation **8**, P12015 (2013).

[102] M. G. Boulay, B. Cai, M. Chen, V. V. Golovko, et al., *Measurement of the scintillation time spectra and pulse-shape discrimination of low-energy beta and nuclear recoils in liquid argon with DEAP-1*, (Apr. 2009) `http://arxiv.org/abs/0904.2930`.

[103] `http://darkside-docdb.fnal.gov:8080/cgi-bin/ShowDocument?docid=937`, Analysis of 51-day campaign, October 2013 - June 2014.

[104] V. Gehman, S. Seibert, K. Rielage, A. Hime, Y. Sun, D.-M. Mei, J. Maassen, and D. Moore, "Fluorescence efficiency and visible re-emission spectrum of tetraphenyl butadiene films at extreme ultraviolet wavelengths", Nuclear Instruments and Methods in Physics Research Section A: Accelerators, Spectrometers, Detectors and Associated Equipment **654**, 116 –121 (2011).

[105] E. Aprile, M. Alfonsi, K. Arisaka, F. Arneodo, et al., "Observation and applications of single-electron charge signals in the XENON100 experiment", Journal of Physics G: Nuclear and Particle Physics **41**, 035201 (2014).

[106] E. Aprile, K. L. Giboni, P. Majewski, K. Ni, and M. Yamashita, "Observation of anticorrelation between scintillation and ionization for MeV gamma rays in liquid xenon", Phys. Rev. B **76**, 014115 (2007).

[107] M. Miyajima, T. Takahashi, S. Konno, T. Hamada, S. Kubota, H. Shibamura, and T. Doke, "Average energy expended per ion pair in liquid argon", Phys. Rev. A **9**, 1438–1443 (1974).

[108] J. Thomas and D. A. Imel, "Recombination of electron-ion pairs in liquid argon and liquid xenon", Phys. Rev. A **36**, 614–616 (1987).

[109] D.-M. Mei, Z.-B. Yin, L. Stonehill, and A. Hime, "A model of nuclear recoil scintillation efficiency in noble liquids", Astroparticle Physics **30**, 12 –17 (2008).

[110] J. A. LaVerne, A. Hitachi, J. J. Kolata, and T. Doke, "Scintillation and ionization in allene-doped liquid argon irradiated with ^{18}O and ^{36}Ar ions of 30 MeV/u", Phys. Rev. B **54**, 15724–15729 (1996).

[111] D. N. Spergel, "Motion of the earth and the detection of weakly interacting massive particles", Phys. Rev. D **37**, 1353–1355 (1988).

[112] Jaffé, George, "Sur l'ionisation des diélectriques liquides par l'émanation du radium", Radium (Paris) **10**, 126–134 (1913).

[113] G. Jaffé, "Zur Theorie der Ionisation in Kolonnen", Annalen der Physik **347**, 303–344 (1913).

[114] G. Jaffé, "Zur Theorie der Ionisation in Kolonnen. II", Annalen der Physik **393**, 977–1008 (1929).

[115] C. Galbiati and F. Calaprice, "Measuring WIMP wind directionality in the WARP two-phase argon drift chamber", WARP Internal Report, Princeton University, 2005.

[116] D. R. Nygren, "Columnar recombination: a tool for nuclear recoil directional sensitivity in a xenon-based direct detection WIMP search", Journal of Physics: Conference Series **460**, 012006 (2013).

[117] D. W. Swan, "Ionization of liquid argon by α particles", Proceedings of the Physical Society **85**, 1297 (1965).

[118] R. Acciarri, C. Adams, J. Asaadi, B. Baller, et al., "A study of electron recombination using highly ionizing particles in the ArgoNeuT Liquid Argon TPC", Journal of Instrumentation **8**, P08005 (2013).

[119] J. F. Ziegler, `http://www.srim.org`.

[120] A. Hitachi, T. Doke, and A. Mozumder, "Luminescence quenching in liquid argon under charged-particle impact: relative scintillation yield at different linear energy transfers", Phys. Rev. B **46**, 11463–11470 (1992).

[121] `https://lapth.cnrs.fr/micromegas/`, MicrOMEGAs: a code for the calculation of Dark Matter properties including the relic density, direct and indirect rates in a general supersymmetric model and other models of new physics.

[122] P Meyers, `http://darkside-docdb.fnal.gov:8080/cgi-bin/ShowDocument?docid=767`, "DarkSide-50 TPC: design, implementation, commissioning, and performance " (DarkSide General Meeting, Feb 2014).

[123] S. A. Paniagua, P. J. Hotchkiss, S. C. Jones, S. R. Marder, A. Mudalige, F. S. Marrikar, J. E. Pemberton, and N. R. Armstrong, "Phosphonic acid modification of indiumtin oxide electrodes: combined xps/ups/contact angle studies", The Journal of Physical Chemistry C **112**, 7809–7817 (2008).